A Study of AGB Stars in the Sagittarius Dwarf Spheroidal

A thesis submitted to The University of Manchester for the degree of
Master of Science by Research
in the Faculty of Engineering and Physical Sciences

2012

Jennifer White

School of Physics and Astronomy

Contents

List of Figures

List of Tables

The University of Manchester

ABSTRACT OF THESIS submitted by Jennifer White
for the Degree of Master of Science by Research and entitled
A Study of AGB Stars in the Sagittarius Dwarf Spheroidal. 2012.

A study of 1095 objects located towards the Sagittarius dwarf spheroidal (Sgr dSph) has been undertaken. 19 of these stars were classified as C-type stars, 341 were classified as M-type stars and 733 were classified as K-type stars (one of the objects was found to be the galaxy 2MASX J18521545-2948214). These stars belong to two radial velocity populations; the Galactic stars with an average radial velocity peak of −13 km s^{-1} and a dispersion of 53 km s^{-1}, and the Sgr dSph stars with an average radial velocity peak of 141 km s^{-1} and a dispersion of 15 km s^{-1}. The determined radial velocities are accurate to ± 10 km s^{-1}. Stars with $(J-K)$ values placing them on the observed giant branch are likely to belong to the Sgr dSph.

Five observed stars are suggested to belong to the metal-poor population of the Sgr dSph, and from these observations it is determined that the metal-poor population of the Sgr dSph is $\frac{1}{11}$ the size of the bulk population.

The onset of thermal pulses is found to coincide with the luminosity of the RGB tip. Four carbon stars are located at this luminosity and it is suggested that, rather than stars in the Sgr dSph becoming carbon-rich very early on the TP-AGB, these stars in fact are in the helium burning phase of the thermal pulse cycle.

An average carbon-rich lifetime of between 1.07 and 2.26×10^5 years is determined and it is calculated that carbon stars in the Sgr dSph may only undergo one or two thermal pulses before high mass-loss rates terminate their AGB lifetimes. Total mass-loss rates of 10^{-5} $M_{\odot}$ yr^{-1} are found for the most reddened carbon stars.

An approximate C/M ratio for the Sgr dSph is determined to be 0.54, indicating that carbon stars are produced by the bulk population.

Declaration

I declare that no portion of the work referred to in the thesis has been submitted in support of an application for another degree or qualification of this or any other university or other institute of learning.

Copyright Statement

Acknowledgements

I would like to thank my supervisor, Albert Zijlstra, for all his help and support throughout this year. I would also like to thank Iain McDonald for his invaluable guidance.

I am greatly endebted to the various Phd students who have helped me on my way; in particular Liz Gurman and Czarek Szyszka for their help with data reduction, Mark Purver for never getting annoyed by my multitude of questions regarding LaTeX, and Jen Gupta and Libby Jones for welcoming me and making the office a fun place to be.

This thesis was typeset with LaTeX.

The Author

The author graduated from the University of Southampton in 2010 with a BSc in Physics. Since then she has been studying for an MSc by Research in Astronomy and Astrophysics at the Jodrell Bank Centre for Astrophysics. The results of this research are presented in this thesis.

List of Abbreviations and Symbols

The following abbreviations and symbols are used throughout this thesis:

1D – One Dimensional

2MASS – Two Micron All Sky Survey

AGB – Asymptotic Giant Branch

CCD – Charge-Coupled Device

CEMP – Carbon-Enhanced Metal-Poor object

CMD – Colour–Magnitude Diagram

CSE – Circumstellar Envelope

ESO – European Southern Observatory

FDU – First Dredge Up

FWHM – Full Width at Half Maximum

H–R diagram – Hertzsprung–Russell diagram

HB – Horizontal Branch

HBB – Hot Bottom Burning

IR – Infrared

IRAS – Infrared Astronomical Satellite

ISCZ – Inter-Shell Convective Zone

ISM – Interstellar Medium

$L_\odot$ – Solar Luminosity

LMC – Large Magellanic Cloud

LPV – Long Period Variable

LSP – Long Secondary Period

$M_\odot$ – Solar Mass

MC – Magellanic Cloud

MS – Main Sequence

MW – Milky Way

PN(e) – Planetary Nebula(e)

RGB – Red Giant Branch

rms – root mean square

SAAO – South African Astronomical Observatory

SAGE – Surveying the Agents of a Galaxy's Evolution

SED – Spectral Energy Distribution

Sgr dSph – Sagittarius dwarf Spheroidal

SHB – Synthetic Horizontal Branch

SMC – Small Magellanic Cloud

SRV – Semi-Regular Variable

TP-AGB – Thermally Pulsating Asymptotic Giant Branch

UT2 – The second VLT Unit Telescope

UV – Ultraviolet

VLT – Very Large Telescope

WISE – Wide-field Infrared Survey Explorer

1

Introduction

1.1 Stellar Evolution of AGB Stars

1.1.1 From the Main Sequence to the Asymptotic Giant Branch

A star spends the majority of its life on the main sequence (MS), burning hydrogen into helium in its core via the proton-proton chain (in stars of mass $\lesssim 1\mathrm{M}_\odot$) or the CNO cycle (in stars of higher mass). Once the core has been exhausted of hydrogen it contracts under gravity and rises in temperature, and the hydrogen burning moves outwards to a shell surrounding the helium core. If the star is massive enough ($M > 4-5\ \mathrm{M}_\odot$; Pilachowski 1988), after the exhaustion of core hydrogen it will be subjected to the first dredge-up (FDU). The FDU mixes the products of hydrogen burning with the outer stellar layers and alters the chemical abundances of the surface layer. Stars having undergone the FDU will subsequently exhibit an increase in ^{14}N, a decrease in ^{12}C and lower ^{12}C/^{13}C and ^{12}C/^{14}N ratios (Gratton et al. 2004; Gilroy 1989).

The contraction of the core leads to an increase in temperature, which causes the outer layers of the star to expand and its luminosity to grow, and it begins to ascend the red giant branch (RGB). Hydrogen-shell burning produces further helium, which collects on the helium core. The core continues to contract and increase in temperature, and it eventually reaches temperatures high enough for helium burning to occur ($\sim 10^8$

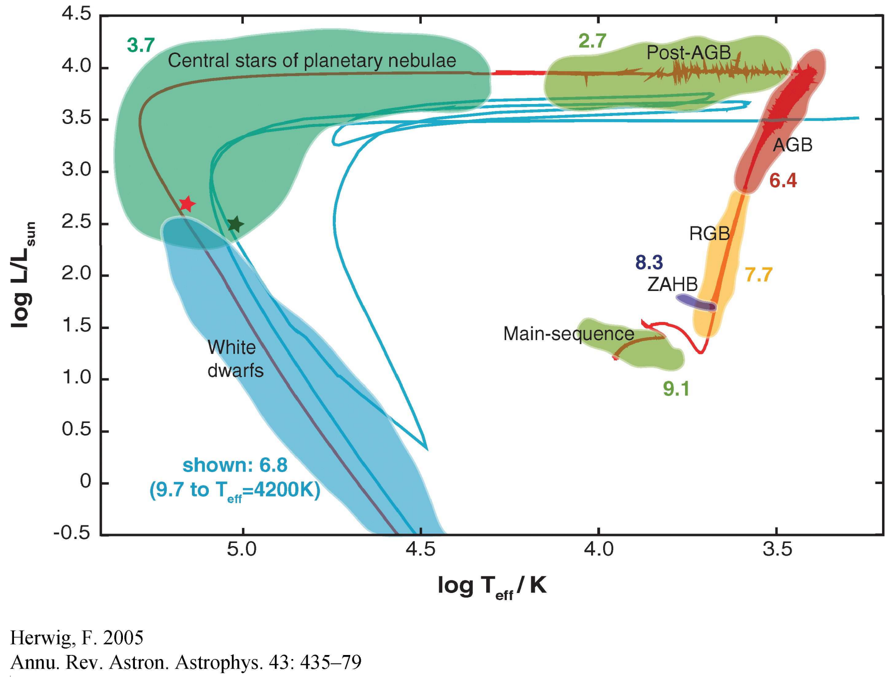

Figure 1.1: Hertzsprung–Russell diagram for a star of 2 $M_\odot$ at solar metallicity, taken from Herwig (2005). The complete evolutionary track is shown, from the main sequence to the white dwarf phase. The blue track shows the evolution of a 'born-again' star (see §1.1.7) of the same mass. The main evolutionary phases are labelled, along with the log of the time spent in these phases by a 2 $M_\odot$ star.

K).

In low mass stars ($M < 2 - 3$ $M_\odot$), helium burning begins after a violent helium flash which alleviates the degeneracy of the core. Higher-mass stars activate helium burning in their cores without such an aggressive start (Willson 2000). While the star is burning helium in its core, and undergoing hydrogen-shell burning, it lies on the horizontal branch (HB) (Lattanzio and Wood 2004).

After the consumption of all the helium in the core, helium burning too moves outwards to a helium-burning shell around the degenerate carbon and oxygen core. In stars of high enough mass ($M \gtrsim 4$ $M_\odot$; Blöcker 1999) the second dredge-up will occur after the termination of core helium burning, mixing these newly processed elements to the surface. The star is now evolving up the asymptotic giant branch (AGB).

AGB stars are characterised by an outer shell of hydrogen burning and an inner

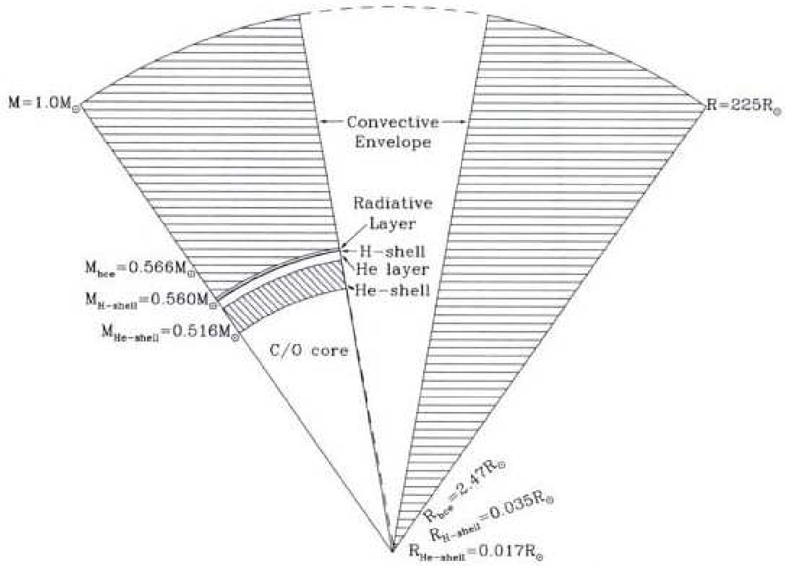

Figure 1.2: The internal structure of a 1 $M_\odot$ AGB star, taken from Lattanzio and Wood (2004). On the left, various regions are plotted against mass, while on the right they are plotted against radius.

shell burning helium, both of which surround a dense, degenerate carbon and oxygen core. The degeneracy of the core prevents any carbon burning from taking place within the core, due to neutrino emisssion (Lattanzio and Wood 2004). Figure 1.1 shows the evolution of a 2 $M_\odot$ star, at solar luminosity, from the main sequence to the AGB and beyond on the Hertzsprung–Russell (H–R) diagram.

1.1.2 The Early-AGB to the TP-AGB

The star then ascends the AGB, burning helium and hydrogen in shells surrounding a degenerate carbon and oxygen core. Figure 1.2 shows the internal structure of a 1 $M_\odot$ AGB star. Core contraction and nuclear burning within the shells have caused the outer layers of the star to swell enormously, up to hundreds of solar radii (Lamers and Cassinelli 1999). The AGB is divided into two sections; the early-AGB and the thermally pulsating-AGB (TP-AGB).

On the early-AGB nearly all the luminosity and energy of the star is provided by the helium-burning shell. The energy released by the helium-burning shell causes the layers above it to expand and therefore cool. This expansion pushes the hydrogen-burning shell out to lower temperatures, which almost forces the termination of hydrogen burning. While the star continues to evolve up the AGB, its helium shell becomes thinner as it burns through the helium deposited by the earlier hydrogen-shell burning. The helium-burning shell moves outwards, approaching the hydrogen shell, and begins to run out of fuel; as it does so its luminosity drops off to $\frac{1}{6} - \frac{1}{10}$ of its former value (Becker and Iben 1980). The hydrogen shell is reignited as the layers below it have continued to contract and therefore heat up. The hydrogen-burning shell now becomes the dominant luminosity source.

At the end of the early-AGB phase the star has two active burning shells, their close proximity and the high temperature dependence of helium burning cause a strong thermal instability which leads to thermal pulses.

1.1.3 A Thermal Pulse

Throughout the greater part of a thermal pulse the hydrogen-burning shell provides most of a star's energy. Periodically, every $\sim 10^4 - 10^5$ years, the helium burning shell will ignite in a helium shell flash which lasts for a few hundred years. The helium shell burns very brightly, with the brightest even reaching luminosities of up to 10^8 $L_\odot$ (Iben 1984; Lattanzio and Forestini 1999). The energy is produced by this reaction far too quickly to be released on radiation timescales; therefore an inter-shell convective zone (ISCZ) is created around the helium-burning region. Helium burns via the triple-alpha process; ^{4}He is burnt into ^{12}C, which in turn can capture α- particles to produce ^{16}O. The ISCZ is made up of ~75% helium, ~22% carbon and a few percent oxygen.

During the 'power-down' phase of a thermal pulse the helium-burning shell begins to decline. This leads to the disappearance of the ISCZ. The energy released by helium burning causes the outer layers of the star to expand and the hydrogen shell is thus forced out to cooler temperatures and lower densities, where it is almost extinguished.

The next stage of a thermal pulse is the one that is the most consequential for the evolution of an AGB star; the third dredge up.

1.1.4 The Third Dredge-Up

The third dredge-up occurs during the TP-AGB. Energy produced during helium shell burning is absorbed by the convective envelope. This increase in luminosity escaping from the core causes the convective envelope to extend inwards. If the convective envelope penetrates the layers in which nucleosynthesis took place it causes the newly created helium- and hydrogen-shell burning products to be dredged up.

The main consequence of the third dredge-up is the enrichment of the stellar envelope in ^{12}C. With each consecutive thermal pulse, further carbon is dredged up to the stellar surface. AGB stars undergoing the third dredge-up will also show an over-abundance of ^{4}He and some *s*-process elements in their stellar envelopes. These *s*-process elements are produced by slow neutron capture, where an unstable nucleus decays via β-decay before capturing a neutron (Iben 1984). This occurs deep within the star when $T \sim 10^8$ K. The N/O ratio will also be affected in stars which have experienced the third dredge-up, as ^{14}N is converted into ^{22}Ne (Becker and Iben 1980). In AGB stars of $M \gtrsim 3$ M$_\odot$ (Lattanzio 2003) this ^{22}Ne can then go on to capture an α-particle, producing ^{25}Mg and a neutron. It is the neutrons created via this process, or via ^{13}C(α,n)^{16}O, which are responsible for the formation of the neutron-rich *s*-process elements (Blöcker 1999).

Thermal pulses therefore, continually enrich the stellar envelope with carbon and other elements. This crucially affects the C/O ratio which plays an important role in the rest of the star's evolution.

The C/O Ratio

AGB stars are split into two main types; oxygen-rich (M-type) and carbon-rich (C-type) stars, depending on the C/O ratio of the star. *J*, *H* and *K* band colour–magnitude diagrams show a distinct separation between the two types, with carbon stars being typically a lot redder than M-type stars at the same luminosity. This colour difference is due to the molecular absorption lines of CN in carbon-rich stars absorbing more blue light than the equivalent in oxygen-rich stars. Recent surveys in the near-and mid-infra-red (e.g. *2MASS*, *WISE* & *AKARI*), and spectral surveys undertaken using the *Spitzer Space Telescope* have helped to illustrate the divide between oxygen- and carbon-rich stars (Marigo 2008).

Carbon monoxide (CO) is one of the first molecules to be formed within the star; it has a high binding energy (11.1 eV) and is therefore a very stable molecule. This means that all atoms of the least abundant element, carbon or oxygen, are trapped within the CO molecules. If there is an excess of carbon, the C/O ratio will be greater than unity and hence the star is a carbon star. The opposite is true for an abundance of oxygen, the C/O ratio is less than unity and the star is an M-type, oxygen rich star. Whether a star is oxygen-rich or carbon-rich greatly affects its evolution, and the chemical composition of the dust produced by the star depends on it.

While all AGB stars begin as oxygen-rich stars, after a number of thermal pulses (and therefore dredge-ups) enough carbon can be mixed to the surface to trap all oxygen atoms within CO molecules, creating an S-type star with C/O $\approx$ 1[1]. Further dredge up of carbon tips the C/O ratio to above unity and the star becomes a carbon-rich C-star.

The C/O ratio affects the type of dust produced in the star. This dust is released into the interstellar medium (ISM) during the heavy mass loss experienced towards the end of the AGB. In carbon stars the dust will mostly be formed of amorphous carbon dust (“soot”) and other hydrogen rich elements, e.g. C_2H_2, CN and HCN. The spectra from M-type stars are dominated by oxygen-rich molecules such as SiO, TiO and H_2O, forming silicates and oxides (“sand”). However, shocks within the stellar envelope may lead to the formation of a small fraction of molecules of the opposite type (Decin et al. 2008).

[1] C/O $\approx$ 1 is a very transitory phase (Iben 1984), therefore S-type stars are rare.

1.1.5 Hot Bottom Burning

Hot bottom burning (HBB) occurs in the most massive AGB stars ($M \approx 4$ M$_\odot$)[2] when the base of the convective envelope reaches high enough temperatures, ($T > 40 \times 10^6$ K; Ventura and Marigo 2010), for nuclear processing. In lower-mass stars there is a radiative buffer between the H-burning shell and the convective envelope, in AGB stars of greater mass this isn't the case. The convective envelope and the H-burning shell overlap causing some of the products of hydrogen burning to be injected directly into the outer layers. This can have a significant effect on the chemical composition of a star, as the stellar envelope will be enriched with material that has repeatedly undergone proton-proton chain reactions.

The stars studied in this thesis are all very old and therefore, are not massive enough to ignite HBB. However, I will summarise the main consequences of HBB. HBB can delay or even prevent the formation of carbon stars as it causes ^{12}C to be burnt into ^{15}N via the CN cycle. As well as this reduction in ^{12}C and increase in ^{15}N, stars that have undergone HBB can be recognised by low C/O and ^{12}C/ ^{13}C ratios, plus enhancements of ^{7}Li and ^{23}Na, ^{25}Mg, ^{26}Mg and ^{26}Al from the Ne-Na and Mg-Al chains (Boothroyd et al. 1995; Lattanzio et al. 2004; Ventura and D'Antona 2011). As a star evolves up the AGB, its envelope mass is continually reduced due to the stellar wind and this gradual loss of the envelope mass terminates HBB in AGB stars. At this critical point the temperature will have dropped too low for nucleosynthesis to occur at the base of the convective envelope.

1.1.6 Variability

Stars on the AGB begin to undergo long period and large-amplitude pulsations. They are described as long period variables (LPVs) and semi-regular variables (SRVs). LPVs with large amplitudes ($\Delta V > 2.5$ mag; Whitelock et al. 2008) are known as Mira vari-

[2]This is for solar metallicity, but the minimum mass for the onset of HBB will decrease with lower metallicities, as lower metallicity stars burn at higher temperatures.

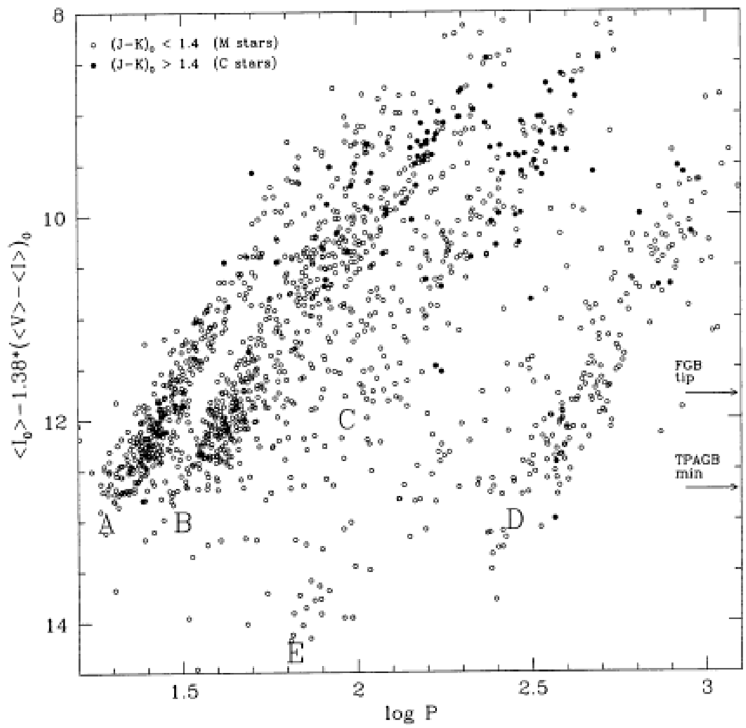

Figure 1.3: The period–luminosity diagram for variable stars in the Large Magellanic Cloud, taken from Wood et al. (1999). Explanations of the sequences are given in the text. Wood et al. (1999) chose $I_W =< I_0 > -1.38 \times (< V > - < I >)_0$ as the luminosity index for the y-axis as it is almost reddening free.

ables. Mira variables have regular periods of $\sim 80 - 1000$ days[3], while SRVs are lower in amplitude and have less regular periods of $\sim 30 - 150$ days (Lebzelter et al. 2005; Zijlstra 2006). AGB stars pulsate due to the κ-mechanism, first suggested by Eddington (1917); opacity (κ) variations in ionisation zones alternately block and transmit the emerging radiative flux, leading to pulsations. In Cepheid variables this occurs during the second helium ionisation (Zhevakin 1963; Baker and Kippenhahn 1965) but in these LPVs, pulsations are due to the ionisation of hydrogen.

Period–luminosity relationships for Miras were obtained through studies of the Large Magellanic Cloud (LMC) (e.g. Feast et al. 1989), but these early relations were

[3]N. N. Samus and O. V. Durlevich, 2009, *GCVS Variability Types* [online] http://www.sai.msu.su/gcvs/gcvs/iii/vartype.txt (accessed 31/01/2011)

calculated using only a few infrared observations (Feast 2004). Wood et al. (1999) also studied optically visible Miras and SRVs in the LMC and established five parallel period–luminosity sequences for these stars, as shown in Figure 1.3.

Miras and SRVs occupy only three of these five sequences; SRVs are found on A, B and the lower part of C, whereas Mira variables only occupy the C sequence. As a star evolves up the AGB it grows in luminosity and therefore, its period also increases (Lattanzio and Wood 2004). Sequence C represents the fundamental mode of the variable star; Mira variables pulsate in this mode after evolving through the overtone modes of the A and B sequences. Some AGB stars with longer periods, $P > 420$ days (Feast et al. 1989), do not follow these period–luminosity relations; these more massive stars are probably experiencing HBB and therefore are at higher luminosities than predicted (Whitelock 2003).

A number of LPVs have been found to display a secondary period of pulsation (Payne-Gaposchkin 1954). These long secondary periods (LSPs) exceed the stars' primary pulsation periods, having lengths of $\sim 250 - 1400$ days (Nicholls et al. 2009). LSPs occur on sequence D of Figure 1.3 (Wood et al. 1999) and while at least 30% of variable red giants exhibit LSPs (Soszynski et al. 2004), there is no current understanding of their cause.

LPVs are the most luminous stars in old or intermediate age stellar populations, therefore it is crucial to understand them in order to use them as tracers of the history of star formation in galaxies (Whitelock 2003). The period–luminosity relation can be used as a distance indicator for these galaxies.

Pulsations within AGB stars also significantly affect the mass-loss rates of these stars, as discussed in §1.2.2, with stars undergoing large-amplitude pulsations also experiencing high mass-loss rates (Lebzelter and Wood 2011).

1.1.7 Termination of the AGB Phase

During the TP-AGB significant mass loss occurs (see §1.2). During a star's TP-AGB evolution, its stellar luminosity increases, until a limiting value is reached. During this time, the star's thermal pulses become more frequent, until the final thermal pulse ejects the majority of the remaining atmosphere. AGB stars eventually lose approximately ∼35 − 85 % of their initial mass (Marshall et al. 2004), with this mass loss ending the AGB phase of a star's life. Once the stellar envelope has been reduced to $\lesssim 10^{-3}$ $M_{\odot}$ (Lattanzio and Wood 2004) the star begins its post-AGB evolution and starts to shrink. Due to the small envelope mass of the star, a radiative buffer zone is present between the base of the convective envelope and the hydrogen-burning shell. Therefore, the mass loss of the envelope does not directly affect the core luminosity of the star.

Mass-loss rates on the AGB reach $10^{-7} - 10^{-4}$ $M_{\odot}$ yr^{-1} with wind speeds of 5 – 25 km s^{-1}, while post-AGB wind speeds reach much higher values but with lower mass-loss rates. However, it has been found that stars at lower metallicity exhibit slower wind speeds than this (Marshall et al. 2004; Zijlstra 1999; Wood et al. 1992), due to the metallicity dependence on dust production which hence affects the dust-gas coupling, see §1.3. The slow AGB stellar wind is caught up by this faster wind creating a dense shell of compressed gas (Schönberner and Steffen 2003; Kwok et al. 1978; Cerrigone et al. 2006; Lamers and Cassinelli 1999). Meanwhile, the core of the star has continued to contract and is therefore increasing in temperature. A post-AGB star is defined as an object in which the superwind[4] has ceased but the central star has not yet reached the temperatures required to ionise the surrounding circumstellar matter. Once this critical temperature is reached ($T \gtrsim 20000$ K; Waelkens and Waters 2004; Suárez et al. 2006; Mesler and Henson 2008), radiation from the hot core ionises the two interacting winds forming a planetary nebula (PN). However, not all post-AGB stars become planetary nebulae (PNe); stars with lower initial masses evolve too slowly through the post-

[4]The superwind is the period of time in which the greatest mass-loss rates are reached, see §1.2.2

AGB phase. Therefore, when the central star reaches the temperatures hot enough for ionisation, the ejected circumstellar matter will have been lost to the ISM and no PN is visible (Karakas 2010).

The post-AGB phase is brief, only lasting around 10^4 – 10^5 years (Habing and Olofsson 2003; van Winckel 2011), and it covers a range of objects; from stars which have only just left the AGB, to those which are on the verge of becoming PNe. Observing post-AGB stars is difficult as their short lifetimes mean that they are rare objects. Furthermore, some individual post-AGB objects have been the subject of multiple studies and are hence very well known, while the stage as a whole is poorly understood (Waelkens and Waters 2004). A post-AGB star can be simplistically described as a visible central star surrounded by a shell of ejected circumstellar material. This arrangement produces a 'double peaked' spectral energy distribution (SED) (Mesler and Henson 2008; García-Lario 2006), with a bump in the visible due to the bright central star and a second in the mid- to far-infrared from the cold dust shell.

Stars which have begun their post-AGB evolution may experience a final thermal pulse. This causes the rapid inflation of their circumstellar envelopes (CSEs) back to red giant size. Stars which undergo this transformation are known as 'born again' AGB stars and evolve very rapidly (Waelkens and Waters 2004). It is thought that approximately 10% of post-AGB stars will undergo these late pulses (van Winckel 2003).

One significant observation that still isn't understood is the transition, during the post-AGB phase, from the generally spherically symmetric mass loss of TP-AGB stars, to the wide range of shapes and sizes found for PNe. Another discrepancy between AGB and post-AGB objects is found in their chemical signatures; only a few post-AGB stars exhibit evidence for the rich nucleosynthesis known to occur during the AGB (van Winckel 2011). It is therefore evident that further research must be done on this brief, yet dramatic, stage of stellar evolution.

After the PN phase and once all nuclear processes have ceased, all that is left of the star is the carbon and oxygen core supported by electron degeneracy pressure, which cools and fades as a white dwarf.

1.2 Mass Loss on the AGB

1.2.1 The Importance of Mass Loss

Mass loss on the AGB is a very important phenomenon; it drives the nourishment of the ISM and causes the termination of the AGB. In this section, the current understanding of AGB mass loss will be discussed and the formation of dust in the CSEs of AGB stars will also be touched upon.

AGB stars eventually lose up to 85% of their initial main sequence mass to the ISM, via the stellar wind (Marshall et al. 2004). Furthermore, approximately 90% of stars that have died in the Universe so far have been AGB stars: it is evident that AGB mass loss is a very important phenomenon. Due to the third dredge-up (and HBB in more massive AGB stars) the stellar wind releases metal-rich molecules and dust into the ISM, the nature of which will depend on the C/O ratio of the star. Dust will dwell in the ISM for $\sim 10^8$ years (Jones et al. 1996) before being involved in star formation. Therefore, the mass injection from AGB stars greatly affects the chemical compositions of newly forming stars and galaxies.

1.2.2 Pulsation- and Dust-Driven Winds

The huge radii reached by AGB stars' extended CSEs mean that as long as there is a driving mechanism present, it is easy for the outer layers of the star to escape the star's gravity. This mass loss is known as the stellar wind.

The driving mechanism for AGB mass loss is a two stage process. First, pulsations in the star create shocks which levitate the outer envelope, causing it to expand and cool. Once the extended atmosphere reaches a radius of $\sim 1 - 2.5$ stellar radii the temperature will drop below the dust condensation temperature ($T \sim 500$ K $-$ 1800 K, dependent on molecular species; Millar 2004), allowing molecules to condense into dust grains (Lamers and Cassinelli 1999), see section §1.2.3. Secondly, radiation pressure on these dust grains accelerates them to the escape velocity. The gas is carried along with the dust particles due to 'momentum coupling' (Gilman 1972); the collisional coupling between the gas and the dust. Collisions between the grains and the gas molecules produce a drag force on the dust grains; the gas is driven outwards due to the flow of dust grains through it. A pulsation-driven wind can support a mass-loss rate of 10^{-7} $M_\odot$ yr^{-1} but, for the highest observed mass-loss rates of $10^{-5} - 10^{-4}$ $M_\odot$ yr^{-1}, dust-driven winds are required (Bowen and Willson 1991).

The Superwind

The Reimers' mass–luminosity relation (Reimers 1975) is widely used in modelling of mass loss throughout the Hertzsprung–Russell diagram:

$$\dot{M} \propto \frac{LR}{M}. \tag{1.1}$$

It is based on the assumption of continual mass loss throughout a stars' life, and while it is frequently still used to determine approximate rates of mass loss, it fails for the dusty winds of pulsating giant stars. The Reimers' mass–luminosity relation does not predict high enough mass-loss rates to explain the observed mass loss on the AGB (Bowen and Willson 1991). Based on this mass–luminosity relation the mass left at the termination of the AGB should be greater than 0.6 $M_\odot$. However, observations of white dwarfs have found that most of them have masses less than predicted by Reimers' law (Moehler et al. 2004). Gradual mass loss from AGB stars throughout their lives is therefore not enough to explain the observed mass-loss rates. The majority of mass loss occurs towards the end of the AGB, in a mass ejection of dust known as the superwind (Bowen and Willson 1991).

Mass-loss rates increase with luminosity and at the very end of an AGB star's life it experiences the superwind. It is during the superwind that the greatest mass-loss rates of $\sim 10^{-4}$ $M_\odot$ yr^{-1} are reached. During this period dust formation is very effective and the star, therefore, becomes surrounded by an optically-thick dust shell. Stars with these high mass-loss rates, which have long periods and exhibit strong 1612 MHz maser lines in their spectra, are classified as OH/IR stars (García-Lario et al. 1999; Engels et al. 1999).

The stellar mass-loss rate far surpasses the rate of nuclear processing within the core. The star therefore, sheds its outer mantle and terminates its life on the AGB before the core mass has had time to grow substantially larger.

1.2.3 Dust Grains and the ISM

Understanding the dust input into the ISM from AGB stars is greatly important in extending our knowledge of the subsequent stellar formation. The *Spitzer* surveys of the Magellanic Clouds (MCs) and the subsequent project 'Surveying the Agents of a Galaxy's Evolution' (SAGE) have produced photometric data for the LMC in varying filters, therefore providing information tracing the evolution of galaxies driven by the life cycle of dust. However, the number of observations are still quite limited (Boyer et al. 2009).

Dust is created within AGB stars during the TP-AGB, once envelope material has been forced out to temperatures lower than the condensation temperature and thus condenses into solid dust particles. Whether dust production is reliant on seed nuclei (around which the molecules condense) is still uncertain: this would introduce an extra metallicity dependence of the dust formation.

As discussed above, the nature of the dust produced in AGB stars is dependent on the C/O ratio of the star. Carbon-rich stars produce amorphous carbon dust and carbohydrates such as acetylene (C_2H_2) and silicon carbide (SiC), while oxygen rich stars produce metal oxides and silicate dust (SiO).

1.3 Low Metallicity Populations

Studies of stellar populations in low metallicity galaxies have become increasingly popular in recent years. Understanding these metal-poor Population II stars is a crucial step towards understanding the processes involved in evolving from an early Universe of only H and He, to the metal-rich Universe seen today.

Low metallicity stars exhibit lower atmospheric opacities and therefore are warmer for a given luminosity (Scalo and Miller 1981; Mouhcine and Lançon 2002). This in turn also necessitates that they evolve to higher luminosities in order to initiate the superwind (Mouhcine and Lançon 2002), compared to higher metallicity stars of the same mass.

Low metallicity populations can be recognised by their ultraviolet (UV) excess. The UV flux of a star is affected by heavy metals in the star, however this is obviously reduced at low metallicities, leading to extra UV light being produced in comparison (Roman 1954; Siegel et al. 2009).

Dust-formation rates fall at lower metallicities causing a reduction in the dust-to-gas ratio, which in turn affects the velocities of stellar winds. Since the expansion velocity of the gas is dependent on the coupling between the dust and the gas, when less dust is produced, each grain will have to drag along more gas with it, causing lower wind speeds in lower metallicity galaxies such as the MCs and the Sagittarius dwarf spheroidal (Sgr dSph) (Wood et al. 1992; Zijlstra 1999; Marshall et al. 2004).

It is also found that LPVs at lower metallicity have shorter pulsation periods than expected in Galactic stars (Wood et al. 1998; Feast and Whitelock 2000). Higher metallicity stars have longer periods as their giant branches are redder and thus their radii greater (Wood et al. 1998).

1.3.1 Mass Loss at Low Metallicities

The *Spitzer* surveys of the Large and Small Magellanic Clouds (LMC and SMC, respectively) have provided observations which generated a lot of interest in low metallicity mass-loss rates; the MCs have metallicities of [Fe/H]= -0.52 to -0.30 (Westerlund 1997; Lagadec et al. 2008) and [Fe/H]= -0.90 to -0.60 (Russell and Dopita 1992; Venn 1999; Rolleston et al. 1999, 2003; Lee et al. 2005) for the LMC and SMC, respectively. SAGE-LMC (Meixner et al. 2006), SAGE-SMC (Gordon et al. 2011) and SAGE-Spec (Kemper et al. 2010) provided the first observations of AGB stars in the MCs over extensive luminosity and mass ranges. Since the distances to the MCs are known, absolute mass-loss rates of AGB stars at low metallicities can be obtained from the *Spitzer* observations.

Bowen and Willson (1991) predicted that at lower metallicities ([Fe/H] < -1) dust-driven winds would fail and mass-loss rates would depend on pulsation-driven winds only. Zijlstra (2004) followed up their work and found that based on Bowen & Willson's calculations, the final mass of a star's core becomes a lot greater in these metal-poor regimes and can even exceed the Chandrasekhar limit (1.4 $M_{\odot}$). Therefore, Bowen & Willson's theories predict the occurrence of AGB supernovae.

Lagadec et al. (2009a) investigated the mass loss from the Sgr dSph, to further study the mass-loss rates and dust production of its stars. They commented on the prevalence of carbon stars at low metallicity. This is due to the longer carbon-rich lifetimes of low metallicity stars (Mouhcine and Lançon 2002, 2003). Low-metallicity stars will become carbon-rich much faster than their Galactic counterparts as they are formed with a lower oxygen abundance and, therefore, fewer dredge-ups are required to reach a C/O ratio above unity. Naturally, these dredge-ups do not cease after the formation of a carbon star: the stellar envelope is continually being enriched with further carbon. Hence, lower-metallicity stars can be expected to reach higher C/O ratios than comparable AGB stars within our Galaxy. This was found to be the case (Matsuura et al. 2005; Lagadec et al. 2009a).

It has also been discovered that these low-metallicity carbon stars have mass-loss rates similar to Galactic carbon stars. However, oxygen-rich stars display lower mass-loss rates at lower metallicity (Sloan et al. 2008). At low metallicity carbon stars have higher mass-loss rates than oxygen-rich stars. This might be explained by the fact that the production of amorphous carbon (which makes up most of the dust formed in carbon stars) depends on self produced carbon, whereas oxygen-rich stars produce dust from metallicity limited elements, such as Si and Al (Zijlstra 2006; Lagadec and Zijlstra 2008). The production of dust in oxygen-rich stars at low metallicity is therefore heavily reduced[5]. The work by Boyer et al. (2011), with the SAGE-SMC data, supports this prediction. They compared their data with the findings of SAGE-LMC and discovered that the LMC displays greater silicate emission than the SMC, suggesting that oxygen-rich dust production is hampered at lower metallicities. On the other hand, carbon-rich dust formation rates were comparable between the two MCs, indicating a much weaker (if any) dependence on metallicity.

Work done by Mattsson et al. (2008) complements these observations. Mattsson et al. (2008) modelled C-stars in low-metallicity environments and they too found that the mass-loss rates of these metal-poor stars were comparable to, or even higher, than stars of solar composition.

These more recent studies of mass loss at low metallicity contradict the predictions of AGB supernovae suggested by Bowen and Willson (1991). In low-metallicity galaxies, dusty winds can be maintained and the rate of mass loss via these winds is still well above the rate of core growth from nuclear burning. This indicates that AGB stars will terminate their evolution via mass loss before the core has had time to grow significantly, therefore rejecting the expectation of the existence of AGB supernovae.

1.4 The Sagittarius Dwarf Spheroidal

The Sgr dSph was discovered by Ibata et al. (1994). It is the second nearest dwarf galaxy to the Milky Way (MW) at only ~25 kpc away (Giuffrida et al. 2010; Sbordone

[5] While the production of amorphous carbon doesn't depend on the galactic metallicity, the abundance of the seeds around which dust grains may be formed could still be metallicity dependent. However, the metallicity dependence of carbon-rich dust will still be less than the metallicity dependence of dust in oxygen-rich stars (Lagadec et al. 2008).

et al. 2007; Lagadec et al. 2008), after the exception of the newly discovered Canis Major dwarf galaxy (Martin et al. 2004). It covers a large area of the sky, with dimensions of approximately $15^\circ \times 7^\circ$ (Giuffrida et al. 2010). Despite its ample size, the Sgr dSph wasn't discovered until recently due to the fact that it is located behind the Galactic Bulge, this continues to make the dwarf galaxy difficult to observe as there is a lot of contamination from foreground stars. The Sgr dSph has a short orbital period around the MW of < 1 Gyr (Sbordone et al. 2007; Bellazzini et al. 1999b).

The Sgr dSph is being tidally destroyed by our Galaxy. The MW is accreting the dwarf galaxy by tidal stripping and will eventually integrate it completely. Studies of the Sgr dSph therefore, are tremendously useful, providing us with an insight into the physics involved in the tidal destruction of satellite galaxies.

Four globular clusters are associated with the Sgr dSph: Terzan 7, Terzan 8, Arp 2 and M54. M54 is located at the centre of the Sgr dSph although it is likely that it was formed elsewhere before being pulled to the centre (Giuffrida et al. 2010).

1.4.1 Metallicity and Chemical Composition of the Sagittarius Dwarf Spheroidal

The Sgr dSph contains different metallicity populations throughout the galaxy, therefore there is also a considerable range of stellar ages in the Sgr dSph. The main stellar population has a metallicity of $-0.7 \leq$ [Fe/H] ≤ -0.4 (Lagadec et al. 2008; Giuffrida et al. 2010) and an age of ~8 Gyr (Lagadec et al. 2009b). However, there is also a younger, more metal-rich population of [Fe/H]= -0.25 (Bonifacio et al. 2004), and a small, very metal-poor population with a metallicity of [Fe/H]= -2.0, which is thought to be much older (Bellazzini et al. 1999a).

Chou et al. (2007) also discovered a metallicity gradient within the stellar component of the tidal stream being accreted by the MW, with more metal-rich stars having been stripped from the Sgr dSph more recently. This finding complements the theory that the Galactic Halo is made up of stars that have been accreted from dwarf galaxies being tidally disrupted by the MW. So far no stellar population has been found within the MW with the same chemical abundances as the dwarf spehroidals, however Chou et al. (2007) provide evidence that there may be vast differences between current chemical compositions of dwarf spheroidals and the stars they have accreted in the past.

The Sgr dSph has a chemical composition very unlike the MW. Significant under-abundancies of α-elements and other light elements such as Na, Al, Sc, V, Co, Ni, Cu, Zn are recorded, in comparison to Galactic stars with the same iron content. Overabundances of La, Ce and Nd are also detected, as well as wildly different abundance ratios (Sbordone et al. 2007). From this striking chemical signature it is possible to detect globular clusters that originated in the Sgr dSph but have since moved away. This is the case with Palomer 12, whose Sgr dSph origin has been confirmed through the work of Sbordone et al. (2007)[6].

1.5 The Project

The dredge up and extensive mass loss a star undergoes during the TP-AGB phase of its life are crucial in the evolution of stars. The dredge up greatly alters the composition of the dust ejected from the CSEs of AGB stars, while the mass loss heralds the end of a star's active life. It is also vitally important in the birth of new stars and planets: the matter expelled from AGB stars makes up the majority of the ISM. Hence, the chemical composition of this matter will greatly affect the compositions of new stars born from the ISM. The study of AGB stars is crucial in understanding stellar and galactic evolution.

The high mass-loss rates towards the end of a star's AGB evolution also cause the termination of its nuclear fusion evolution along the AGB by evaporating the star's

[6] It is worth noting that the presence of this 'chemical signature' is unknown at metallicities lower than [Fe/H]=-1, therefore the stars stripped from the Sgr dSph earlier, and hence at lower metallicites, may not be detectable through this method (Sbordone et al. 2007).

atmosphere, see §1.2.

The Sgr dSph is a low metallicity ([Fe/H] ~ -2.0 to -0.25; Bellazzini et al. 1999b; Bonifacio et al. 2004) dwarf galaxy being tidally destroyed by the Milky Way. Its low metallicity makes the Sgr dSph a highly interesting object to study. If we can understand the metal poor stars of the Sgr dSph we can hope to understand the processes involved in evolving from a completely H-He Universe to the metal-rich Universe we see today.

This project is a study of the Sgr dSph, focusing on the upper-RGB and the AGB. The aim is to further our understanding of how the AGB evolves at lower metallicities, and we hope to better realise the carbon-rich stage of an AGB star's life.

In Chapter 2, our observations and the data reduction undertaken to extract spectra from them will be discussed. Chapter 3 will focus on determining the spectral types of our data; how many objects are oxygen- or carbon-rich, and then plotting a colour–magnitude diagram (CMD) of our observations. The radial velocities of the stars will be calculated in Chapter 4, to determine which of them are members of the Sgr dSph, rather than Galactic foreground stars. In Chapter 5, the Hertzsprung–Russell (H–R) diagram of our data will be plotted, after the bolometric luminosities of our observed stars have been determined. This H–R diagram will also be compared with theoretical isochrones and evolutionary tracks, to try and determine the carbon-rich lifetime of stars within the Sgr dSph. Chapter 6 will present a comparison of our observations with other published catalogues. Finally, a discussion of all the findings of this thesis will be presented in Chapter 7, and Chapter 8 will draw together the project's conclusions.

2

Observations and Data Reduction

The data for this project were taken using the 1.9 m Radcliffe telescope at the South African Astronomical Observatory (SAAO) along with data from the Very Large Telescope (VLT) at the European Southern Observatory (ESO). Before any of the goals of this project can be accomplished, the raw data must first be reduced to the useful spectra to work from.

The SAAO, situated in Sutherland was established in 1972 with the merging of the Royal Observatory at the Cape of Good Hope with the Republican Observatory in Johannesburg[1]. In 1974 the Radcliffe Observatory in Pretoria closed and its 1.9 m telescope was moved to the SAAO (Laney 1996).

The European Southern Observatory (ESO) is an inter-governmental organisation incorporating 15 member countries[2]. The VLT is located at Cerro Paranal in the north of Chile. It consists of four 8.2 m telescopes, observing in the optical, near- and mid-infrared[3].

In this Chapter, brief introductions to the telescopes and instruments will be given, the target observations will be summarised and the techniques used in reducing the

[1]SAAO, 2008, *History: SAAO* [online] http://www.saao.ac.za/about/history/ (accessed 29/07/2011)

[2]ESO, 2011, *ESO's Organisational Structure* [online] http://www.eso.org/public/about-eso/organisation.html (accessed 29/07/2011)

[3]ESO, 2011, *The Very Large Telescope* [online] http://www.eso.org/public/teles-instr/vlt.html (accessed 29/07/2011)

data will be outlined.

2.1 Observations

The observations from the VLT were taken on June 23rd 2010 and Sept 21st – 26th 2010, using the second VLT Unit Telescope (UT2). The fibre-fed, multi-object spectrograph FLAMES (Pasquini et al. 2002) was used with the GIRAFFE grating filters H14B, H16, L5 and L6. The two high resolution grating filters (H14B and H16) have wavelength ranges of 638.3 – 662.6 nm and 693.7 – 725.0 nm, at a resolving power of R = 28800 and 23900 respectively, while the low resolution filters (L5 and L6) cover 574.1 – 652.4 nm and 642.8 – 718.4 nm at a resolving power of R = 7400 and 8600 respectively. Nine fields were observed using all four of these grating settings, with exposure times of 300 seconds for the two low resolution filters, 780 seconds for H14B and 900 seconds for H16. The coordinates for the observed fields are listed in Table 2.1. The target list comprised a magnitude selected sample of $2MASS$ objects within 1° of the core of the Sgr dSph and with $K < 11$. Further objects with fainter K magnitudes were visually selected from the comparison of a Sgr dSph field with a Galactic field, to choose objects which are most likely to belong to the giant branch of the dwarf galaxy. This selection of observed stars can be seen in Figure 3.4. A total of 1015 stars were observed with the VLT.

Data taken at the VLT using UVES, a high-resolution optical spectrograph located on UT2, were also obtained. The same nine fields were observed on June 24th 2010, and Sept 20th – 27th 2010. The red echelle grating was used with the cross-disperser grating CD3. This provided a central wavelength of 580 nm, a wavelength range of 420 – 680 nm and a resolving power of R = 22500. However, due to time limitations this data set is yet to be analysed.

To complement the data taken using the VLT, observations made at the SAAO were also obtained. Observations from the 1.9 m Radcliffe telescope were taken between July 4th – July 8th 2009; 26 stars were observed. In addition to this the data for 65

Table 2.1: Postions of the observed Sag dSph Fields.

Field	Central Coordinates (J2000.0)	
Sag_dSph_Field_1	$18^h56^m24^s.0$	$-30°31'47''.7$
Sag_dSph_Field_2	$18^h53^m24^s.0$	$-30°20'58''.5$
Sag_dSph_Field_3	$18^h54^m00^s.1$	$-30°44'59''.1$
Sag_dSph_Field_4	$18^h58^m26^s.5$	$-31°22'46''.7$
Sag_dSph_Field_5	$18^h59^m38^s.6$	$-31°01'09''.8$
Sag_dSph_Field_6	$18^h58^m21^s.1$	$-30°42'00''.1$
Sag_dSph_Field_7	$18^h55^m11^s.9$	$-30°11'59''.9$
Sag_dSph_Field_8	$18^h48^m28^s.7$	$-30°12'01''.9$
Sag_dSph_Field_9	$18^h52^m12^s.0$	$-29°59'58''.2$

stars observed during the week of July 28th – Aug 3rd 2010 were obtained. The grating spectrograph with the SITe CCD was used, with grating #5. This is a 1200 lines mm^{-1} grating with a central wavelength at 6800 Å, a total wavelength coverage of the range 6400 – 7200 Å and a resolution of 1 Å (Kilkenny 2010).

The SAAO observations were chosen to focus on objects in the region of the Sgr dSph. A targetted survey of the AGB and upper-RGB stars in the galaxy was carried out. These images were observed for exposure time lengths of 1800 seconds, with the exception of four objects observed for 600 seconds and two objects observed for 1200 seconds.

As well as observations of these stars, bias, flat and arc lamp calibration frames were also recorded.

2.2 Reducing the SAAO Data

Using IRAF, the overscan area, bias and flat field are corrected for and bad columns and cosmic rays are removed. Wavelength calibration is then applied to the images and the background is subtracted. The image is then collapsed to a 1D spectrum and the spectra are smoothed, in order to help identify stellar types. For a detailed account, see Appendix B.

2.2.1 Overscan Region

Many CCD arrays produce an overscan region as a measure of the bias level on an exposed image. The overscan region is comprised of a few columns and rows around the image edge which are not exposed to light.

Within IRAF, the task `imhead` was used to extract the overscan region and `ccdproc` was used to remove it from the images.

2.2.2 Bias Subtraction

Once the overscan area has been corrected for the remaining bias must be removed from the images. Bias is a small electric voltage that is not a result of excitation, but is added to the signal by the computer to prevent any values falling below zero. To correct for the bias, bias frames must be taken in the dark with zero exposure time (or as close to zero as is possible) to ensure that any counts measured by the CCD are due to this signal and its associated noise ($\sqrt{n}$).

The task `zerocombine` is used to create an average bias image from all the bias frames. `ccdproc` is then used to remove this average bias frame from all the object images.

Unfortunately the bias frames obtained at the SAAO were taken with the CuNe arc lamp left on. Therefore, there are several bright lines present within the master bias. Dark lines of negative counts are a residual effect, within all the object images,

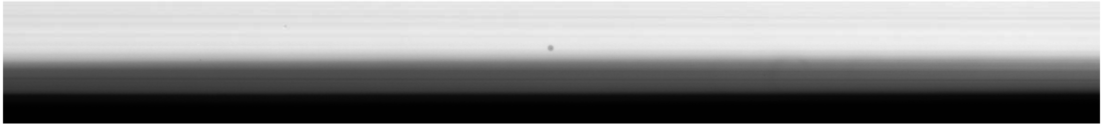

Figure 2.1: A section of an example flat field image taken at the SAAO.

of subtracting the master bias.

2.2.3 Dark Current

CCD images are also affected by dark current. Dark current is the signal created by electron excitation due to thermal emission rather than due to light. To correct for dark current, dark frames are taken at the same temperature and exposure time as the object images, but in the dark so as to measure this thermal excitation.

The SITe1 CCD used with the grating spectrograph on the 1.9 m telescope at the SAAO is cooled, using liquid nitrogen, to ~180 K (Kilkenny 2010). At such a low temperature the effects due to dark current are negligable.

2.2.4 Flat Field

Flat fields are used to correct for any sensitivity variations from pixel to pixel and also any optical transmission irregularities, due to dust, defective pixels and vignetting, present in the image. Flat field images are exposures of a uniform background, allowing any features due to the irregularities mentioned to be removed. The object images are divided by the flat field to reduce the effects of these imperfections.

Unfortunately, the flat fields taken at SAAO appeared to show a graduated light leak, as shown in Figure 2.1, and therefore, they were not used. Attempts to acquire better images were unsuccessful however, visual inspection of the flat field images suggests that flatfielding would have only a small effect ($\lesssim$ few %) on the final spectra. The procedure to apply the flat field correction is outlined in Appendix A.

2.2.5 Bad Pixels

As mentioned above, CCD images can have a variety of defects. Defective pixels include: hot pixels, which have a high dark current and therefore saturate very quickly; dead pixels, which do not register any counts and irregular pixels, which do not show a linear response to light. The bad pixels, or columns, are recorded in a list and then removed using the IRAF task `ccdproc`.

The lines of negative count, due to the bias subtraction, are corrected for by interpolating between their neighbouring pixels during the bad pixel removal.

2.2.6 Trimming the Images

The images are trimmed to remove the overscan regions, as described above, and any irregular pixel counts on the edges of the frame. Again `ccdproc` is used to complete the task.

2.2.7 Cosmic Ray Removal

Cosmic ray detections cause very high pixel counts and therefore need to be removed so that they do not contaminate the data. The task `lacos_spec`[4] is used. `lacos_spec` detects cosmic rays by the sharpness of their edges using Laplacian edge detection, and the values of these pixels are then compared to the expected noise value. Detected cosmic rays are replaced by the median value of their neighbouring pixels (van Dokkum 2001). The result of this can be seen in Figure 2.2.

2.2.8 Wavelength Calibration

Arc lamp images are used to calibrate the wavelength scale for our images. At the SAAO, a CuNe arc lamp was used to get the comparison spectra. The arclamp images

[4] The task `lacos_spec` is available from http://www.astro.yale.edu/dokkum/lacosmic/lacos_spec.cl

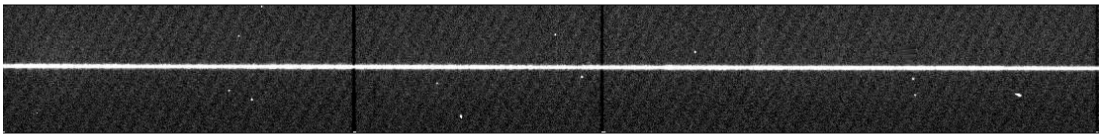

(a) An example section of an image before cosmic ray removal.

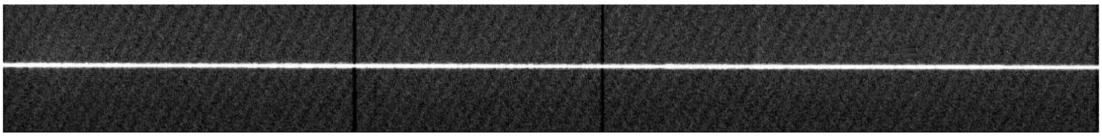

(b) An example section of an image after cosmic ray removal.

Figure 2.2: Displaying the effects of cosmic ray removal: the top image shows an example spectrum prior to cosmic ray removal, while the bottom image shows the same spectrum after cosmic rays have been removed.

have been reduced in the same way as the object images up until this point, with the exception of the cosmic ray removal.

Multiple steps are involved in wavelength calibration. First, the known spectral lines of the arc lamp images are identified using the IRAF task `identify` followed by `reidentify`. Next, the wavelengths of the lines are used to create the wavelength coordinates for the whole image; using the task `fitcoords`. This is followed by `transform`, which uses a bicubic polynomial interpolation to convert pixel number to wavelength for all images. `transform` is run twice; first to apply the calibration to the arc lamp image, and second to apply it to the object image. These steps are repeated for each arc lamp image and related object image.

2.2.9 Background Subtraction

The final IRAF programme used in reducing the SAAO data is the task `background`. This takes an average sky background flux and subtracts it from the object images. `background` must be run individually on each object image, with the co-ordinates of the spectrum and any bright pixels, which may have escaped previous calibration steps, specified.

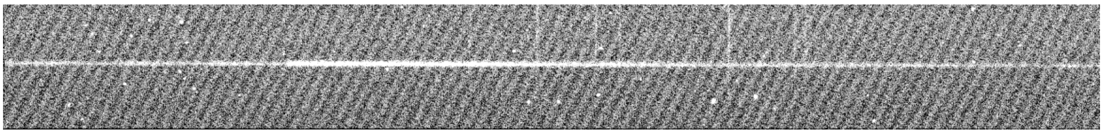

(a) An example section of a raw image.

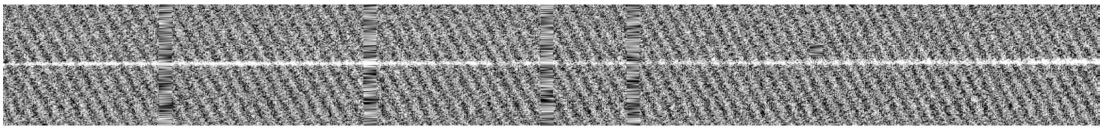

(b) An example section of an image after all calibration corrections have been completed.

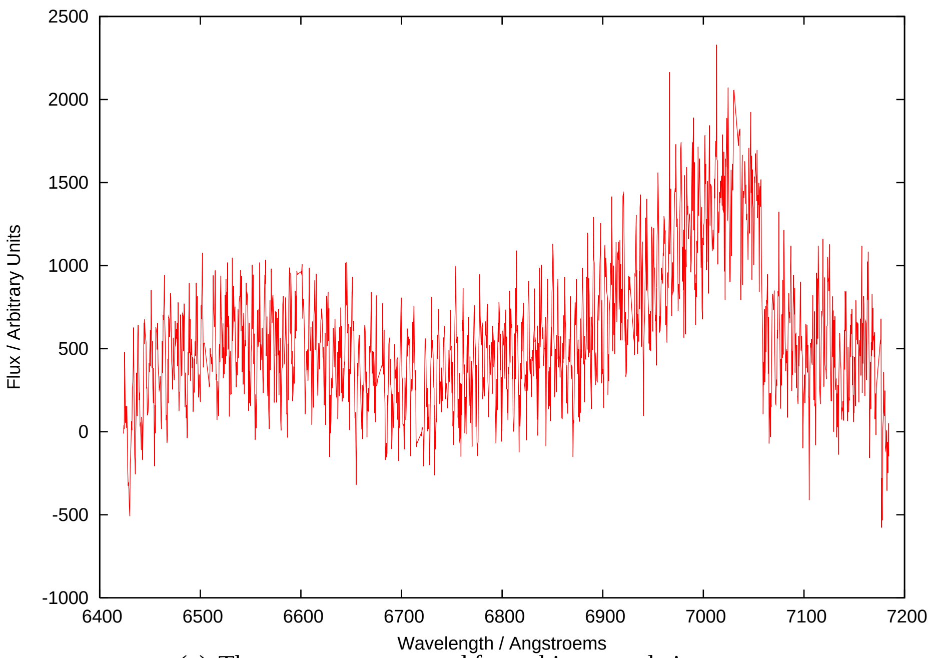

(c) The spectrum extracted from this example image.

Figure 2.3: Displaying the effects of the data reduction: the top figure shows the raw image, the middle figure shows the image after all calibration corrections and the bottom figure shows the spectrum extracted from this image.

2.2.10 Collapsing to 1D Line Spectra

Once the images have been calibrated using the IRAF packages as described above, they are collapsed to 1D spectra. This was done using a script, written by Iain McDonald. The script collapses the wavelength axis to find the detector row with the most flux, and sets the spectrum to be the sum of five rows either side of this peak pixel. The spectrum is then extracted and saved as a data file. For images with multiple stellar detections the spectrum selection has to be done manually.

Figure 2.3 presents the effects of the data reduction steps. The vertical lines in Figure 2.3(b) are due to the bad pixel removal of the dark lines caused by the bias subtraction. Figure 2.3(b) appears to have been flipped, with respect to Figure 2.3(a), as Figure 2.3(b) is in wavelength coordinates instead of pixel number.

2.3 Reducing the ESO Data

The ESO data contain multiple stellar observations per image. To reduce these data it was found that the automatic advanced GIRAFFE data reduction products provided with the raw frames[5] produced accurate enough results. Bias frames, arc lamp spectra and fibre flat fields are taken daily by the GIRAFFE calibration system. The arc lamp used is a Th-Ar lamp.

The bias frame is subtracted from the raw images, while the locus and width of each fibre is determined from the continuum calibration lamp information. The arc lamp frames are also used to do the wavelength calibration for each fibre. All the counts in the aperture are summed to extract the spectra and, finally, the images are flat field corrected to account for the differences in transmission between the fibres. The GIRAFFE automatic data reduction does not remove cosmic rays from the VLT data.

Neither the SAAO data nor the VLT data were flux calibrated, as no spectral flux standards were observed. However, this does not affect the presented results as there

[5]The GIRAFFE reduction pipeline is available at http://www.eso.org/projects/dfs/dfs-shared/web/vlt/vlt-instrument-pipelines.html

are very few telluric features present within the wavelength range of interest. Those that are present have very well known wavelengths and therefore can be identified visually.

The images were not corrected to the solar system barycentre.

3

Broad Spectral Typing

In this Chapter the spectral types of the observed stars are determined; whether they are M-stars, C-stars or S-stars. The stellar spectra are identified by the molecular features they exhibit. The J and K $2MASS$ magnitudes for each object are then used to plot a colour–magnitude diagram (CMD) of our data, in order to determine the number of carbon stars we have observed and also, where these carbon-rich stars lie on the CMD.

3.1 Carbon- or Oxygen- Rich?

Once the spectra have been reduced via the processes outlined in §2.2 and §2.3, the next stage is to identify whether the stars are oxygen- or carbon- rich.

3.1.1 Determining the SAAO Stellar Types

The SAAO spectra were visually compared to template carbon- and oxygen-rich stellar spectra, as shown in Figure 3.1[1], to determine their spectral types.

Oxygen-rich stars are identified by the TiO absorption features at 6650 Å and 7054 Å, whereas carbon-rich stars are identified due to absorption features around 6900 Å and 7060 Å, due to CN (Cote et al. 1997). S-type stars are identified by the presence

[1]The template spectra used can be found at http://www.sdss.org/dr5/algorithms/spectemplates/index.html

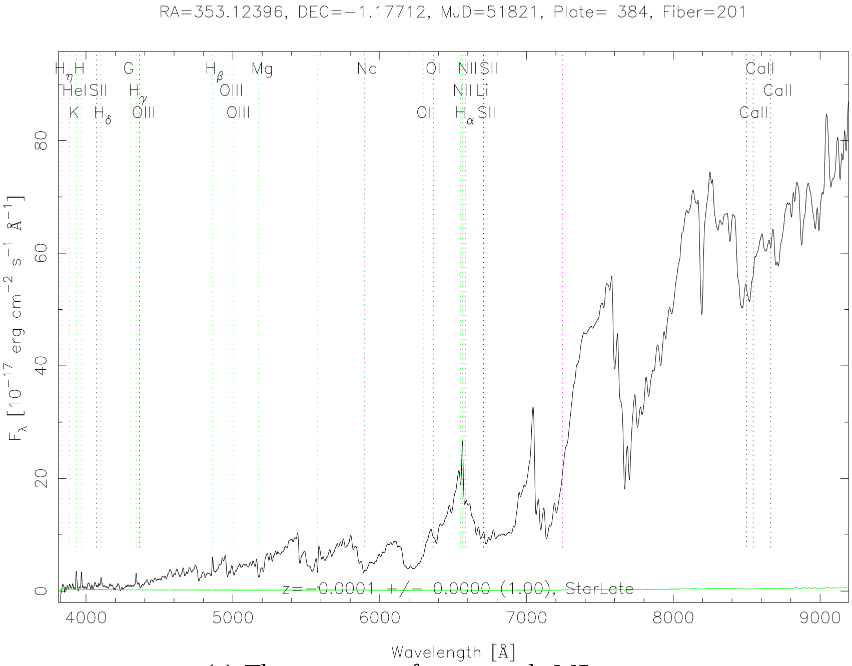

(a) The spectrum of an example M5 star.

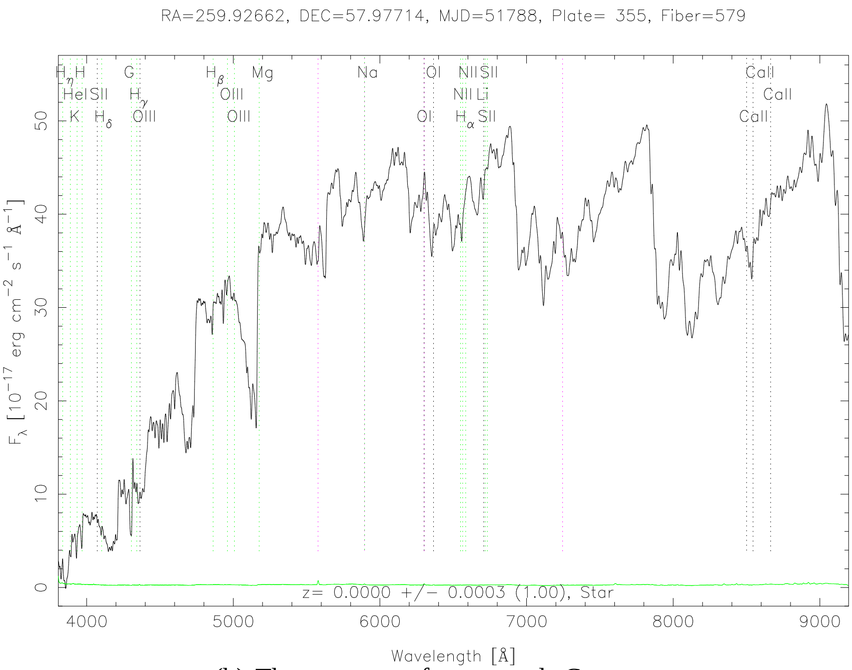

(b) The spectrum of an example C star.

Figure 3.1: The spectra against which the SAAO data were visually compared.

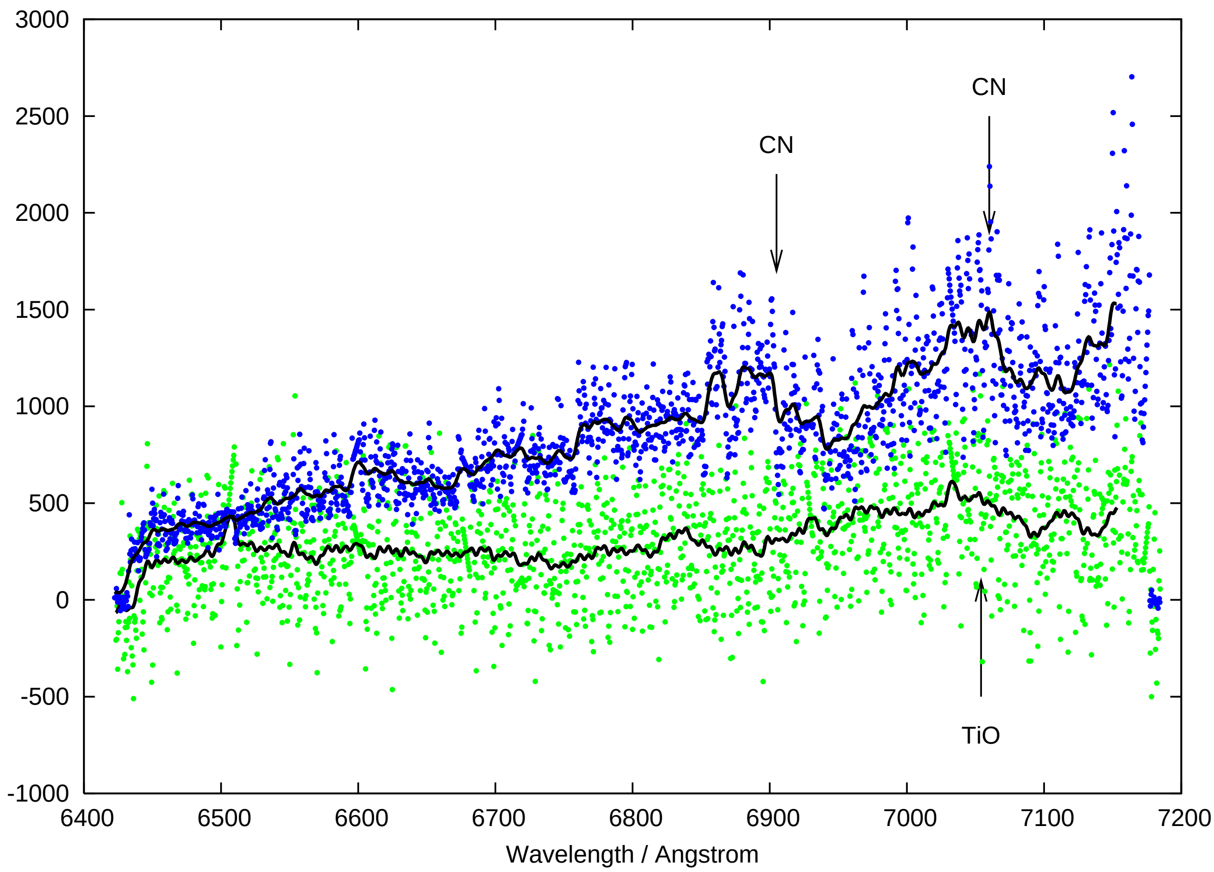

Figure 3.2: Example SAAO carbon-rich (blue dots) and oxygen-rich (green dots) stellar spectra, with the molecular features used to identify the spectral types indicated.

of ZrO molecular bands at 6473.7 Å, 6508.0 Å and 6542.8 Å (Ake 1979). However, in our observations no S-type stars were detected. As the S-type period is a brief evolutionary phase between M-type and C-type stars, S-type stars are less abundant than M- or C-type stars (Iben 1984; Ramstedt et al. 2011).

Figure 3.2 shows the spectra of a carbon-rich star and an oxygen-rich star. The oxygen-rich spectrum shows the effect of smoothing the spectra, making it easier to determine this star's oxygen-richness by highlighting the TiO features.

3.1.2 Determining the VLT Stellar Types

For each object, smoothed and unsmoothed versions of both low-resolution spectra were plotted against carbon- and oxygen-rich model spectra, to aid with the spectral

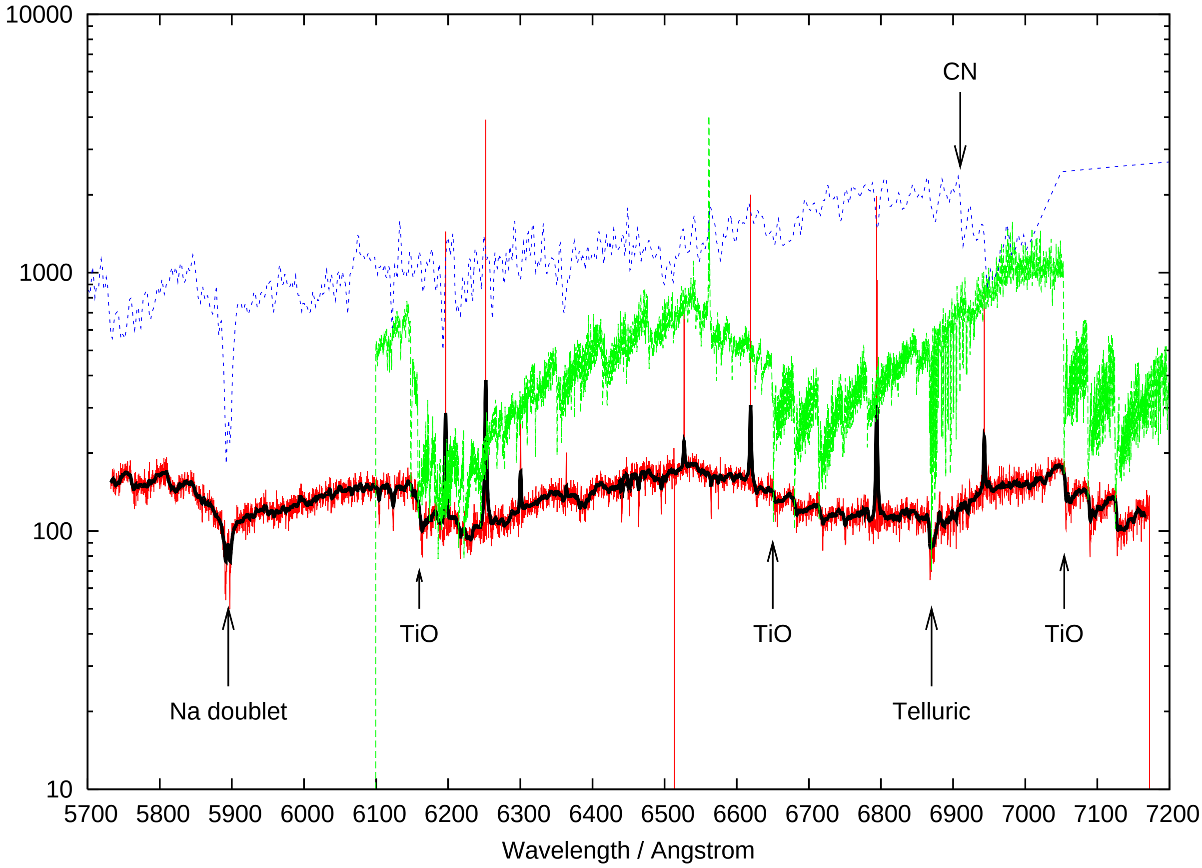

Figure 3.3: An example oxygen-rich stellar spectrum (red and black), from the VLT data, plotted against carbon- (blue) and oxygen- rich (green) templates with molecular features labelled. Cosmic rays have not been removed.

type identification. The oxygen-rich template used was the M7 giant 47tcx08 from McDonald and van Loon (2007), while the carbon-rich template was a C5 giant star. The molecular features already mentioned were used to identify the spectral types of the stars, as well as a further TiO complex around 6150 Å in the oxygen-rich stars. Figure 3.3 shows the spectrum of an oxygen-rich star plotted against the template stars.

3.1.3 Results

In the SAAO data 15 carbon-rich stars, 54 oxygen-rich stars and 15 stars of unknown type were determined, while in the VLT data 7 carbon-rich stars, 289 oxygen-rich stars and 719 unknown stars were determined. Some of the stars were observed with both telescopes and therefore, after accounting for these duplications, 1095 objects have been observed in total; 19 C-type stars, 342 M-type stars and 734 unknown stars.

The unknown spectra are flat and feature-less. It is assumed that these spectra belong to K-type stars. Our observations are contaminated with foreground stars from the Galactic bulge. The Galactic bulge displays a very old population of stars, therefore any more massive, hotter stars will have already died, leaving behind the cooler K-stars. The unknown spectra within the giant branch are expected to be from K-giants. K-type stars are the coolest stars which do not display molecular bands and O, B, A, F and G stars do not appear on the RGB. Therefore, any giant stars which do not show molecular absorption features will be K-type giant stars. However, it is worth noting that some of the classified K-type stars from the SAAO data may in fact be C- or M-type stars, but with poor signal-to-noise ratios making the identification of absorption lines not possible. Also, as can be seen in Figure 3.1, the absorption features in the wavelength ranges of interest are visually stronger in the oxygen-rich template than the template for the carbon-rich star. This could lead to an oxygen-rich bias within my identification results. However, as shown in Figure 3.5, the number of classified K-type stars present at the RGB tip (where carbon-rich stars begin to appear) is small. Therefore, any selection bias within the identification process will have a minimal effect.

More accurate spectral typing of M1, M2, etc. was hoped to be achieved. However due to time constraints this was not possible.

3.2 Colour–Magnitude Diagrams

Once the stellar type of each observed star has been determined, their $2MASS$ J and K band magnitudes are obtained and CMDs for each data set are plotted, see Figures 3.4 and 3.5.

The CMDs clearly show the giant branch of the Sgr dSph, extending from $K \approx 14$ up to the RGB tip around $K \approx 10$. The majority of M-type stars are located towards

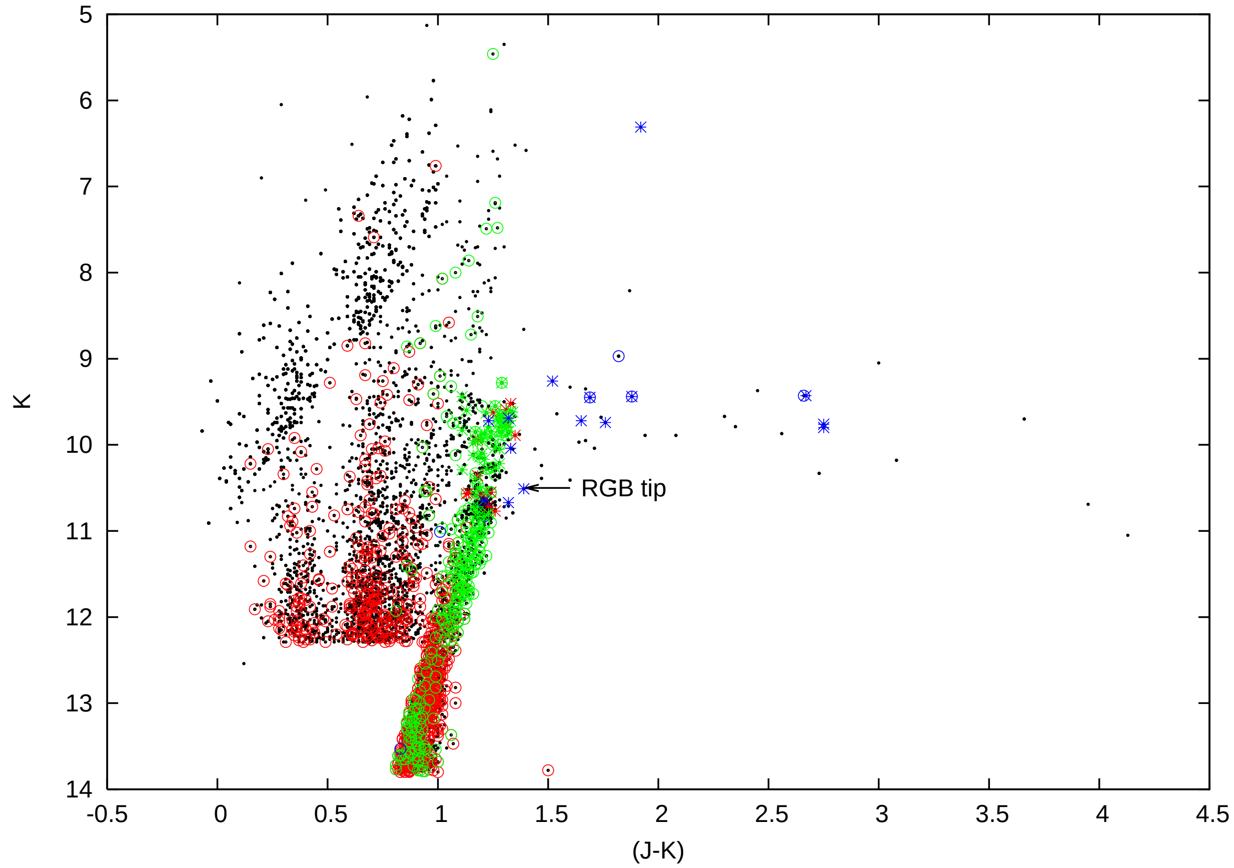

Figure 3.4: The colour–magnitude diagram of our data highlighting the C-type (blue), M-type (green) and K-type stars (red). SAAO data are indicated by asterisks and VLT data by open circles. The black dots denote all the stars within the fields of the Sgr dSph that were not observed.

the tip of the giant branch, while the K-type stars are most frequent towards the base of the giant branch and at lower $(J-K)$ values. The majority of K-type stars found to the left of the giant branch are expected to belong to the Galaxy, but this will need to be determined from their radial velocities, see Chapter 4. An exception to the spectral-type locations mentioned is a group of M-type stars positioned at the base of the giant branch. These will have to be investigated further.

Figure 3.5 shows a close up of the RGB tip and the AGB of the Sgr dSph. Above $K \approx 10.6$ there is a reduction in the number of stars, by a factor of around 4, thus the tip of the RGB is determined to be at $K \approx 10.6$. The AGB extends above the RGB tip

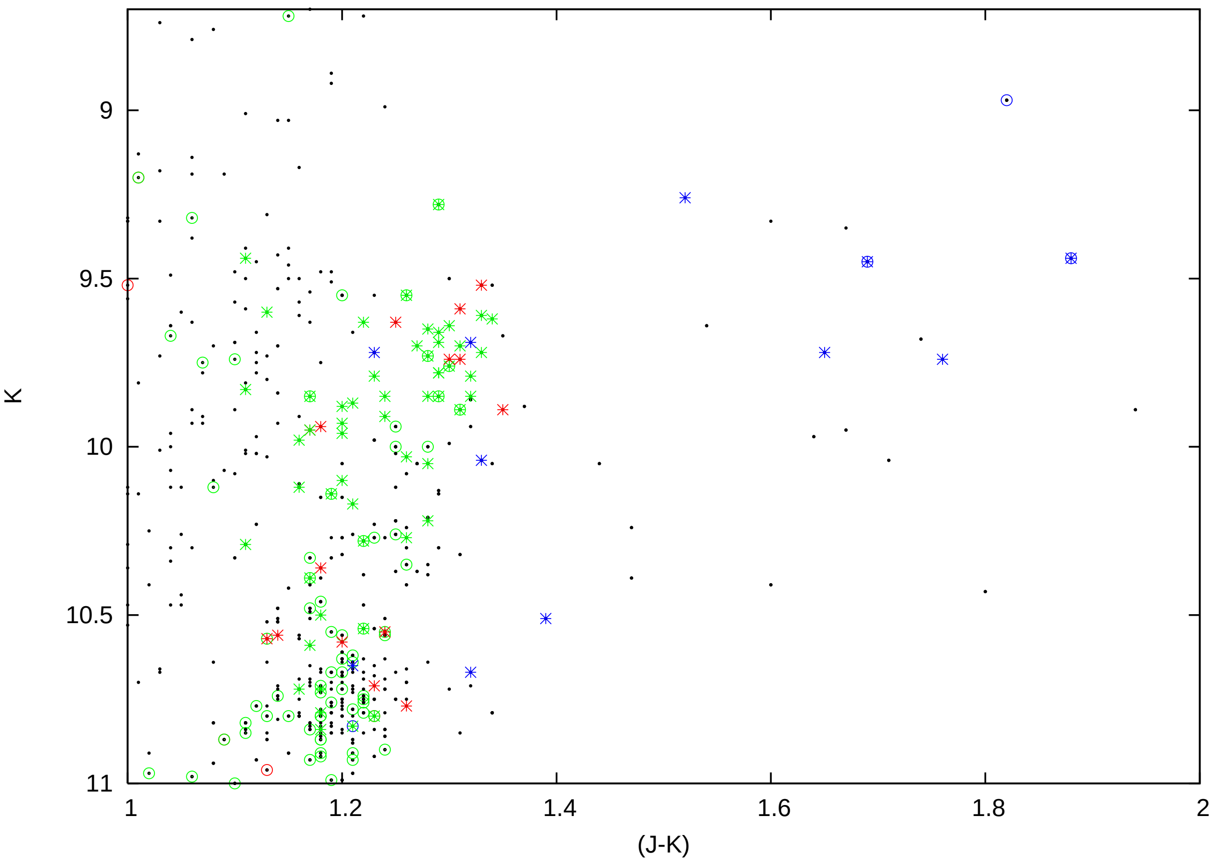

Figure 3.5: Colour–magnitude diagram, focused on the RGB tip and highlighting the carbon-ric C-type (blue), M-type (green) and K-type stars (red). SAAO data are indicated by asterisks and VLT data by open circles.

and rightwards as stars become redder.

As can been seen in Figures 3.4 and 3.5, the majority of observed carbon-rich stars are located at the tip of the RGB and beyond, extending to redder colours as they become progressively dust-enshrouded. Carbon stars appear redder than their oxygen-rich counterparts as the carbon-rich dust in their CSEs absorbs more blue light, see §1.1.4.

As discussed in §1.3, a higher C-type/M-type ratio is expected at the lower metallicities of the Sgr dSph, and therefore a greater number of carbon stars was expected within our observations. However, as can be seen in Figures 3.4 and 3.5, the CMDs show that a lot of the more reddened stars, which are expected to be carbon-rich, have

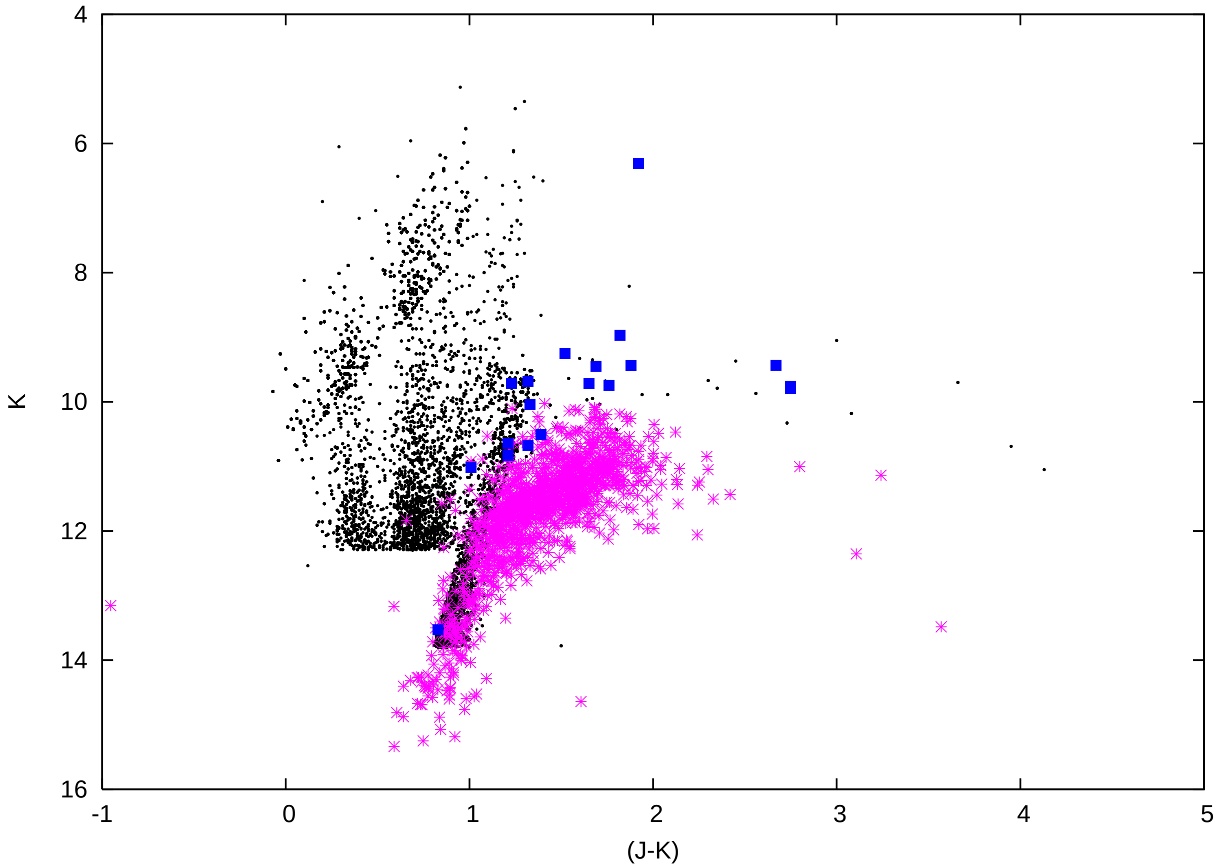

Figure 3.6: Colour–magnitude diagram displaying carbon-rich stars in the Sgr dSph (blue squares) and in the SMC (pink stars).

not been observed in this project. Also, some of the oxygen-rich stars may belong to the MW, not the Sgr dSph.

One exception to the clustering of C-stars towards the tip of the giant branch is observed. One carbon-rich star is located towards the base of the giant branch, with $(J-K)$ ~0.8, and K ~13.5. It is speculated that, rather than an 'intrinsic' carbon star formed through numerous dredge-up events, this is instead an 'extrinsic' carbon star. 'Extrinsic' carbon stars are formed in binary systems where their companions are late-stage carbon-rich AGB stars. Mass transfer from this carbon-rich companion causes the star to also become carbon rich. It is expected that the companion star is now a dull white dwarf. There is evidence for the creation of these 'extrinsic' carbon stars at low metallicity, from studies of carbon-enhanced metal-poor objects (CEMPs) in the Galaxy (Lucatello et al. 2005; Pols and Izzard 2006; Izzard et al. 2009) and of CH and barium (Ba) stars (McClure and Woodsworth 1990; North et al. 2000; Izzard et al. 2009). Research by Sneden et al. (2003) has also determined that blue, metal-poor stars only show carbon abundances if they are part of a binary system. Mowlavi (1998); Izzard and Tout (2004) have shown that the low luminosity carbon star tail observed in the MCs is due to 'extrinsic' C-type stars in binaries.

The CMD displays an 'odd' star observed at $(J - K) \approx 1.5$ and $K \approx 13.8$. After re-checking the spectrum of this star, it is determined that this isn't a K-type star, but is in fact a galaxy. Using SIMBAD it was identified as 2MASX J18521545-2948214. Therefore, the number of total observed stars is 1094; 19 C-type stars, 342 M-type stars and 733 K-type stars.

3.2.1 Carbon Stars in the Small Magellanic Cloud

Figure 3.6 displays the known carbon stars in the SMC on the CMD of the Sgr dSph. These carbon stars are from the Rebeirot et al. (1993) catalogue and have been cross-correlated with $2MASS$ to find their J and K magnitudes (Lagadec et al. 2007). As is evident in Figure 3.6, the carbon stars in the Sgr dSph form at similar $(J - K)$ values to those in the SMC but at brighter K magnitudes. The difference in K magnitudes between carbon stars in the Sgr dSph and the SMC is due to the fact that the SMC is further away than the Sgr dSph. The SMC has a distance modulus of 18.91 (Hilditch et al. 2005), whereas the Sgr dSph has a distance modulus of 17.1 (Monaco et al. 2004). Therefore, the SMC carbon stars are shifted by $\sim$1.81 magnitudes on the CMD of the Sgr dSph data.

4

Radial Velocities

Due to the location of the Sgr dSph, behind the Galactic Bulge, our observations are contaminated by foreground Galactic stars. In order to deduce which stars belong to the Sgr dSph, the radial velocities of the observed stars are determined. This Chapter will outline how these velocities are found and comment on the Sgr dSph stars that have been identified.

The radial velocities have only been determined for the VLT data. The spectra from the SAAO observations do not have sufficiently high signal-to-noise ratios to accurately find these radial velocity values.

4.1 Determining the Radial Velocities

In order to determine the radial velocities of our observed stars, object spectra are cross-correlated with template spectra. The object spectrum is compared with a template spectrum to find the radial velocity at which the spectra coincide. The calculated velocity shifts are then corrected for the velocities of the template stars and the heliocentric radial velocity variations.

The Starlink applications `istat`, `clip`, `setmagic` and `hcross` are used. As discussed in §2.3, the automatic GIRAFFE data reduction does not remove cosmic rays from the data images. Therefore, `istat`, `clip` and `setmagic` are used to account for this, as follows. The mean flux and standard deviation in the spectrum are identified using `istat` and any pixels with a value higher than 3σ are selected using `clip`, as these will probably be cosmic rays. The clipped pixels are then set as bad pixels, which are ignored by any subsequent programme, using `setmagic`.

Once this has been completed the data are cross-correlated using `hcross`. Bright, red template stars of each type are selected and `hcross` cross-correlates a data file with the template spectrum of the correct type (K-, M- or C-), returning the shift between the two spectra. The template stars used are (in J2000.0 coordinates): SGR_P2893, at $18^h54^m29^s.73$ $-30°11'21''.86$, for M-type spectra; SGR_P3550, at $18^h57^m21^s.77$ $-30°47'58''.4$, for C-type spectra and SGR_00397, at $18^h54^m41^s.68$ $-30°43'11''.10$, for K-type spectra. The relevent template is used for each spectral type, as each spectral type has different molecular features in its stellar spectra. Different wavelength regions are selected for each of the spectral types, focusing on strong spectral features. Tables 4.1, 4.2 and 4.3 present the different wavelength ranges chosen. The final output from running `hcross` is ~30 radial velocity shifts for each star, one for each wavelength range.

The average radial velocity shift for each star is derived using an iteratively-clipped

Table 4.1: The wavelength ranges (in Å) used to cross-correlate the K-type spectra.

L614.2	L682.2	H651.5B	H710.5
5766 – 5790	6445 – 6461	6389 – 6405	6938 – 6954
5843 – 5864	6487 – 6508	6415 – 6431	6971 – 6987
5884 – 5905	6554 – 6571	6443 – 6459	7006 – 7022
5971 – 5991	6622 – 6639	6490 – 6507	7030 – 7046
6049 – 6070	6734 – 6760	6554 – 6570	7059 – 7075
6355 – 6375	6833 – 6850	6587 – 6604	7078 – 7095
6443 – 6460	6973 – 6989	6606 – 6622	7118 – 7135
6488 – 6507	7076 – 7093	-	7142 – 7158

Table 4.2: The wavelength ranges (in Å) used to cross-correlate the M-type spectra.

L614.2	L682.2	H651.5B	H710.5
5750 – 5840	6472 – 6546	6384 – 6402	6984 – 7006
5800 – 5850	6545 – 6593	6411 – 6429	7030 – 7053
5860 – 5960	6590 – 6650	6447 – 6465	7055 – 7090
5938 – 6027	6650 – 6750	6472 – 6488	7075 – 7090
6070 – 6147	6746 – 6849	6543 – 6560	7086 – 7125
6355 – 6412	6931 – 6988	6577 – 6593	7112 – 7126
6380 – 6450	7004 – 7084	6591 – 6607	7125 – 7159
6410 – 6474	7086 – 7160	-	-

Table 4.3: The wavelength ranges (in Å) used to cross-correlate the C-type spectra.

L614.2	L682.2	H651.5B	H710.5
5735 – 5761	6492 – 6513	6387 – 6403	6951 – 6967
5773 – 5801	6540 – 6560	6424 – 6440	6976 – 6992
5832 – 5863	6670 – 6688	6448 – 6464	7039 – 7055
5884 – 5914	6737 – 6755	6492 – 6508	7082 – 7098
5928 – 5949	6786 – 6807	6540 – 6556	7114 – 7130
5975 – 5997	6943 – 6968	6562 – 6584	7129 – 7145
6132 – 6148	7013 – 7035	6590 – 6606	-
-	7084 – 7103	-	-

median. First, the median radial velocity is calculated. All median values are found to be between $-200 < v_{rad} < 300$ km s^{-1}, and most are well within these values. Therefore, any velocities outside of this range are discarded. The median values and the standard deviation (σ) are calculated again. Any value that varies from the median by greater than 2.2σ is rejected and the new median value is found. This process is repeated until the median stabilises. Any sources which still display high σ values are analysed further. If greater than 20% of the velocity values lie within 10 km s^{-1} of the median then the outlying velocities are ignored and the iteration is run again. The final uncertainty on the radial velocity value is determined to be σ.

The majority of objects have $\sigma < 10$ km s^{-1}, however 147 objects still have high σ values. Therefore, accurate radial velocities could not be determined for these 147 stars. See §4.2.

The measured radial velocities must be corrected for the radial velocities of the template stars. The template spectra were visually cross-correlated with theoretical model spectra. The `marcs` (Gustafsson et al. 1975, 2008) model atmosphere for a K-type star, with T= 4000 K, log(g)= 1.5, [Z/H]= −1.5 and [α/Fe]= 0.3, was used to determine template radial velocity corrections of −17, +92 and +105 km s^{-1}, for K, M and C stars respectively. These values are estimated to be accurate to ±2 km s^{-1}.

Once the radial velocities of the template spectra have been determined, the next step is to correct for the heliocentric variation, due to the motion of the Earth around the Sun. To do this the Starlink routine `rv` (Wallace and Clayton 1996) was used. This returns the heliocentric corrections for a given location and time. The observations taken in September have a heliocentric correction of 29.20 km s^{-1}, while the heliocentric corrections for the observations in June have a value of −5.00 km s^{-1}. These values do vary within each observation, but only by $< \pm$ 0.25 km s^{-1}, which is less than the estimated error from the cross-correlation of the template spectra with theoretical models.

To get the final radial velocity values for our observations, the heliocentric corrections are added to the average measured velocity and the template radial velocity corrections are subtracted. The result is multiplied by −1 to account for sign convention variations within the different cross-correlation methods. No radial velocity standard stars were observed. Therefore, it is assumed that an average Sgr dSph star has a radial velocity of v_{rad} = 141 km s^{-1} (Ibata et al. 1997). Our radial velocity measurements are corrected by +84 km s^{-1} to account for this and to correct for the atmospheric

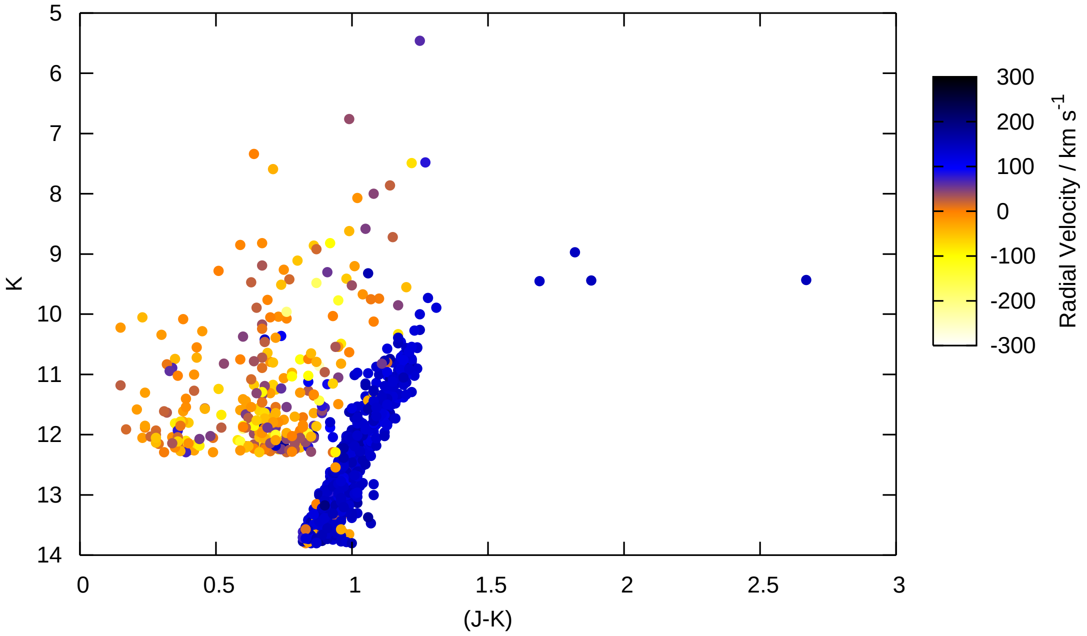

Figure 4.1: CMD displaying the radial velocity range of stars with accurate radial velocities.

refractive index.

Figure 4.1 shows the CMD, from §3.2, plotted again with a colour palette corresponding to the radial velocities. It is found that, as expected, our observations belong to two clear populations. The objects selected in the giant branch mostly belong to the Sgr dSph, with radial velocities ranging from ∼95 to ∼180 km s^{-1}, while the majority of K-giants belong to the Galaxy with radial velocities in the range ~ -100 to ∼80 km s^{-1}.

As shown in Figure 4.2, a small number of K-type stars observed with lower $(J-K)$ values are shown to have radial velocities which group them with the Sgr dSph stars. It might be the case that some Galactic stars coincidentally have the radial velocities that are associated with the Sgr dSph, although from the observed range in radial velocities this is unlikely. These stars could be: post-AGB stars in the Sgr dSph, if they have

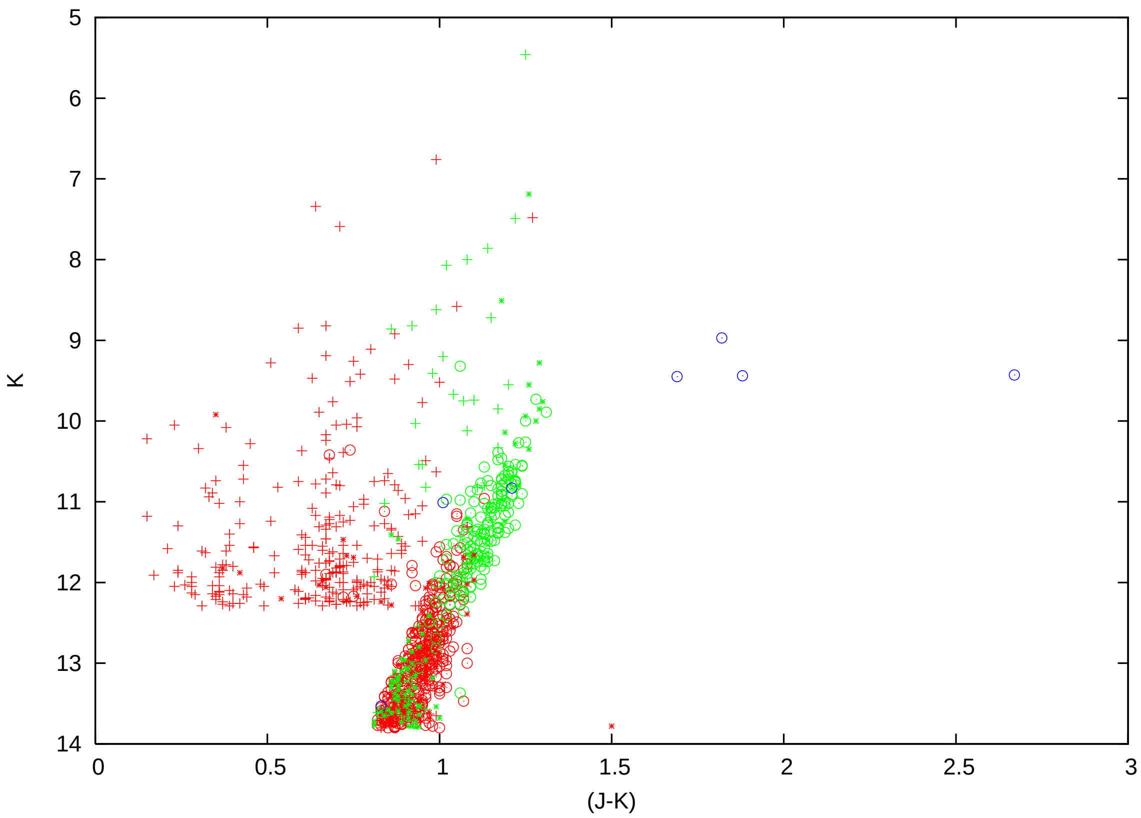

Figure 4.2: CMD displaying Galactic stars (crosses), Sgr dSph stars (open circles) and stars of undetermined velocity (asterisks), with their stellar types; C-type (blue), M-type (green) and K-type (red).

similar luminosities to the AGB tip; contact binaries, if they display twice the expected luminosity (or K_{bol} + 0.7); giant or main sequence binaries in the Galaxy, with unusual radial velocities; Galactic Halo stars, which have similar radial velocities to the Sgr dSph but are closer to us, or stars belonging to the Sgr dSph, but that do not belong to the bulk population. These stars have to be studied further to determine their origin.

4.2 Radial Velocity Errors

The radial velocity error values are plotted against K magnitude and the determined radial velocities, in Figures 4.3 and 4.4, respectively. These Figures clearly show two populations: 85.5% of stars have radial velocities accurate to $< \pm 10$ km s^{-1}, while

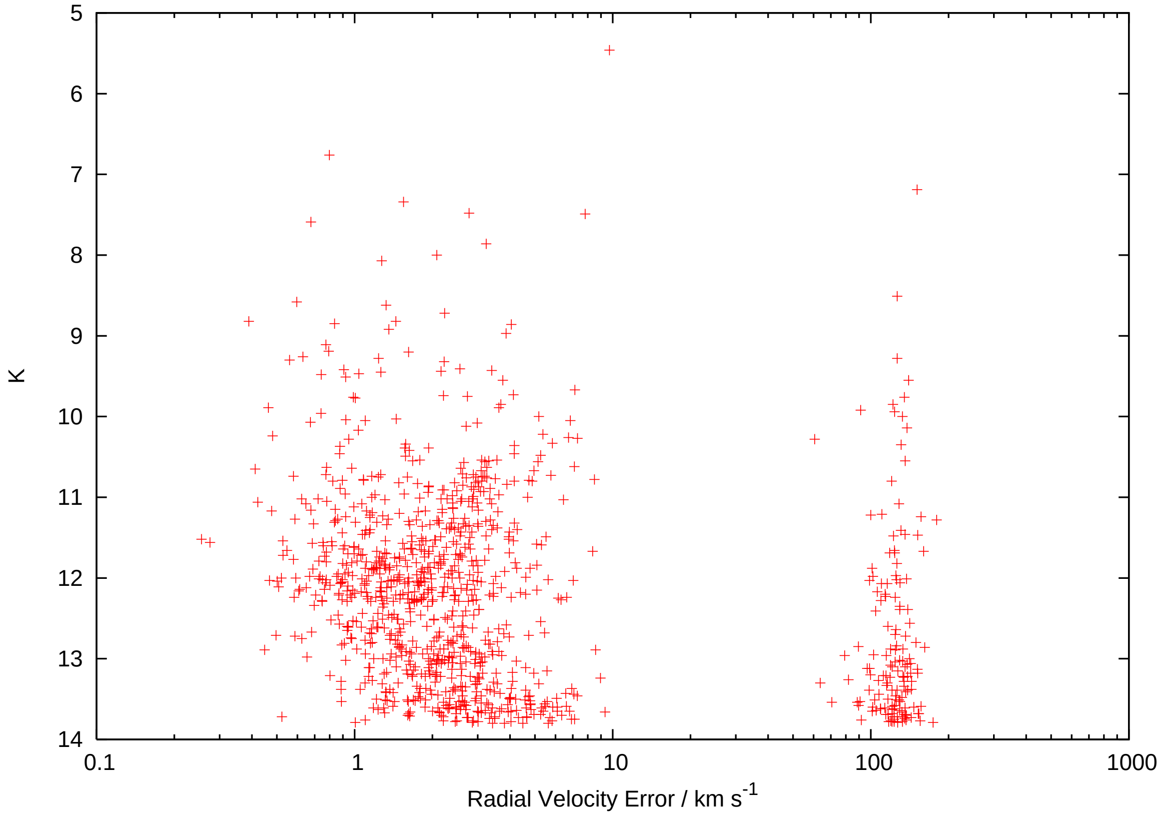

Figure 4.3: Radial velocity error values plotted against K magnitude.

the remaining 147 stars have very large error values. These stars have relatively poor signal-to-noise ratios in their spectra, which is likely due to poor fibre placement on the spectrograph. This causes the cross-correlation to fail.

Figure 4.3 shows how the error values increase slightly towards fainter magnitudes, although there is not a huge increase. The accuracy of our radial velocities is therefore limited by the spectral features used for cross-correlation, and the signal-to-noise ratio of the spectrum, more than it is by the stellar magnitude.

The quantisation of the large radial velocity errors around $\sigma \sim 150$ km s^{-1}, that can be seen in Figure 4.4, can be attributed to the poor signal-to-noise ratios of the spectra of these stars. The cross-correlation of the template stars with these spectra will produce random cross-correlation function results, therefore the σ values from these results will cluster together. After discarding all velocity results outside of the range $-200 < v_{rad} < 300$ km s^{-1} the length of our spectra is 500 km s^{-1}, leading to a

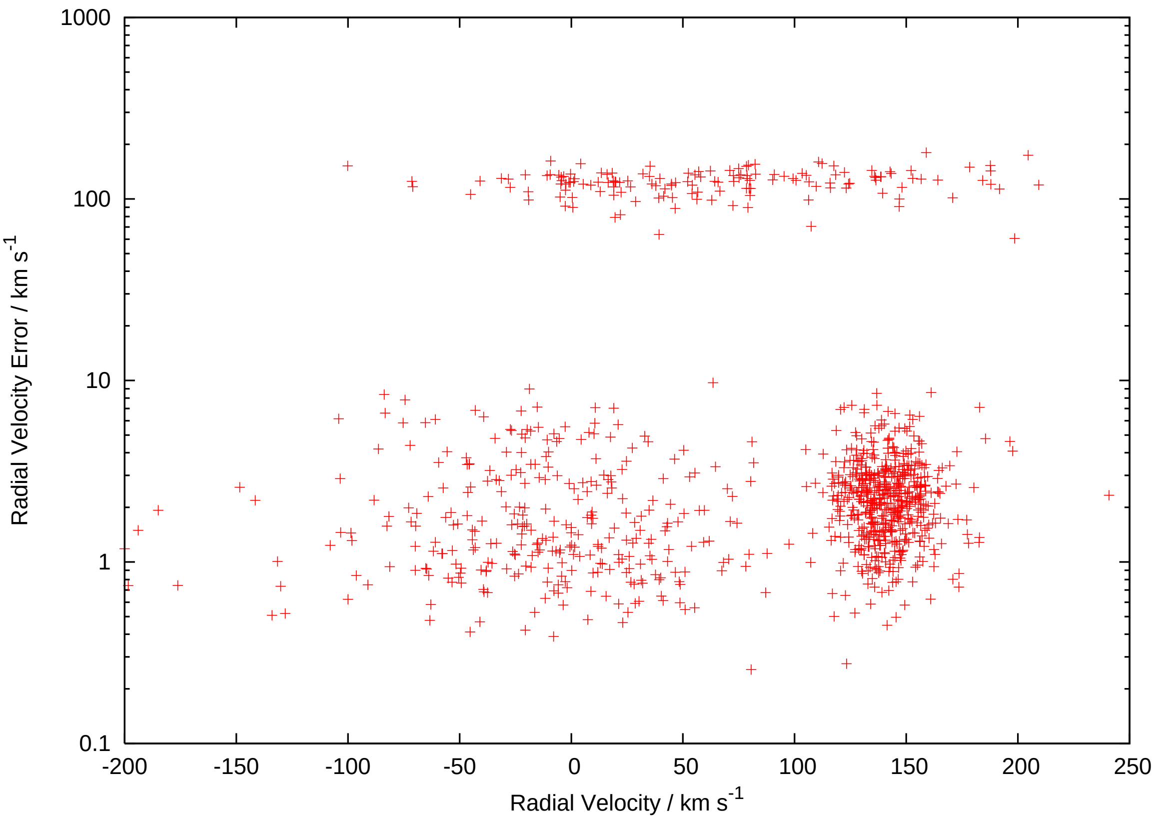

Figure 4.4: Radial velocity error values plotted against the radial velocities determined from each filter value.

value of $\sigma \approx 170$ km s^{-1}.

A systematic offset of approximately 6 km s^{-1} (~0.5 pixels) has been discovered between the radial velocities of the M- and K-type stars. This variation is due to the wavelength regions chosen for the cross-correlation. The selection of the wavelength ranges affects this systematic error so it is not removed.

4.3 Radial Velocity Ranges

Figure 4.5 clearly displays the two radial velocity populations of the data. Any star with a radial velocity greater than 95 km s^{-1} is classified as belonging to the Sgr dSph, while any star with a radial velocity less than 95 km s^{-1} is determined to be Galactic. The Galactic stars have an average radial velocity of -13 km s^{-1}, with a dispersion of

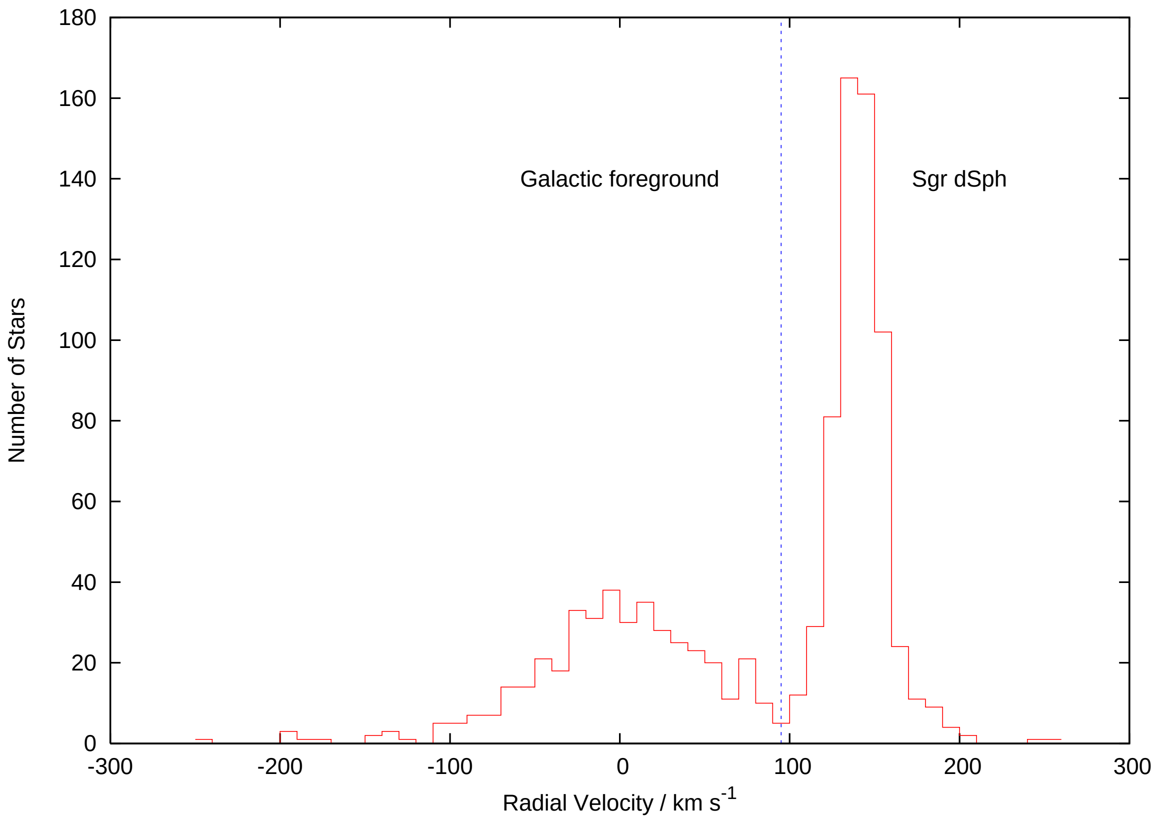

Figure 4.5: A histogram displaying the range in radial velocities of our data.

53 km s^{-1}. The Sgr dSph stars exhibit a peak in their distribution at 141 km s^{-1}, with a dispersion of 15 km s^{-1}. As described in §4.1 our measured velocities were corrected to the average value for Sgr dSph radial velocities found in the literature, to account for the lack of radial velocity standard stars observed. Giuffrida et al. (2010) determine that the heliocentric radial velocities of stars in the Sgr dSph fall in the range $120 < v_{rad} < 180$ km s^{-1}, with a peak at ~140 km s^{-1}, while Ibata et al. (1997) determine an average Sgr dSph radial velocity of 141 km s^{-1}, with a dispersion of 13 km s^{-1}. Furthermore, Zijlstra and Walsh (1996) determined the radial velocities of two PNe within the Sgr dSph, as 132.9 km s^{-1} and 133.9 km s^{-1}, consistent with the velocity of the Sgr dSph being 140 ± 10 km s^{-1}. Our dispersion of Sgr dSph radial velocities is slightly greater than the average published value in the literature. This could be due to a greater uncertainty in determining the radial velocities, or it could be indicative of the region of the Sgr dSph observed in this study having a larger intrinsic radial velocity

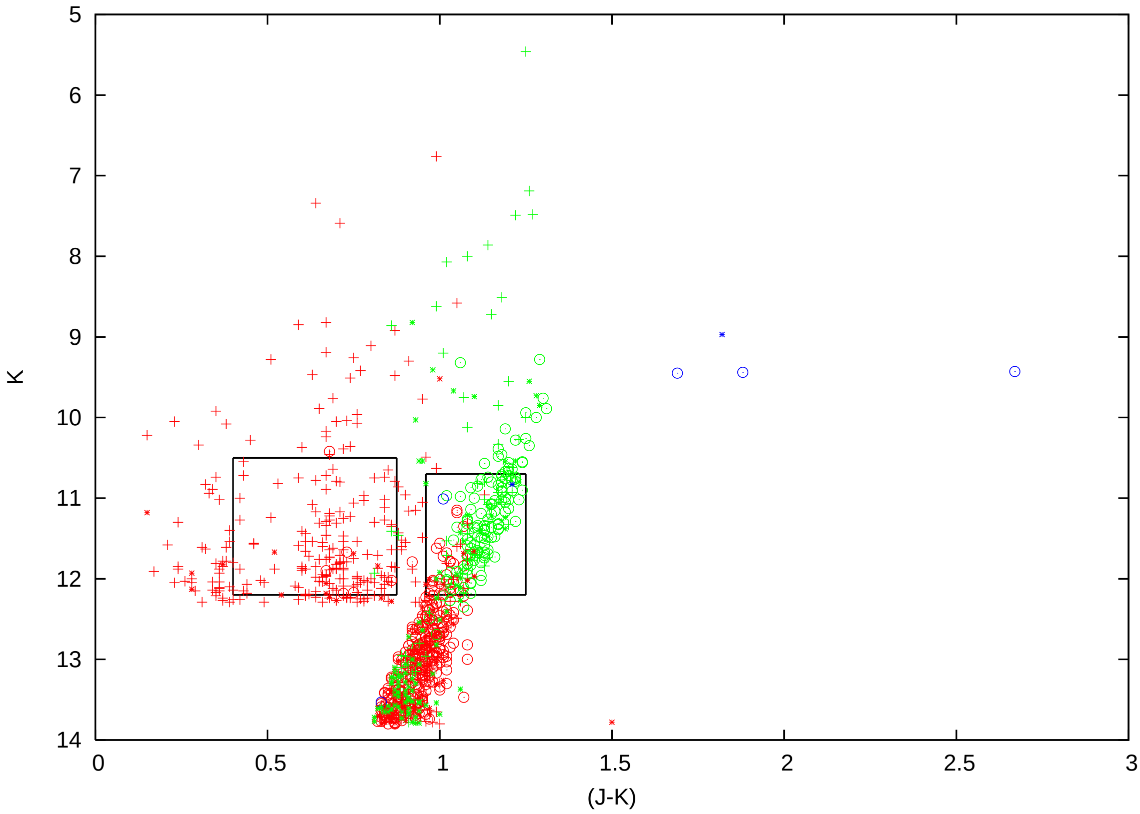

Figure 4.6: Displaying the regions of the CMD plotted in Figure 4.7.

variation.

The radial velocity distributions for the stars belonging to the colour-selected giant branch of the CMD and for the rest of the population, as outlined in Figure 4.6, are displayed in Figure 4.7. Figure 4.7(a) shows the radial velocity range for the stars assumed to belong to the Galactic foreground. The section of the CMD was deliberately chosen to include the stars recorded at Sgr dSph velocities. The Galactic foreground stars display a radial velocity peak at -5 km s^{-1}, with a dispersion of 65 km s^{-1}. Figure 4.7(a) shows that the stars at the velocities of the Sgr dSph might belong to the tail of the Galactic radial velocity distribution. The radial velocity errors on these values are small, therefore it is unlikely that these stars belong to the main Galactic population unless they are binary stars or Galactic Halo stars, as discussed in §4.1. If they are members of the Sgr dSph, they are not part of the bulk population.

The histogram of the radial velocities determined for stars on the colour-selected

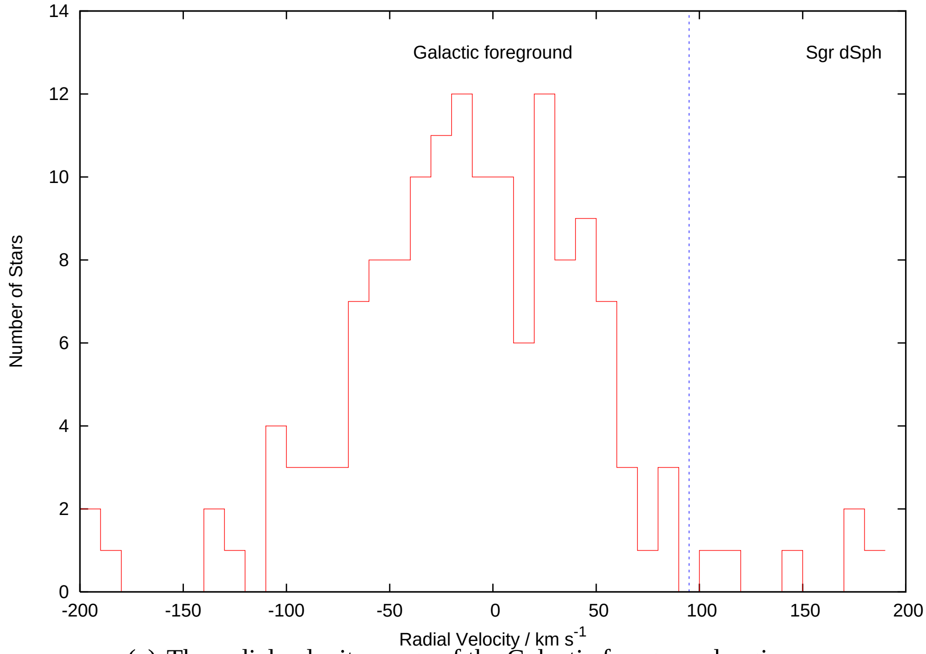

(a) The radial velocity range of the Galactic foreground region.

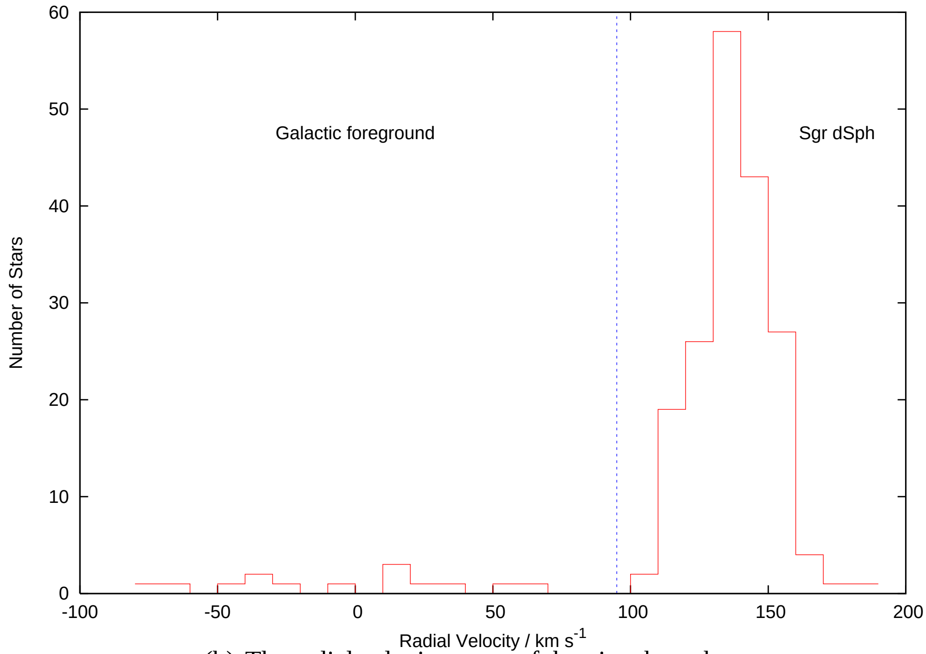

(b) The radial velocity range of the giant branch.

Figure 4.7: The radial velocity ranges for stars with $(J-K)$ and K values placing them within the Galactic foreground region, Figure (a), and the red giant branch, Figure (b).

giant branch displays two populations, see Figure 4.7(b). It is evident that the vast majority of stars on the giant branch belong to the Sgr dSph, with a radial velocity peak at 140 km s^{-1}, and a dispersion of 10 km s^{-1}. A smaller population of stars is present within the Galactic radial velocity range determined in Figures 4.5 and 4.7(a).

As discussed in §3.2, and as is evident in Figures 4.2 and 4.6, there is a cluster of 63 M-type stars located at the base of the giant branch. Accurate radial velocities have been determined for 19 of these stars: 8 belong to the Sgr dSph, while 11 have radial velocities placing them within the Galaxy. These Galactic stars may be foreground M-type dwarfs.

5

The Hertzsprung–Russell Diagram

In order to determine where on the AGB stars can become C-rich, and how long this C-rich phase lasts, a Hertzsprung–Russell (H–R) diagram is produced for our observations, and then compared to theoretical isochrones. Before this can be achieved, the bolometric luminosities of our stars must be calculated from their observed J and K magnitudes. This Chapter will describe how the H–R diagram is produced and present the results of comparing this diagram with model isochrones.

5.1 Plotting the Hertzsprung–Russell Diagram

The bolometric corrections to the K magnitude are calculated from Table 5 of Houdashelt et al. (2000) for the M- and K-type stars, and are determined by the stars' $(J - K)$ colours. It is assumed that the majority of our stars belong to the main population of the Sgr dSph, therefore having a metallicity of [Fe/H] = −0.55. It is also assumed that at the tip of the RGB log(g) = 0, therefore the stars are sorted using:

- $K < 10$, log(g) = 0.0,
- $10 \leq K < 11$, log(g) = 0.5,
- $11 \leq K < 12$, log(g) = 1.0,

- $12 \leq K < 13$, log(g) = 1.5,
- $13 \leq K < 14$, log(g) = 2.0.

Houdashelt et al. (2000) have not derived bolometric corrections for the $2MASS$ J and K filters. Therefore, the Carpenter (2001) colour corrections:

$$(J - K)_{2MASS} = (0.972 \pm 0.006)(J - K)_{BB} + (-0.011 \pm 0.005) \quad (5.1)$$

$$K_{2MASS} = K_{BB} + (0 \pm 0.005)(J - K)_{BB} + (-0.044 \pm 0.003) \quad (5.2)$$

must first be applied, to relate the Houdashelt et al. (2000) Johnson-Glass $(J - K)$ colour to the $2MASS$ $(J - K)$ colour.

The bolometric corrections to the C-type stars are calculated using the bolometric correction equation for carbon stars derived by Kerschbaum et al. (2010). This paper does not provide values for T_{eff}, therefore a bolometric table derived from Aringer et al. (2009)[1] is used to find the T_{eff} values. However, the effective temperature for the carbon-rich stars will be inaccurate as these reddened stars' photospheric radii change with wavelength, thus the definition of an effective temperature is redundant. A stellar mass of 2 $M_{\odot}$ is assumed for the determination of T_{eff} from the Aringer et al. (2009) bolometric correction table, as there are not enough results at 1 $M_{\odot}$, along with values of log(g) = 0.0 and Z = 0.33, although the assumed metallicity and gravity have much smaller effects on T_{eff} and K_{bol} than the $(J - K)$ colour. The Aringer et al. (2009) bolometric correction tables do not provide T_{eff} values for the high $(J - K)$ values reached by four of our carbon stars. However, the models reach a maximum $(J_{corr} - K_{corr})$ for T_{eff} = 3000 K and K_{corr} = 3.08, so this value is assumed for the carbon stars with $(J - K) > 1.45$. K_{corr} is the bolometric correction to the K magnitude.

The observed J and K magnitudes must also be corrected for the distance of the Sgr dSph and for any reddening effects. A distance modulus of $(m - M)_0 = 17.10 \pm 0.15$ mag, corresponding to a heliocentric distance of 26.30 ± 1.8 kpc, from Monaco

[1]The bolometric correction table for determining T_{eff} for the C-type stars is available at http://stev.oapd.inaf.it/synphot/Cstars/cphot08.html

et al. (2004) is used and a reddening of $E(B-V) = 0.14 \pm 0.03$ mag from Layden and Sarajedini (2000). Using the Rieke and Lebofsky (1985) relations of:

$$A_J = 0.871E(B-V) \tag{5.3}$$

and

$$A_K = 0.346E(B-V), \tag{5.4}$$

extinction values of $A_J = 0.122$ mag and $A_K = 0.048$ mag are determined.

The bolometric K magnitudes are worked out using the following equation:

$$K_{bol} = K_{obs} + K_{corr} - A_K - (m-M)_0 \tag{5.5}$$

Once the bolometric K magnitudes have been found, the stars' luminosities are calculated, using:

$$\frac{L}{L_\odot} = 10^{\frac{M_\odot - K_{bol}}{2.5}}. \tag{5.6}$$

Figure 5.1 shows the H–R diagram for all our observations. The SAAO data, for which radial velocities could not be determined, are assumed to belong to the Sgr dSph. As shown in Figures 4.7, stars with $(J-K)$ colours and K magnitudes which place them on the giant branch are very likely to belong to the Sgr dSph, due to the small range in radial velocities recorded there.

As can be seen in Figure 5.1, when plotted on the H–R diagram, the carbon-rich stars shift to temperatures ~400 K less than the M- and K-type stars. In general carbon stars are cooler than oxygen-rich stars, plus they are usually dusty which also makes them appear cooler, as they are obscured at optical wavelengths which shifts their temperatures lower. However, this shift on the H–R diagram may be due to the fact that a different set of bolometric corrections are used for the carbon stars, and these could be a poor match for the bolometric corrections used for the rest of the stellar population. Also, as mentioned previously, the definition of an effective temperature becomes redundant for the reddened carbon stars.

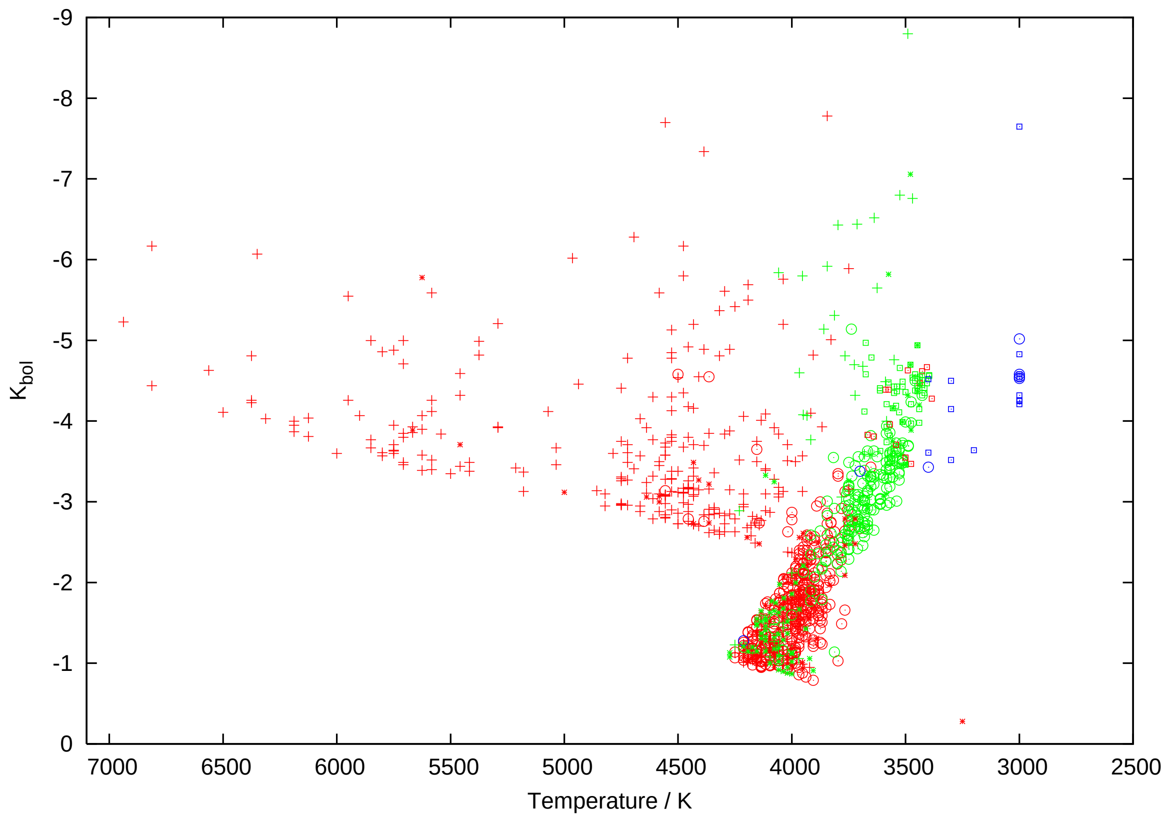

Figure 5.1: Hertzsprung–Russell diagram displaying Galactic stars (crosses), Sgr dSph stars (open circles), SAAO stars of undetermined velocity (open squares) and the VLT stars with inaccurate velocities (asterisks), with their stellar types: C-type (blue), M-type (green) and K-type (red).

5.2 Isochrone Fitting

Once the H–R diagram has been produced for our observations, it is compared to theoretical isochrones in order to investigate the evolution of giant stars in the Sgr dSph.

The Dartmouth stellar evolution models are used (Dotter et al. 2007, 2008) and isochrones are plotted for each of the metallicity populations of the Sgr dSph. The parameters used for each isochrone are outlined in Table 5.1. From the literature, values of [α/Fe] $\approx$ 0.0 (Smecker-Hane and McWilliam 2002; McWilliam and Smecker-Hane 2005) and [α/Fe] = -0.17 (Monaco et al. 2005) were found. Smecker-Hane and McWilliam (2002) and McWilliam and Smecker-Hane (2005) noted that a higher

Table 5.1: Parameters used for the Dartmouth isochrone models.

Name	[Fe/H]	[α/Fe]	Age (Gyr)
isochrone1	–0.55	–0.2	8
isochrone2	–0.55	0.0	8
isochrone3	–0.70	–0.2	8
isochrone4	–0.70	0.0	8
isochrone5	–0.40	–0.2	8
isochrone6	–0.40	0.0	8
isochrone7	–0.25	0.0	1
isochrone8	–0.25	–0.2	1
isochrone9	–0.25	0.0	2.5
isochrone10	–0.25	–0.2	2.5
isochrone11	–2.00	0.2	10
isochrone12	–2.00	0.4	10
isochrone13	–2.00	0.2	11
isochrone14	–2.00	0.4	11
isochrone15	–2.00	0.2	12
isochrone16	–2.00	0.4	12
isochrone17	–2.00	0.2	13
isochrone18	–2.00	0.4	13

value of [α/Fe] $\approx$ 0.3 is apparent in more metal-poor populations ([Fe/H] < -1.0). Synthetic horizontal branch (SHB) models[2] are also produced using the Dartmouth system and the parameters for each model are listed in Table 5.2. The data are also plotted against Pisa evolutionary track models[3] (Castellani et al. 2003; Cariulo et al. 2004); the parameters for each track are listed in Table 5.3.

[2] The Dartmouth isochrones and SHB models are available from http://stellar.dartmouth.edu/ models/webtools.html

[3] The Pisa evolutionary track models are available from http://astro.df.unipi.it/SAA/PEL/Z0.html

Table 5.2: Parameters used for the Dartmouth synthetic horizontal branch models.

Name	[Fe/H]	[α/Fe]	Horizontal Branch Mass ($M_\odot$)
SHB1	–0.55	–0.2	0.6
SHB2	–0.55	0.0	0.6
SHB3	–0.55	–0.2	0.7
SHB4	–0.55	0.0	0.7
SHB5	–0.55	–0.2	0.8
SHB6	–0.55	0.0	0.8
SHB7	–0.55	–0.2	0.9
SHB8	–0.55	0.0	0.9
SHB9	–0.55	–0.2	1.0
SHB10	–0.55	0.0	1.0
SHB11	–0.55	0.0	1.1
SHB12	–0.55	0.0	1.2
SHB13	–0.55	0.0	1.3

Table 5.3: Parameters used for the Piso evolutionary tracks. The standard helium abundances are used, and the tracks are modelled with no overshooting.

Name	Z	Mass ($M_\odot$)
track1	0.004	1.2
track2	0.004	1.0
track3	0.008	1.2
track4	0.008	1.0

Figure 5.2 displays the model isochrones for the bulk population of the Sgr dSph plotted on the H–R diagram for the Sgr dSph giant branch. All the models fit the luminosity of the RGB tip well, with the lower metallicity limit models at higher tem-

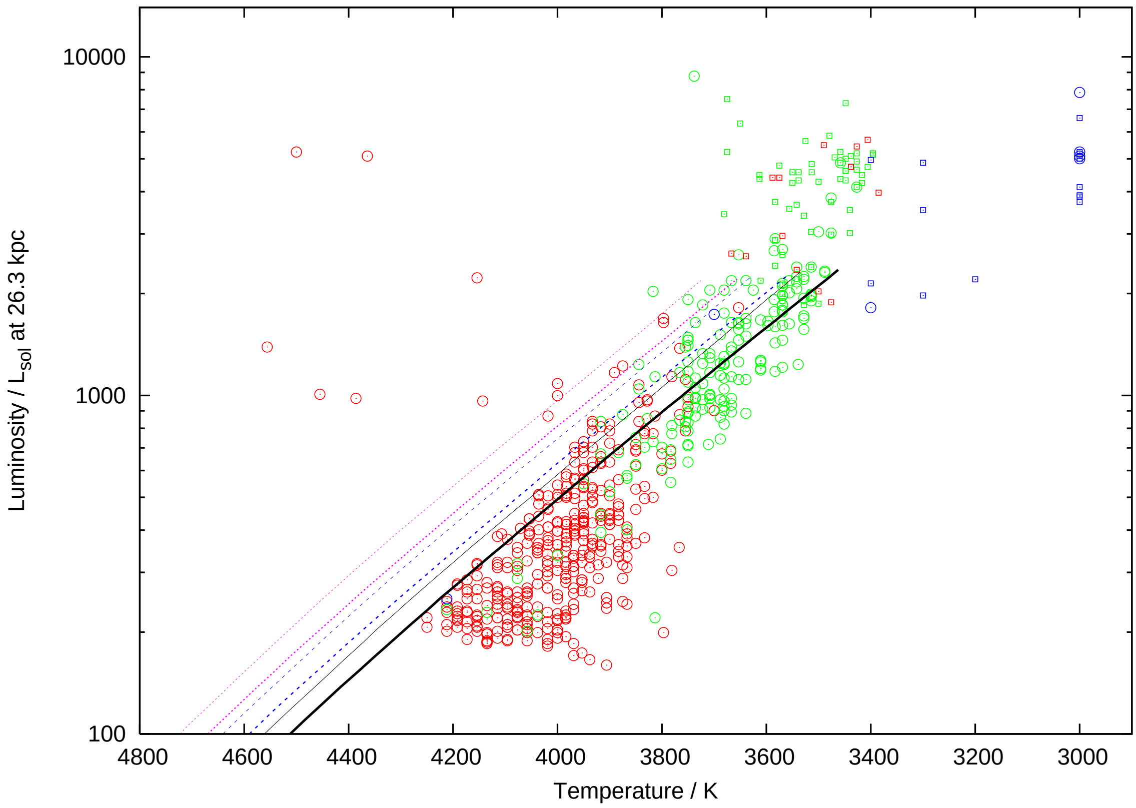

Figure 5.2: Hertzsprung–Russell diagram, in solar luminosities, of radial velocity members of the Sgr dSph, with the model isochrones for the bulk population of the Sgr dSph plotted. Isochrones are plotted, from left to right, at [Fe/H] = −0.70 (pink lines), [Fe/H] = −0.55 (blue lines) and [Fe/H] = −0.40 (black lines). [α/Fe] values of −0.2 are represented by the thinner lines, while [α/Fe] = 0.0 are the thicker lines. The best fitting isochrone, isochrone6, is the thick black line. The symbols are determined as in Figure 5.1.

peratures than the higher metallicity limit models. A higher value of [α/Fe] shifts the isochrones to lower temperatures. The thick black line in Figure 5.2 is the best fitting model, isochrone6, at [Fe/H] = −0.40 and [α/Fe] = 0.0. This indicates that the stars that have been observed exhibit metallicities towards the metal-rich end of the published bulk population metallicity range.

The isochrones are also plotted on the CMD to see whether the corrections used to determine K_{bol} and T_{eff}, and thus $L/L_{\odot}$, are correct. The isochrones fit the main body of the giant branch better on the CMD than the H–R digram, especially towards the

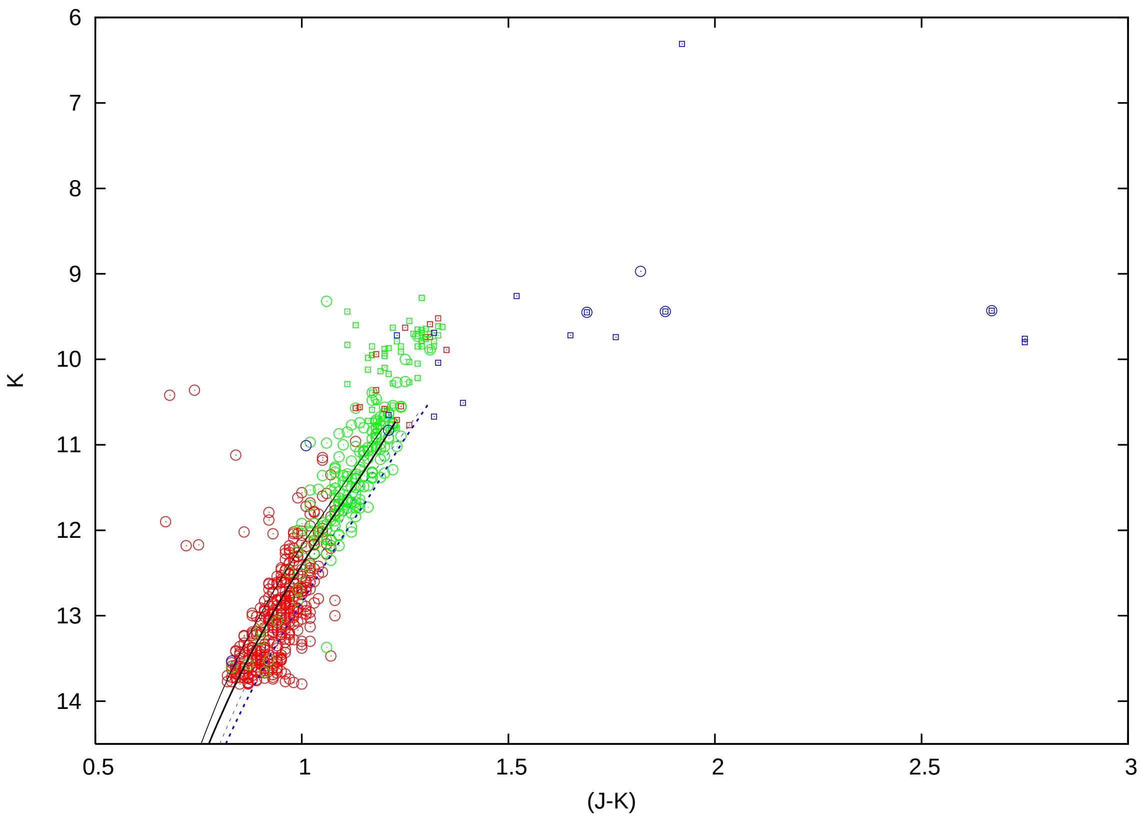

Figure 5.3: CMD with the model isochrones, showing the range of metallicity of the bulk population of the Sgr dSph; [Fe/H] = −0.70 (black line) to [Fe/H] = −0.40 (blue line). The [α/Fe] values are distinguished as in Figure 5.2, the symbols as in Figure 5.1.

base of the observed giant branch; this suggests that the corrections used may not be as accurate at lower luminosities and higher temperatures. Figure 5.3 displays isochrones for the published metallicity range of the main population of the Sgr dSph. The width of the isochrone distribution matches the width of the observed giant branch, indicating that this metallicity range is appropriate.

Figures 5.2 and 5.3 display a difference in gradient between the observed giant branch and the modelled giant branch. As this slope is evident in both diagrams it is concluded that it is inherent in the data, not a result of corrections, and therefore, that the Dartmouth isochrone model RGB gradient is in error. This gradient may also have been artificially enhanced by the colour cut imposed when selecting our targets.

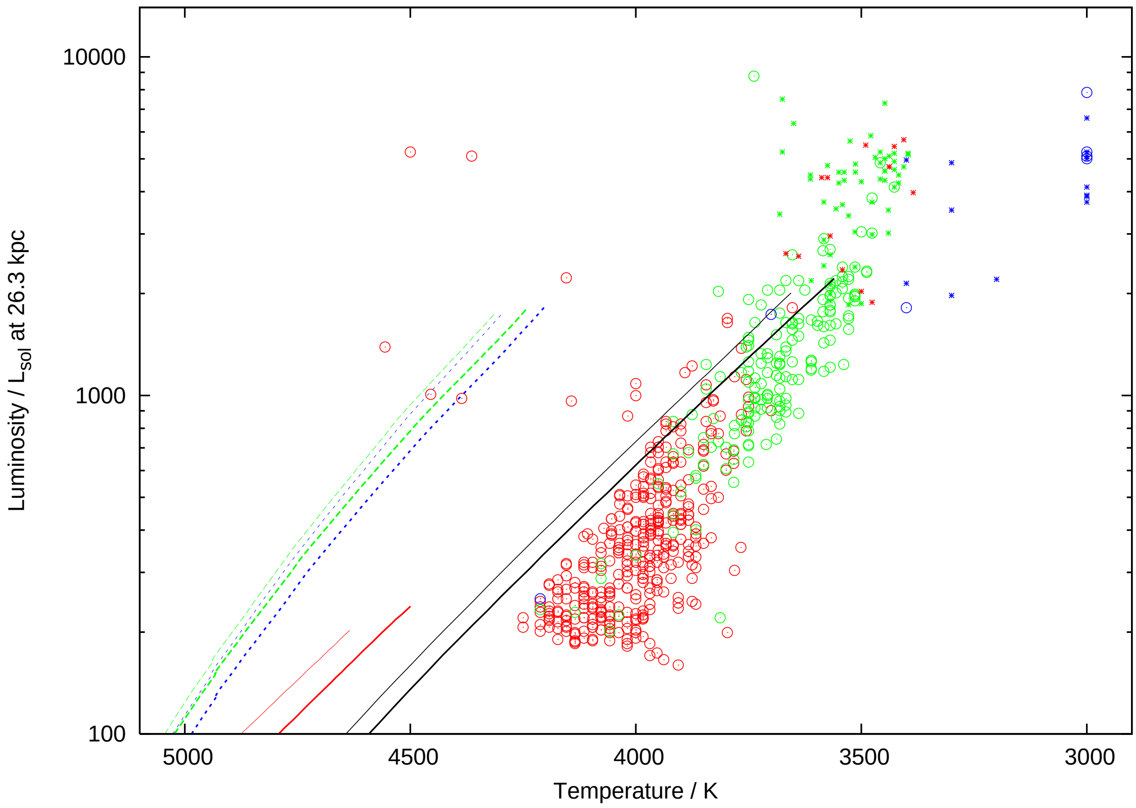

Figure 5.4: Hertzsprung–Russell diagram with the model isochrones for the metal-poor (dashed lines) and metal-rich (filled lines) populations of the Sgr dSph. Models are displayed, from left to right, for 10 Gyr (green), 13 Gyr (blue), 1 Gyr (red) and 2.5 Gyr (black) populations. Again the lower [α/Fe] values are thinner. The symbols are determined as in Figure 5.1.

Figure 5.4 shows the metal-poor models plotted with our observations. The RGB tip for these low metallicity models falls near the region of the K-type stars mentioned in Chapter 4.1, which have radial velocities classifying them as Sgr dSph stars, but which are of undetermined origin. It is therefore suggested that these stars belong to the metal-poor population of the Sgr dSph. In the metal-poor models, an increase in stellar age moves the RGB to lower temperatures and to slightly higher luminosities, and an increase in [α/Fe] causes the RGB to jump to lower temperatures. However, due to the spread in our observations at these values of L/T_{eff}, which age and [α/Fe] assumptions are correct cannot be commented on.

The size of the metal-poor population can be estimated from the CMD. As shown

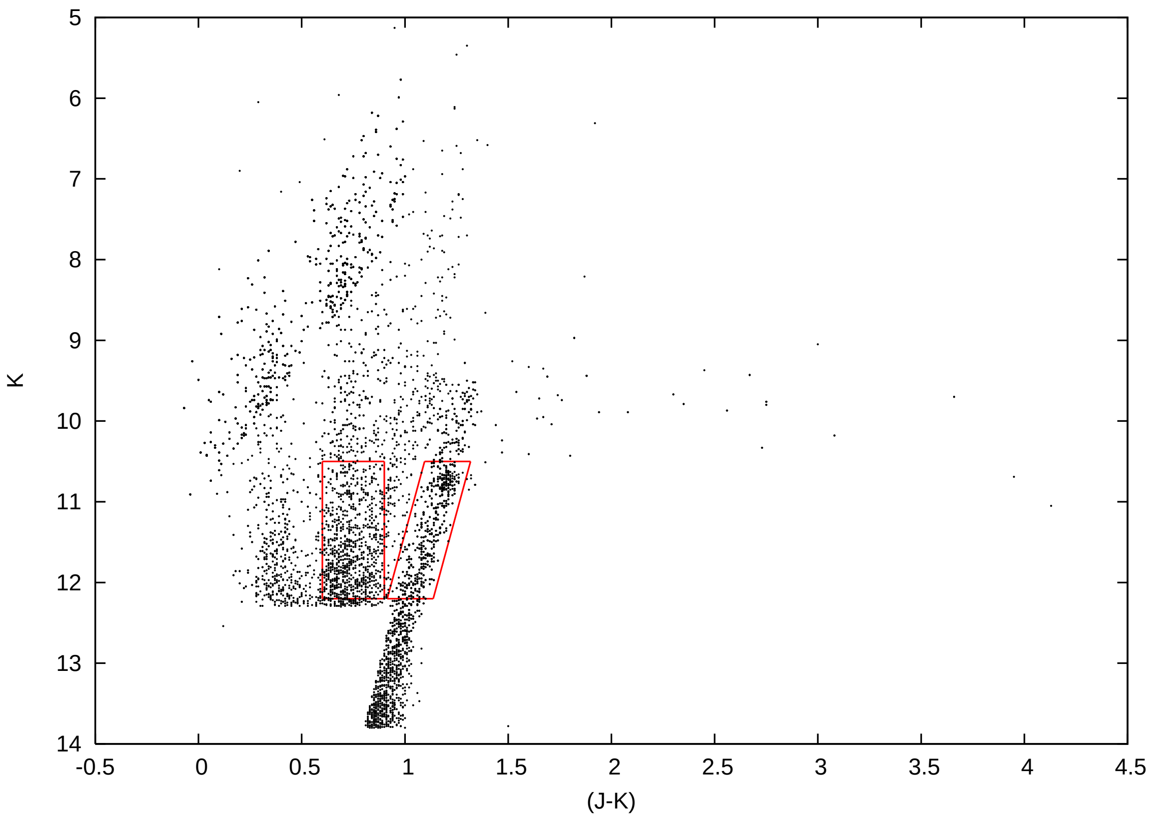

Figure 5.5: CMD of all the 2*MASS* objects within the Sgr dSph fields, showing the regions used to determine to size of the metal-poor population.

in Figure 5.5, two regions are selected; one on the giant branch of the bulk population and the other to include the stars belonging to the metal-poor population. The fraction of Sgr dSph to Galactic stars within each box is calculated and then multiplied by the total number of objects within the regions, to determine the confusion rates. It is found that the bulk population is approximately 11 times more populous than the metal-poor population.

The metal-rich population of the Sgr dSph is also displayed in Figure 5.4. Bonifacio et al. (2004) determine an age for this metal-rich population of 1 Gyr. However, as shown in Figure 5.4, the isochrone of this age misses all of the observations in this thesis. The modelled RGB tip barely reaches the base of our observed giant branch. Therefore, as no stars have been observed at this L/T_{eff}, it cannot be determined whether this age estimation is accurate. Layden and Sarajedini (2000); Zijlstra

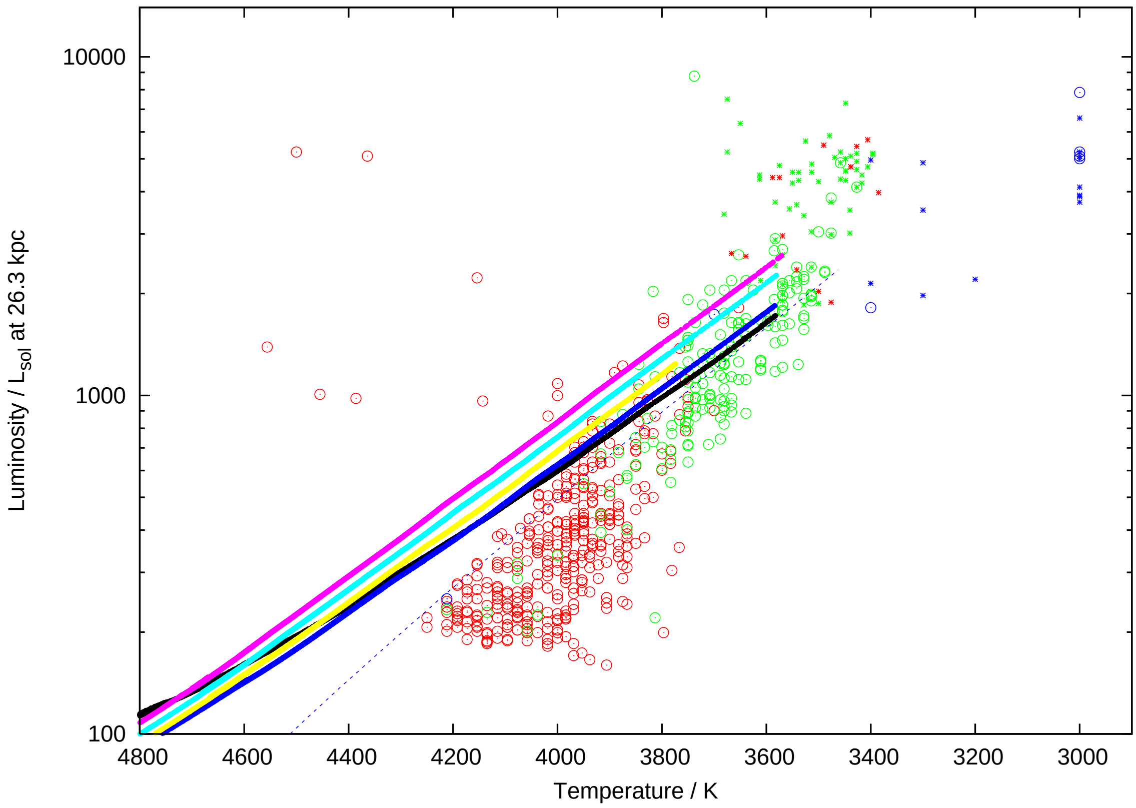

Figure 5.6: Hertzsprung–Russell diagram with the synthetic horizontal branch models for a range of horizontal branch masses, from bottom to top; 0.6 $M_{\odot}$ (black), 0.8 $M_{\odot}$ (blue), 0.9 $M_{\odot}$ (yellow), 1.0 $M_{\odot}$ (cyan) and 1.1 $M_{\odot}$ (pink). The best fitting isochrone (blue dashed line) is also displayed to indicate the location of the RGB tip. The symbols are determined as in Figure 5.1.

et al. (2006a) suggest an estimate for the age of the metal-rich population to be 2.5 Gyr. These isochrones compare better with the observed data, although do fall to the left of the observed giant branch. This indicates that some of the observed stars may belong to the metal-rich population of [Fe/H] = −0.25.

Synthetic horizontal branch (SHB) models from Dotter et al. (2007, 2008), for increasing HB masses, are plotted on Figure 5.6. These models only plot up to the onset of thermal pulses on the AGB, hence they do not reach the peak luminosities of our data. Increasing the HB mass increases the luminosity of the modelled start of the TP-AGB. An 8 Gyr star on the AGB will have a main sequence turn off age of ~7.27 Gyr, after taking into account an HB lifetime of ~10% of the MS lifetime and an RGB

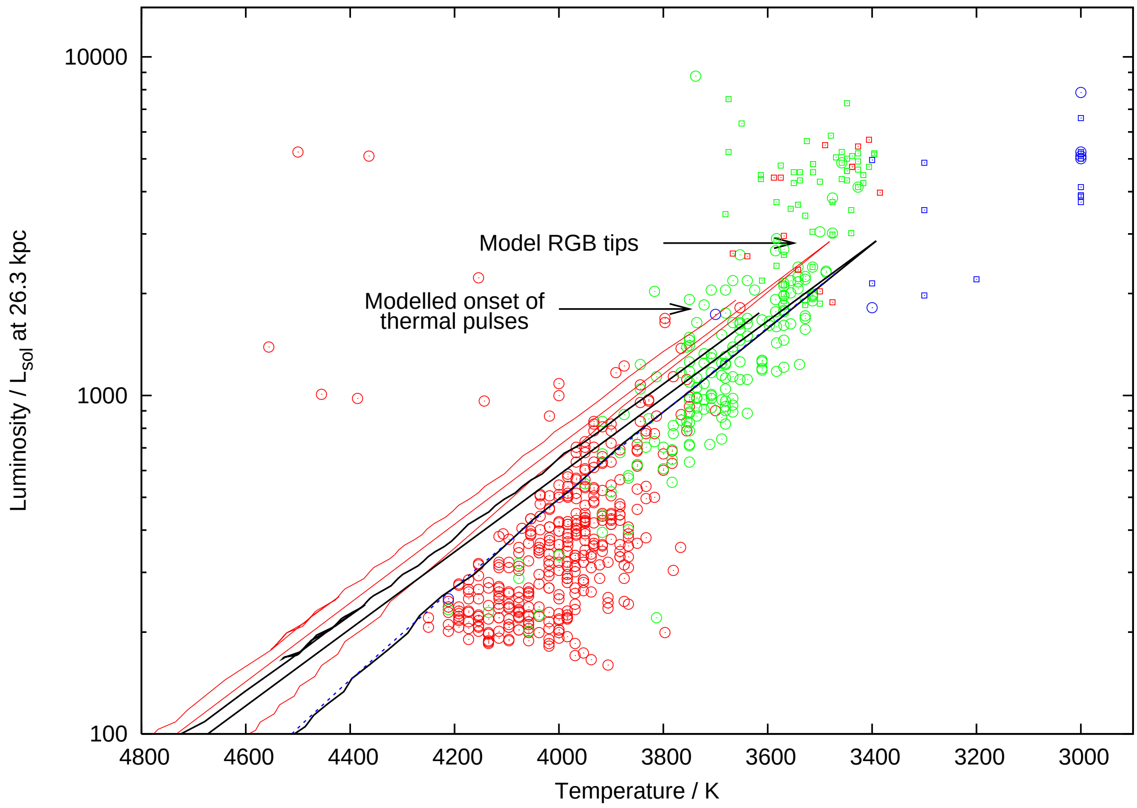

Figure 5.7: Hertzsprung–Russell diagram with the best fitting evolutionary track models, from left to right; track3 (red) and track4 (black). The modelled RGB tip and the beginning of the TP-AGB are labelled. The best fitting isochrone (blue dashed line) is also displayed to indicate the location of the RGB tip. The symbols are determined as in Figure 5.1.

lifetime of a few million years. Therefore, the maximum possible HB mass of this star on the AGB, if it experiences no RGB mass loss, is $\sim$1.11 $M_{\odot}$. Figure 5.6 displays the SHB models up to 1.1 $M_{\odot}$, although the 0.9 $M_{\odot}$ track does not model to the low temperatures reached by the others.

The SHB models SHB2, SHB6 and SHB8 all predict the onset of thermal pulses to occur below the RGB tip, and therefore below the carbon stars located around the RGB tip. This implies that these stars are 'intrinsic' carbon stars rather than 'extrinsic' carbon stars, see §3.2.

The Pisa evolutionary track models (Castellani et al. 2003; Cariulo et al. 2004) have also been used to plot our observations. However, their grid means that the choice of parameters is more limited. The best fits are found with track3 and track4, as plotted in Figure 5.7, with Z = 0.008 ([Fe/H] = −0.38) and M = 1.2 $M_\odot$ or M = 1.0 $M_\odot$, respectively. These evolutionary tracks model the RGB tip at slightly too high luminosities. However, they do predict that the TP-AGB will begin below the RGB tip, as suggested by the SHB models in Figure 5.6, therefore providing further evidence for the carbon stars to be 'intrinsic'.

There is one exception to the assumption of the carbon stars around luminosities of the RGB tip being 'instrinsic'. The carbon star located at T_{eff} = 3700 K and $L \sim 1700$ $L_\odot$ may still be 'extrinsic'.

The Pisa model RGB falls to the left of our observed giant branch, especially at the lower luminosities and higher temperatures towards the base of the RGB. As this is consistent with all the models, but less prominent in the CMD displayed in Figure 5.3, it is suggested that the determination of T_{eff} by J and K magnitudes is less successful at these higher temperatures. At higher temperatures both the J and K magnitudes lie on the Rayleigh-Jeans tail of the spectral energy distribution (SED). Therefore, for all $T_{eff} \gtrsim 4500$ K, $(J - K)$ tends to zero.

The RGB tip is reproduced at correct luminosities by each of these models, apart from the Pisa evolutionary tracks for which limited variables are available. Therefore, the distance modulus and reddening estimates assumed earlier in this section appear to be correct.

The best fitting isochrone model and Pisa evolutionary tracks both have metallicity values at the upper end of the bulk population metallicity range. This implies that the observed stars are at a slightly higher metallicity than expected (Lagadec et al. 2008; Giuffrida et al. 2010). However, the width of the giant branch in the CMD closely matches the metallicity range of the isochrone models, therefore suggesting that the assumed metallicity range is correct, and that the shift to higher metallicities is due to the corrections used.

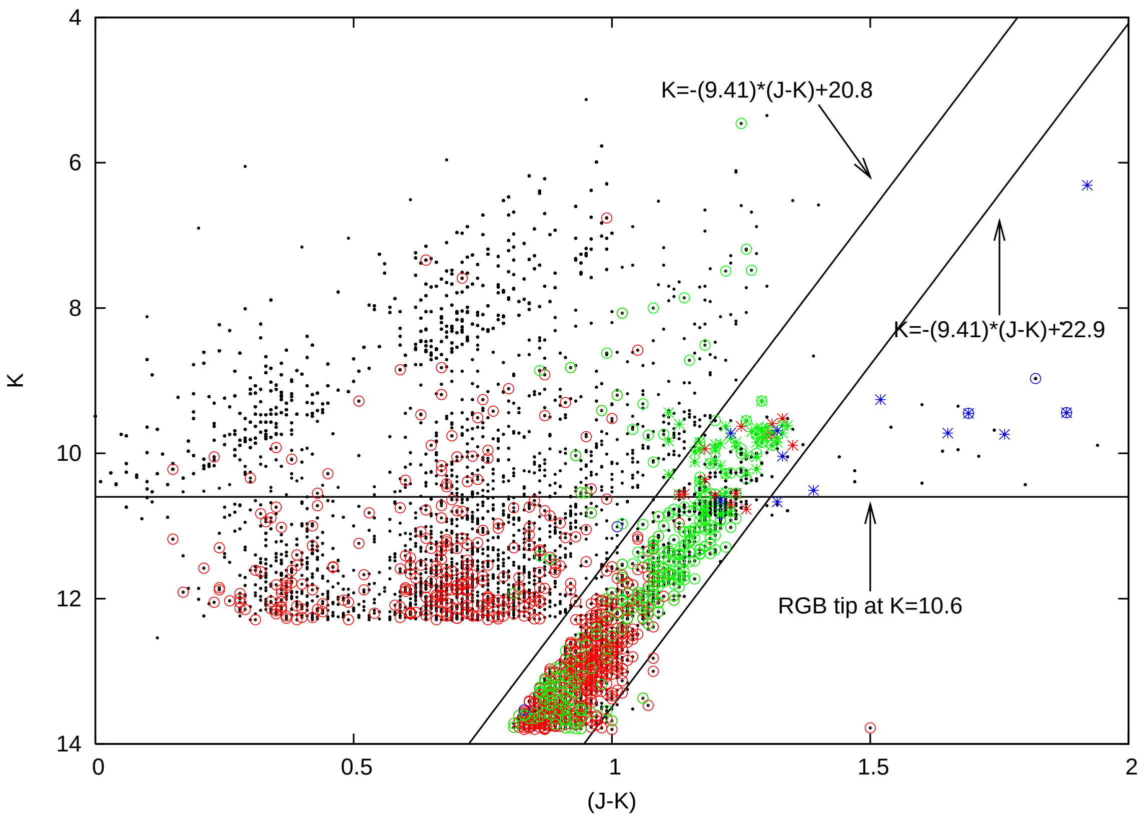

Figure 5.8: CMD highlighting the colour cuts made to count the number of stars on the RGB and on the AGB. The symbols are as in Figure 3.4.

5.3 Carbon Stars in the Sagittarius Dwarf Spheroidal

From the Pisa evolutionary tracks (Castellani et al. 2003; Cariulo et al. 2004), the average lifetime of carbon stars in the Sgr dSph can be estimated. The difference in the age of a star at the RGB tip (10.6 ± 0.05 mag) and the age at $K = 11.6 \pm 0.05$ mag, further down the RGB is determined, from the Pisa isochrones, to be 382595 years. A colour cut is introduced to identify stars on the giant branch, as presented in Figures 5.8 and 5.9, and the number of stars redwards of the line $K = -(9.41) \times (J - K) + 20.8$ and between the above two K magnitudes is counted. 238 stars are found within this 1 magnitude range. The number of stars between the RGB tip and the AGB tip (at $K = 9.28$), and within the imposed colour cuts, is found to be 127. These values are corrected to account for the ratio of the radial-velocity-determined Galactic and Sgr

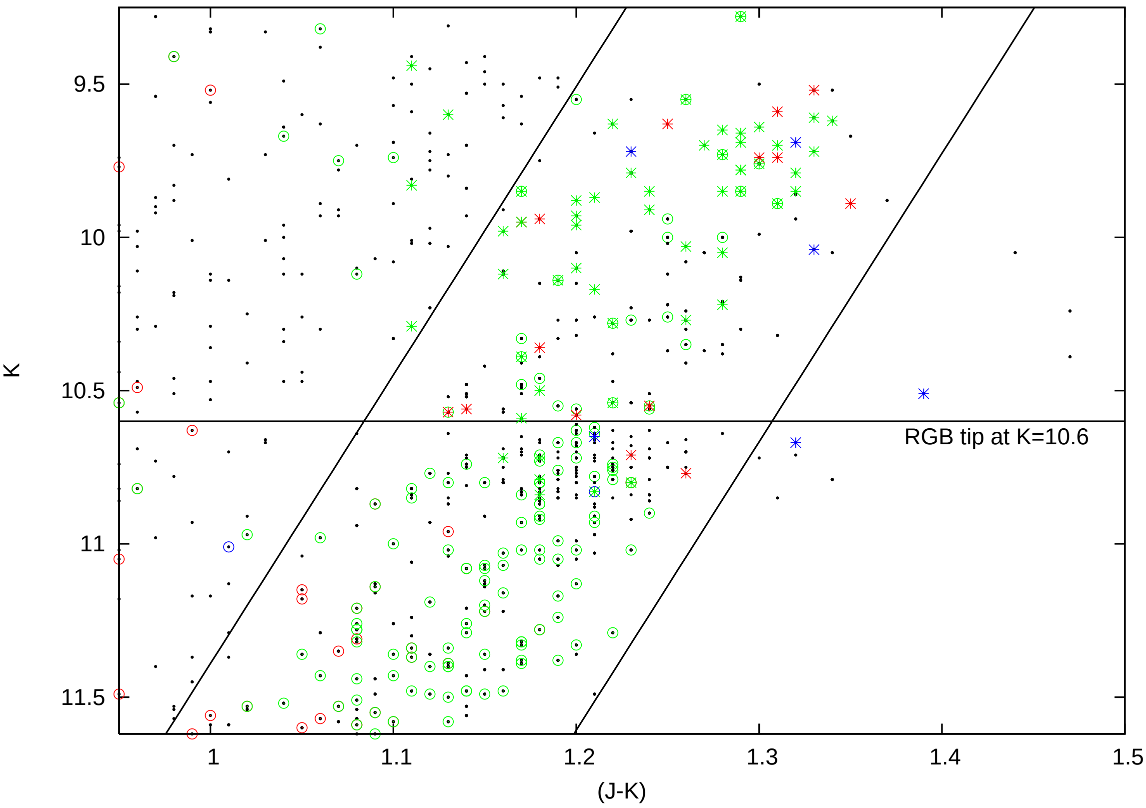

Figure 5.9: A close up of the tip of the giant branch highlighting the colour cuts made to count the number of stars on the RGB and on the AGB. The symbols are as in Figure 3.4.

dSph stars, to $N_{RGB,S} \approx 229$ stars, and $N_{AGB,S} \approx 102$ stars, where $N_{RGB,S}$ is the number of stars on the RGB and in the Sgr dSph and $N_{AGB,S}$ is the number of stars on the AGB and in the Sgr dSph. The ratio of the calculated number of RGB and AGB stars in the Sgr dSph is used to determine a maximum lifetime of AGB stars above the RGB tip of $\tau_{AGB} \approx 382595 \times \frac{N_{AGB,S}}{N_{RGB,S}} \times 1.32$ mag ≈ 226013 years. The *calculated* maximum C-rich lifetime of an AGB star is $\tau_C \approx 382595 \times \frac{N_{AGB,S}}{N_{RGB,S}} \times 1.57 \approx 268819$ years. All stars redwards of the line, $K = -(9.41) \times (J-K) + 22.9$, and with $K < 12$, are assumed to be carbon rich. The $\frac{C}{(C+M)}$ ratio above the RGB tip is therefore $\frac{37}{93}$, leading to an *average* lifetime of a carbon star in the Sgr dSph of $< \tau_C > \approx \tau_C \times \frac{C}{(C+M)} \approx 1.07 \times 10^5$ years.

The carbon star at $(J-K) = 1.92$ and $K = 6.3$ is assumed to belong to the foreground Galactic population.

Thermal pulses occur on the TP-AGB every $10^4 - 10^5$ years (Zijlstra 2006) and as our observations are towards the lower mass limit of AGB stars, it is assumed that their interpulse periods will be $\sim 10^5$ years. This is confirmed by Karakas and Lattanzio (2007), who determine an interpulse time of 1.43×10^5 years for a 1 $M_\odot$ star of Z = 0.004 ([Fe/H] = −0.68, at the lower end of the expected metallicity distribution of the main Sgr dSph population). This model includes an assumed mass-loss law. The 1 $M_\odot$ model at Z = 0.008 ([Fe/H] = −0.38, at the upper metallicity limit of the bulk population) calculates an interpulse period of 7.49×10^4 years, but no mass-loss parameter is included. If the average carbon-rich lifetime of an AGB star in the Sgr dSph is between 1.07 and 2.26×10^5 years, during the carbon-rich phase a star will undergo 0.7 − 3.6 thermal pulses. In the Sgr dSph C-stars may only experience one or two thermal pulses before the associated mass loss terminates the AGB phase of their lives. This implies that the rate of mass loss greatly increases once a star becomes carbon rich. Lagadec and Zijlstra (2008) find that dust production in AGB stars is greatly enhanced once the C/O ratio exceeds unity, triggering the superwind.

The SHB models and the Pisa evolutionary tracks both predict the onset of thermal pulses to occur around the luminosities at which the first carbon stars appear on the H–R diagram. This implies that stars in the Sgr dSph become carbon rich very early on on the TP-AGB. Lagadec and Zijlstra (2008) also observed this phenomenon for AGB stars within the SMC. The location of these carbon stars around the tip of the RGB could also be due to the luminosity variations experienced during a thermal pulse. If these stars are currently burning helium they will exhibit luminosities roughly three times fainter than the stars undergoing hydrogen burning. Stars burn helium for approximately 10% of the thermal pulse cycle.

6

Comparison With Existing Data

The *AKARI* 9-μm magnitude and the *IRAS* 12-μm magnitude can be used to determine whether stars are dusty or not, as the ($K-$ [9]) and ($K-$ [12]) colours are indicators of the infrared (IR) excess displayed by dusty stars. Total mass-loss rates, $\dot{M}_{tot}$, of these stars can also be estimated using the ($K-$ [12]) colour. In this Chapter, the *AKARI* and *IRAS* catalogues are used to determine these values, before the results are compared with the conclusions of Lagadec et al. (2008, 2009b), who studied carbon-rich stars in the Sgr dSph in the IR.

6.1 Comparison With Infrared Observations

Several stars within our data set are included in the *AKARI* and *IRAS* catalogues. Any stars, in the Sgr dSph fields observed, within 5″ of the *AKARI* and *IRAS* co-ordinates are identified as matches to our targets. 12 stars have been observed by *AKARI*, while 6 stars have been observed by *IRAS*: 2 stars have been observed by both.

6.1.1 ($K-$ [9]) and ($K-$ [12]) Colours

The K magnitude, *AKARI* 9-μm flux and the *IRAS* 12-μm flux lie on the Rayleigh-Jeans tail of the stellar spectral energy distribution (SED). Therefore, if λ is plotted against $F\lambda^2$, where F is the flux from the system, a non-dusty star will produce a flat line[1]. However, dusty circumstellar envelopes of evolved stars absorb radiation at optical wavelengths before re-emitting it in the mid-IR, causing an increase in flux at mid-IR wavelengths such as 9μm and 12μm. Positive values of ($K-$ [9]) and ($K-$ [12]) indicate the presence of dust.

To work out the ($K-$ [9]) and ($K-$ [12]) colours, the flux in the K band must be calculated. The wavelength of the $2MASS$ K band is 2.2 μm and its zero point is at 666.7 Jy. To determine the flux in the K band, the following equation is used:

$$F_K = 10^{-\frac{K_{mag}}{2.5}} \times 666.7 Jy, \tag{6.1}$$

where K_{mag} is the observed K magnitude.

Subsequently, the following equations are used to calculate the ($K-$ [9]) and ($K-$ [12]) colours, respectively:

$$(K - [9]) = 2.5 \times \log\left(\frac{F_9}{F_K}\frac{\lambda_9^2}{\lambda_K^2}\right) \tag{6.2}$$

$$(K - [12]) = 2.5 \times \log\left(\frac{F_{12}}{F_K}\frac{\lambda_{12}^2}{\lambda_K^2}\right), \tag{6.3}$$

where F_9 is the observed *AKARI* 9-μm flux, $\lambda_K = 2.2$ μm, $\lambda_9 = 8.61$ μm, F_{12} is the observed *IRAS* 12-μm flux and $\lambda_{12} = 12$ μm.

Table 6.1 summarises all the stars, studied in this thesis, which have been observed by *AKARI* and *IRAS*. The stars in bold are those which are assumed to be carbon stars belonging to the Sgr dSph, while the rest are assumed to be Galactic foreground stars. This assumption is based on the radial velocity range calculated for stars from their K

[1]A flat line will be produced assuming that a naked photosphere has a power law of λ^{-2} between the K band and the 12 μm region. In actual fact a number of molecular features cause slightly non-zero colours.

and $(J - K)$ values, see Chapter 4.3. Figure 6.1 displays the stars detected by *AKARI* and *IRAS* on the CMD from Chapter 3. The $(K-[9])$ and $(K-[12])$ colours in Table 6.1, for the six assumed carbon-rich Sgr dSph stars, show clear IR excesses, with the highest $(K-[9])$ and $(K-[12])$ colours found for the most reddened stars.

The Galactic stars also have positive $(K-[12])$ colours[2], albeit at much lower values than for the carbon stars. These stars could be dusty foreground stars or their positive K values may be due to the CO feature at 2.3 μm, or the fact that they are cool stars. The CO feature at 2.3 μm may lower the K flux dramatically, hence an enhanced positive $(K-[12])$ colour will be recorded. Furthermore, if the stars are cool stars then their SED peaks will be shifted to longer wavelengths. Therefore, the K band may lie at the peak of the SED, or in the Wien's law section; thus producing a positive $(K-[12])$ colour.

The mass-loss rates in Table 6.1 are calculated using the relation between mass loss and $(K-[12])$ colour as determined by Whitelock et al. (2006). Unfortunately, only two of the assumed carbon stars have been observed with *IRAS*, therefore, total mass-loss rates can only be determined for these stars. The total mass-loss rates for the two dusty carbon stars are found to be $\sim 10^{-5}$ $M_\odot$ yr^{-1}.

6.2 Comparison With Previous Studies of the Sagittarius Dwarf Spheroidal

Studies of the Sgr dSph have been completed in the IR by Lagadec et al. (2008, 2009b). 29 stars within the Sgr dSph were observed by Lagadec et al. (2008, 2009b), for ten of which we have J and K band magnitudes. The spectra for four of these stars have been obtained and they have been classified as carbon rich, see §3.1.

The target selection for Lagadec et al. (2008) consisted of some spectroscopically confirmed C-stars, as determined by Whitelock et al. (1999), and a colour selection of

[2]No Galactic stars were detected by *AKARI*.

Table 6.1: Determining the ($K-$ [9]) and ($K-$ [12]) colours. The stars in bold are Sgr dSph carbon stars. Values labelled with an asterisk were derived from magnitudes taken from the *IRAS* reject catalogue and therefore should be treated with caution. The value of log($\dot{M}_{tot}$) was calculated using the relation between mass loss and ($K-$ [12]) colour determined by Whitelock et al. (2006).

Star	K_{flux} / Jy	*AKARI* 9-μm / Jy	*IRAS* 12-μm / Jy	($K-$ [9])	($K-$ [12])	log($\dot{M}_{tot}$)
1	**0.025**	**0.313**	**-**	**5.70**	**-**	**-**
2	**0.088**	**0.193**	**0.219**	**3.82**	**4.67**	**−5.30**
	0.088	**0.193**	**0.418 ***	**3.82**	**5.38 ***	**−5.09 ***
3	**0.160**	**0.145**	**-**	**2.86**	**-**	**-**
4	**0.035**	**0.214**	**0.171**	**4.92**	**5.40**	**−5.09**
5	1.99	-	0.681	-	2.52	−6.15
	1.99	-	0.550 *	-	2.29 *	−6.26 *
6	**0.347**	**0.157**	**-**	**2.10**	**-**	**-**
7	1.18	-	0.108 *	-	1.09 *	−6.93 *
8	4.83	-	0.722	-	1.62	−6.62
9	0.839	-	0.151 *	-	1.82 *	−6.51 *
10	5.93	-	0.350	-	0.61	−7.24
11	**0.083**	**0.171**	**-**	**3.75**	**-**	**-**
12	0.816	-	0.132 *	-	1.71 *	−6.57 *
13	1.56	-	0.278	-	1.81	−6.52
14	2.40	-	0.143 *	-	0.62 *	−7.24 *
15	4.36	-	0.359	-	0.97	−7.01
16	2.26	-	0.163	-	0.83	−7.10

the 2*MASS* catalogue, aimed to isolate redder carbon stars than those from Whitelock et al. (1999). Lagadec et al. (2009b) confirmed the carbon-rich abundances of eight of the stars observed by Lagadec et al. (2008), including two that are covered by our

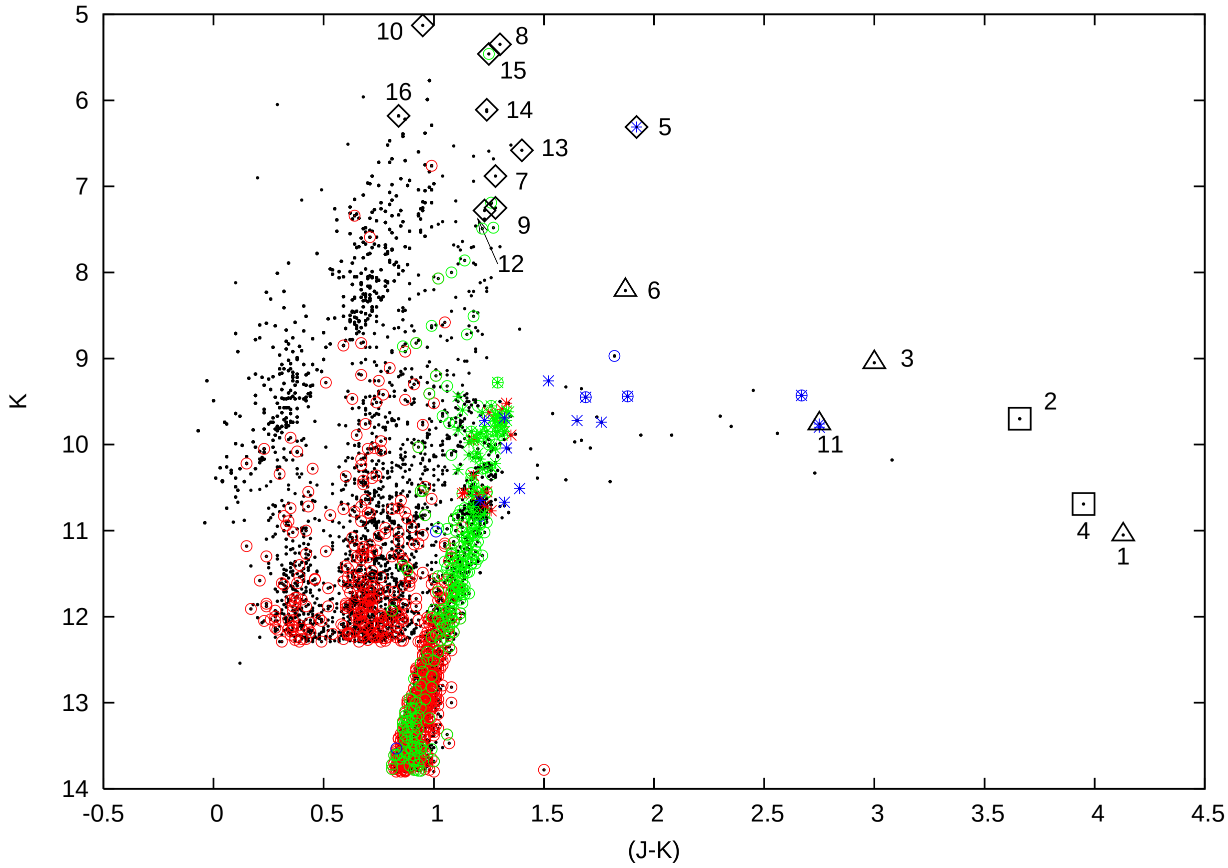

Figure 6.1: CMD indicating the stars that have been observed with *IRAS* (triangles), *AKARI* (diamonds) or both (squares). The rest of the symbols are as in Figure 3.4.

sample. Figure 6.2 identifies which stars have been studied by Lagadec et al. (2008, 2009b) and highlights those that are confirmed as carbon rich.

Lagadec et al. (2008) determined dust mass-loss rates of $10^{-10} - 10^{-8}$ $M_{\odot}$ yr^{-1} for the stars they observed in the Sgr dSph, and subsequently made estimations of the total mass-loss rates. Using the assumption of van Loon (2007) that the dust-to-gas mass ratio scales linearly with metallicity as:

$$\Psi = \Psi_{\odot} 10^{-[Fe/H]}, \tag{6.4}$$

where, Ψ is the dust-to-gas ratio and $\Psi_{\odot} = 0.005$, Lagadec et al. (2008) determine $\Psi \approx 1.4 \times 10^{-3}$ in the Sgr dSph. This leads to estimates of the total mass-loss rates of $\sim 6 \times$

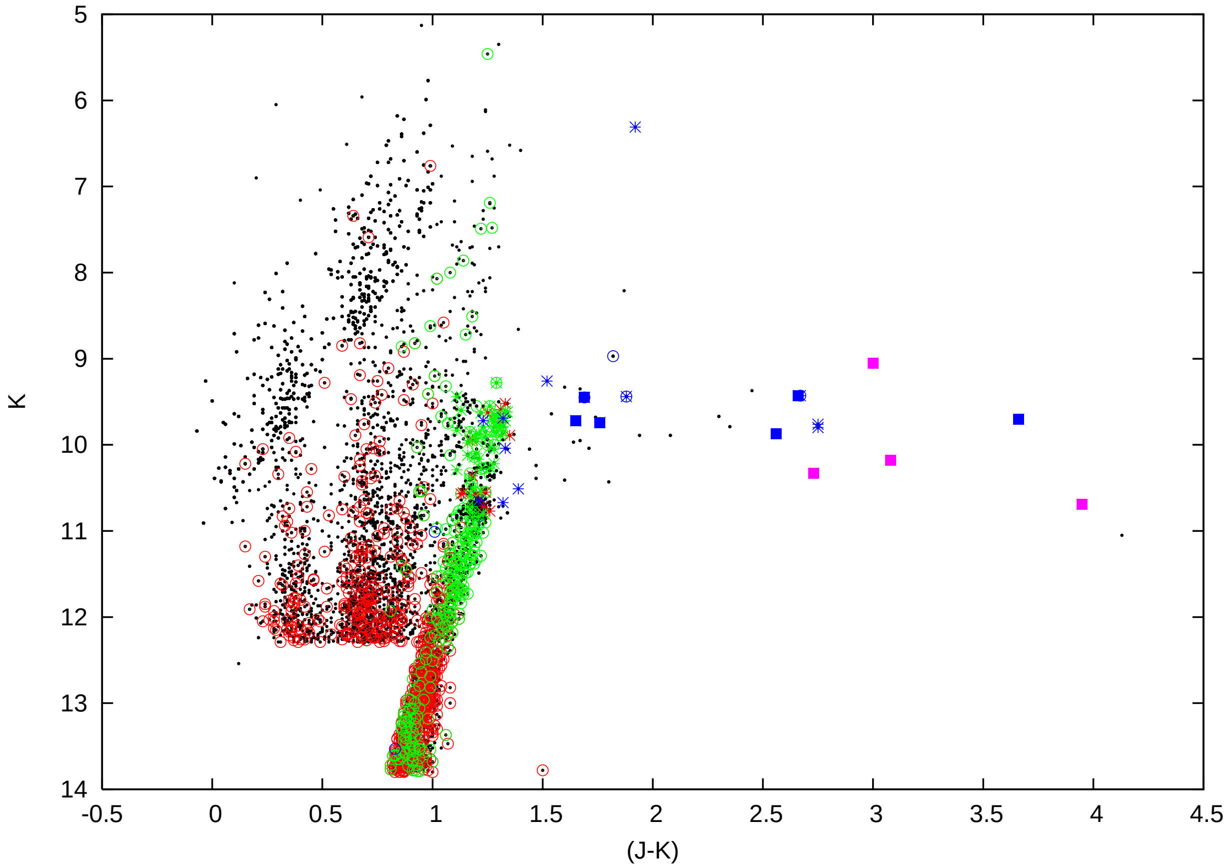

Figure 6.2: CMD, as in Figure 3.4, with the stars observed by Lagadec et al. (2008, 2009b) (filled squares) identified. Confirmed carbon stars; by either this thesis, Whitelock et al. (1999) or Lagadec et al. (2009b), are in blue. The expected, but unconfirmed, carbon stars are in pink.

10^{-7} to 2×10^{-5} $M_{\odot}$ yr^{-1} for the stars also studied in this thesis, with mass-loss rates increasing with redder colours and lower luminosities. These values are comparable with the total mass-loss rates of $\sim 10^{-5}$ $M_{\odot}$ yr^{-1} determined in §6.1.

Lagadec et al. (2009b) conclude that the carbon stars in the Sgr dSph belong to high-metallicity population of the galaxy. The isochrone modelling in §5.2 does not provide enough information to distinguish between the bulk metallicity population and the metal-rich population at 2.5 Gyr. Therefore, the comparison of our data with theoretical isochrones does not support nor oppose Lagadec et al. (2009b).

7

Discussion

7.1 The C/M Ratio

1094 objects have been observed in this thesis, of which 19 have been determined as C-type stars, 342 as M-type stars and 733 as K-type, or unknown, stars. After radial velocity determinations and colour cuts, as described in Chapter 5, the number of carbon stars in our observations is assumed to be 46. This assumption is supported by the findings of Chapter 6, from Lagadec et al. (2008, 2009b) that a further two of the reddened stars can be classified as carbon-rich. Furthermore, every observed star with $(J - K) > 1.35$ is found to be carbon rich.

To calculate an approximate C/M ratio for our observations the number of C- and M-type stars above the RGB tip, and which belong to the Sgr dSph, is found. The ratio of the number of stars above the RGB tip observed by the VLT, to the number of M-type stars which have been observed by the VLT and have accurate radial velocities classifying them as Sgr dSph members is 1/2. The total number of stars above the RGB tip is multiplied by this fraction to give an estimate for the number of M-type stars of 63.5. The number of C-stars above the RGB tip is 34. Therefore, an approximate C/M ratio for the Sgr dSph is 0.54.

C/M ratios have been determined for the LMC and the SMC, with values of 0.30

and 0.27, respectively (Cioni and Habing 2003). However, Cioni and Habing (2003) observe that the C/M ratio for M3, M5 and M7 stars, is much greater in the SMC than the LMC. This agrees with the theory that in low metallicity galaxies, carbon stars are more readily produced, see §1.3.1. Boyer et al. (2011) determine a C/M ratio for the SMC of 0.56. This C/M ratio includes extreme AGB stars, classified as carbon rich, and anomolous oxygen-rich AGB stars, as well as oxygen- and carbon-rich AGB stars.

The approximate C/M ratio determined for the Sgr dSph is, therefore, comparable with the values for the C/M ratio of the SMC found in the literature. As the Sgr dSph and the SMC have similar metallicities, $-0.7 \leq$ [Fe/H] ≤ -0.4 (Lagadec et al. 2008; Giuffrida et al. 2010) and [Fe/H]= -0.90 to -0.60 (Russell and Dopita 1992; Venn 1999; Rolleston et al. 1999, 2003; Lee et al. 2005), respectively, the observation of a comparable C/M ratio implies that the main population of the Sgr dSph must produce carbon stars, not just the small population at high metallicity as suggested by Lagadec et al. (2009b).

7.2 Carbon-Rich Lifetimes in the Sagittarius Dwarf Spheroidal

In §5.3 an average carbon-rich lifetime in the Sgr dSph of between 1.07 and 2.26×10^5 years was determined. This suggests that a carbon star may only experience 0.7 $-$ 3.6 thermal pulses before mass loss terminates its AGB life. This lifetime estimate is only an average value however, and has been calculated assuming that the carbon stars belong to the bulk population. If the carbon stars are only produced in the high metallicity population, as suggested by Lagadec et al. (2009b), the lifetime of each carbon star will increase proportionally. However, as discussed in §7.1, the calculated C/M ratio for this data suggests that this is not the case.

A luminosity spread in the carbon-rich AGB track is observed in the H–R diagram and the CMD, possibly due to the metallicity range of the bulk population and also the fact that stars within the Sgr dSph will display some range in ages. The stars in the Sgr dSph will also have undergone different mass-loss experiences throughout their lives, which also affects their evolution. The luminosity range of carbon stars is found to be $-3.5 \gtrsim K_{bol} \gtrsim -5.5$, with a range in $(J-K)$ due to the previously mentioned variations.

Lagadec et al. (2008) suggest that stars in lower metallicity galaxies will be carbon rich for a time before the onset of the superwind. The determination of an average C-rich lifetime of between 1.07 and 2.26×10^5 years does not support this prediction. The short C-star lifetime implies that once a star becomes carbon rich in the Sgr dSph, its mass-loss rate greatly increases, to shed its remaining atmospheric envelope quickly. This therefore suggests that at low metallicity, mass loss is more effective for carbon-rich stars than oxygen-rich stars. The mass loss of carbon-rich stars may be more effective due to the fact that the production of oxygen-rich dust is hampered at low metallicites, as it relies on metallicity dependent species, such as Si. Whereas, the majority of carbon-rich dust is only dependent on carbon, which the star produces itself. A study of the LMC and SMC, by Sloan et al. (2008), finds that the dust production rate of oxygen-rich dust is reduced at low metallicities, whereas the dust production rate in carbon stars is similar regardless of metallicity. The determination, in this thesis, of such a short average carbon-rich lifetime in the Sgr dSph supports the idea that carbon-rich dust production is not greatly affected in low metallicity environments.

As can be seen in Figure 3.4, a few carbon stars have been observed at luminosities around the tip of the RGB. This might be explained by the luminosity variations a star experiences during the thermal pulse cycle. Stars spend approximately 10% of the thermal pulse undergoing quiescent helium burning and during this phase their luminosities are roughly three times fainter than stars in the hydrogen burning phase. On the other hand, these carbon stars could indicate that, at the metallicity of the Sgr dSph, it does not take long for AGB stars to dredge up enough carbon for their C/O ratios to exceed unity. Lagadec and Zijlstra (2008) also observed this for AGB stars in the SMC; the RGB tip was found to coincide with the shift from oxygen-rich to carbon-rich, and the onset of thermal pulses. The SHB models and evolutionary tracks in §5.2 do not provide conclusive evidence for either of these theories.

However, the number of carbon stars observed to coincide with the onset of thermal pulses is four, roughly 10% of the total assumed number of carbon stars (46). If these stars were at three times their luminosity they would lie at the tip of the AGB, where other observed carbon stars are found. Also, the determined carbon-rich lifetime implies that stars in the Sgr dSph quickly lose their CSEs once they become carbon rich. If this occurs soon after the onset of thermal pulses, the TP-AGB will be a very brief phase, therefore limiting the number of observations of carbon-rich stars in the Sgr dSph. It is suggested that the most likely explanation for the carbon stars at the tip of the RGB, is that they are currently burning helium and are therefore at lower luminosities than stars which are experiencing the rest of the thermal pulse.

7.3 Modelling the Sagittarius Dwarf Spheroidal

7.3.1 The Carbon-Rich Population of the Sagittarius Dwarf Spheroidal

The models of Karakas and Lattanzio (2007), for the yields of PNe, indicate that at the metallicity and stellar mass of the Sgr dSph, carbon stars should not appear. Stars belonging to the bulk population metallicity (Z = 0.004 − 0.008) are not modelled to become carbon rich until 1.5 − 1.75 $M_\odot$. The young, 2.5 Gyr, stars of the metal-rich population will have initial masses of ∼1.5 $M_\odot$, but their metallicity is closer to the 1.75 $M_\odot$ limit from Karakas and Lattanzio (2007).

In this thesis, 19 carbon stars are detected in the Sgr dSph and strong evidence is presented for a further 27 stars to be carbon rich. Hence, our observations do not agree with these models.

7.3.2 Evolutionary Tracks of the Sagittarius Dwarf Spheroidal

From the comparison of our data with the isochrone models in §5.2, it is concluded that the distance modulus, $(m - M)_0 = 17.10$ mag (Monaco et al. 2004), reddening estimate, E($B-V$) = 0.14 (Layden and Sarajedini 2000) and extinction relation, A_K = 0.346E ($B-V$) (Rieke and Lebofsky 1985), assumed are accurate. Both the Dartmouth isochrone models (Dotter et al. 2007, 2008) and the Pisa evolutionary tracks (Castellani et al. 2003; Cariulo et al. 2004), model the RGB tip at the correct luminosity. The metallicity spread of the bulk population isochrones compares favourably to the width of the observed giant branch on the CMD, indicating that the published ranges in metallicity and [α/Fe] are accurate (e.g. Lagadec et al. 2008; Smecker-Hane and McWilliam 2002). However, when compared to the H–R diagram, the isochrones and evolutionary tracks towards the metal-rich limit of the bulk metallicity range fit the data most successfully. The metallicities of the data within this thesis should be identified to conclusively state whether the more metal-rich models are correct, or if the difference observed between the CMD and the H–R diagram is due to the bolometric corrections used.

7.4 The Metal-Poor Population of the Sagittarius Dwarf Spheroidal

As discussed in §4.1, several stars are observed in the region of the CMD dominated by K-type Galactic stars and yet display radial velocities classifying them as members of the Sgr dSph. In §5.2 it is suggested that five of these stars may belong to the metal-poor population. Metal-poor stars are at warmer temperatures and have much weaker molecular features, hence they were not distinguished as M- or C-type AGB stars during the spectral classification.

Another two stars are present at $T_{eff} \approx 4500$ K and $K_{bol} \approx -4.6$, whose origins are still unknown. If these stars are post-AGB stars they are expected to be present at the luminosities of the RGB tip, $K_{bol} \sim 4.00$. On the CMD these unknown stars have K_{obs} magnitudes comparable to the RGB tip, although when plotted on the H–R diagram they are located at luminosities higher than the RGB. It is suggested that these stars are most likely post-AGB stars, and the distance from the RGB tip has been exaggerated by the bolometric corrections used to plot the H–R diagram.

In §5.2 an estimation of the relative size of the metal-poor population is calculated. The metal-poor population is found to be approximately $\frac{1}{11}$ of the size of the bulk population. The size of the metal-rich population cannot be determined as the isochrone modelling was inconclusive. Metallicity determinations of these stars should be made from our spectra in order to determine the size of the metal-poor population, with more accuracy, and the size of the metal-rich population.

8

Conclusion

An extensive search for AGB stars in the Sgr dSph has not been completed before. Observations of the galaxy have been made to determine the metallicity and age populations of the Sgr dSph (e.g. Bellazzini et al. 1999a; Giuffrida et al. 2010), and smaller studies focusing on a few stars have been undertaken (e.g. Monaco et al. 2005; Lagadec et al. 2008, 2009b). This thesis adds to the findings of these previous papers.

In this thesis, 1095 objects have been observed: 1 galaxy, 19 carbon-rich stars, 342 oxygen-rich stars and 733 K-type or unknown stars. Due to time limitations the spectra were only classified as carbon- or oxygen-rich. Therefore, it is suggested that the exact spectral typing should be completed. Template spectra for M1, M3, M5 and M8 stars are available from http://www.sdss.org/dr5/algorithms/spectemplates/index.html. A more rigorous search for molecular features within the spectra should also be carried out, in order to determine whether dredge-up elements, such as *s*-process elements and Li, are present. This would enhance our understanding of how the dredge-up behaves at the lower metallicity of the Sgr dSph.

The radial velocities have been determined for the observations made at the VLT. Stars with approximate radial velocities greater than 95 km s^{-1} and with a radial velocity error of $< \pm$ 10 km s^{-1} are classified as belonging to the Sgr dSph. It is found that the Galactic foreground stars have a peak average radial velocity of -23 km s^{-1}, with a dispersion of 53 km s^{-1}, while stars within the Sgr dSph have a peak average radial velocity of 141 km s^{-1}, with a dispersion of 15 km s^{-1}. From the radial velocity determinations, and the theoretical isochrone modelling, a small population of K-type stars was observed at luminosities corresponding to the metal-poor population of the Sgr dSph. It was calculated that the bulk population is approximately eleven times greater than the metal-poor population.

The CMD of these observations was plotted and the RGB tip is determined to be located at $K = 10.6$. The onset of thermal pulses also occurs around this luminosity. A few carbon stars are located at the tip of the RGB and it is suggested that these stars are undergoing helium burning and therefore exhibit lower luminosities than stars in the hydrogen burning phase of a thermal pulse.

An average carbon-rich lifetime in the Sgr dSph of $1.07 - 2.26 \times 10^5$ years is been estimated from the evolutionary track models. This short lifetime implies that at the metallicities of the Sgr dSph, mass loss is much more effective for carbon-rich stars than oxygen-rich stars. This supports predictions that carbon-rich dust production is not restricted at lower metallicities (e.g. Zijlstra et al. 2006b; Sloan et al. 2008). The $(K-[9])$ and $(K-[12])$ colours have been determined for 19 stars, including six Sgr dSph carbon stars. The stars for which the $(K-[12])$ colour could be calculated, also have total mass-loss rates estimated for them. The most reddened, dusty carbon stars in the Sgr dSph have mass-loss rates of $\sim 10^{-5}$ $M_\odot$ yr^{-1}, which is comparable to the mass-loss rates determined by Lagadec et al. (2008).

A C/M ratio for the Sgr dSph is calculated to be 0.54, although it is acknowledged that, due to the fact that not all stars with K and $(J-K)$ values placing them on the Sgr dSph giant branch have been observed, this C/M value will have a significant error on it.

Appendix A

Tables of Results

A.1 VLT Data

Table A.1: A Complete Table of all the VLT Data

ID	RA	Dec	Spectral	2MASS		v_{rad}	σ_{rv}
			Type	K	$(J-K)$	(km s^{-1})	(km s^{-1})
SGR_00076	18 55 12.44	–30 23 39.03	K	09.92	00.35	-2.65	91.36
SGR_00138	18 55 18.97	–30 21 01.66	K	09.26	00.75	-11.68	0.63
SGR_00254	18 54 12.34	–30 24 09.96	K	12.28	00.78	-5.81	0.75
SGR_00262	18 54 08.78	–30 25 41.05	K	11.87	00.60	-0.63	1.21
SGR_00270	18 55 24.90	–30 17 22.26	K	10.24	00.67	7.42	0.48
SGR_00286	18 54 16.02	–30 21 21.63	M	10.54	00.94	31.34	1.79
SGR_00376	18 54 36.15	–30 42 12.12	K	12.09	00.72	-25.07	1.09
SGR_00390	18 53 54.27	–30 30 50.36	K	12.02	00.78	0.15	0.90
SGR_00397	18 54 41.68	–30 43 11.10	K	09.52	01.00	37.80	0.00
SGR_00406	18 55 56.09	–30 39 02.01	K	12.14	00.79	34.88	1.93
SGR_00423	18 53 50.14	–30 28 12.82	M	09.32	01.06	156.54	2.22

Continued on next page

Table A.1 – continued from previous page

ID	RA	Dec	Spectral Type	2MASS K	2MASS $(J-K)$	v_{rad} (km s^{-1})	σ_{rv} (km s^{-1})
SGR_00426	18 54 41.21	–30 43 50.34	K	12.25	00.77	35.77	1.33
SGR_00453	18 54 25.27	–30 14 36.47	K	12.14	00.70	41.15	0.61
SGR_00462	18 53 46.24	–30 28 30.72	K	12.29	00.66	-53.27	1.16
SGR_00478	18 53 44.73	–30 28 50.43	K	12.24	00.79	31.01	0.97
SGR_00481	18 54 34.18	–30 44 31.71	K	10.72	00.43	-36.03	1.26
SGR_00484	18 53 44.67	–30 26 39.98	K	11.31	00.65	43.07	1.01
SGR_00493	18 56 08.90	–30 38 42.67	K	12.07	00.44	50.90	0.88
SGR_00513	18 56 23.61	–30 32 44.87	K	10.08	00.38	-6.26	2.99
SGR_00514	18 56 25.11	–30 26 30.26	M	11.02	00.84	-99.97	0.62
SGR_00522	18 53 40.40	–30 28 00.92	K	10.46	00.68	24.70	0.87
SGR_00537	18 53 50.39	–30 37 53.15	K	12.02	00.48	48.82	0.75
SGR_00562	18 55 51.26	–30 13 13.03	K	11.97	00.76	-35.51	0.98
SGR_00571	18 53 36.30	–30 30 03.17	K	09.28	00.51	0.08	1.24
SGR_00575	18 54 43.66	–30 10 21.20	K	11.02	00.36	-1.84	0.72
SGR_00578	18 56 30.61	–30 31 03.62	K	11.03	00.78	-98.20	1.31
SGR_00595	18 56 26.49	–30 35 49.47	K	11.87	00.82	-8.17	1.37
SGR_00611	18 56 33.80	–30 28 48.35	K	11.30	00.81	-19.98	1.62
SGR_00612	18 54 28.02	–30 46 43.17	K	11.08	00.63	15.59	0.65
SGR_00620	18 55 59.24	–30 13 14.57	K	11.88	00.61	21.20	1.10
SGR_00629	18 56 33.84	–30 25 33.25	K	06.76	00.99	39.38	0.80
SGR_00639	18 55 39.59	–30 10 26.89	K	10.63	00.99	-2.66	0.78
SGR_00642	18 53 50.87	–30 41 07.36	K	11.33	00.86	-7.80	0.69
SGR_00645	18 55 28.44	–30 09 30.24	K	11.15	00.93	-63.83	0.84
SGR_00647	18 53 35.15	–30 34 59.74	K	11.61	00.31	21.36	1.00

Continued on next page

Table A.1 – continued from previous page

ID	RA	Dec	Spectral Type	2MASS K	2MASS $(J-K)$	v_{rad} (km s^{-1})	σ_{rv} (km s^{-1})
SGR_00679	18 54 23.32	–30 47 27.31	K	12.03	00.85	-40.92	0.47
SGR_00686	18 54 47.41	–30 08 14.98	K	11.40	00.39	-8.47	1.15
SGR_00688	18 54 55.85	–30 07 59.50	K	10.94	00.33	59.58	1.93
SGR_00698	18 53 35.72	–30 37 45.59	K	11.16	00.91	87.03	0.68
SGR_00707	18 56 35.00	–30 21 25.29	K	11.86	00.87	-52.72	1.60
SGR_00710	18 54 20.84	–30 47 43.74	K	12.07	00.76	42.84	1.56
SGR_00736	18 53 23.17	–30 27 52.18	K	12.00	00.76	28.64	0.59
SGR_00748	18 54 50.43	–30 50 16.04	K	11.57	00.46	-39.10	0.69
SGR_00768	18 54 26.97	–30 08 05.10	K	11.27	00.42	21.21	0.59
SGR_00785	18 56 42.39	–30 22 15.88	M	09.20	01.01	-24.07	1.62
SGR_00792	18 53 58.23	–30 46 20.08	K	09.30	00.91	55.23	0.56
SGR_00802	18 55 20.79	–30 06 22.44	M	07.19	01.26	78.43	151.10
SGR_00803	18 53 26.44	–30 19 53.09	K	11.88	00.69	53.82	1.22
SGR_00810	18 56 48.78	–30 28 02.98	K	10.80	00.71	-50.39	0.82
SGR_00828	18 54 43.96	–30 06 05.37	K	11.79	00.71	-22.41	1.24
SGR_00829	18 55 06.05	–30 05 42.71	K	11.30	00.24	-24.74	3.22
SGR_00858	18 56 50.67	–30 25 24.91	K	11.12	00.84	107.19	0.99
SGR_00877	18 53 50.52	–30 46 21.69	K	12.29	00.94	-91.09	0.75
SGR_00882	18 55 35.27	–30 06 06.46	K	11.05	00.95	48.37	0.78
SGR_00888	18 56 33.58	–30 42 20.48	K	12.24	00.68	1.47	1.21
SGR_00894	18 56 53.62	–30 26 59.28	M	10.03	00.93	-0.03	1.45
SGR_00904	18 53 12.61	–30 26 22.70	K	11.76	00.65	-60.86	1.29
SGR_00912	18 56 54.17	–30 25 59.50	M	09.75	01.07	5.11	2.73
SGR_00913	18 54 22.83	–30 51 08.94	K	12.29	00.93	9.68	1.74

Continued on next page

Table A.1 – continued from previous page

ID	RA	Dec	Spectral Type	2MASS K	$(J-K)$	v_{rad} (km s^{-1})	σ_{rv} (km s^{-1})
SGR_00918	18 54 13.09	–30 50 18.79	K	11.64	00.72	-40.39	0.90
SGR_00920	18 54 08.12	–30 49 45.50	K	12.05	00.28	-53.83	1.87
SGR_00930	18 53 23.40	–30 17 29.67	K	10.97	00.78	-43.06	1.20
SGR_00933	18 54 07.53	–30 49 54.14	K	12.05	00.81	34.70	1.27
SGR_00943	18 55 50.49	–30 06 24.25	K	11.97	00.67	-14.84	1.13
SGR_00956	18 53 38.52	–30 12 08.87	K	07.34	00.64	0.02	1.55
SGR_00985	18 53 07.28	–30 25 50.56	K	12.26	00.59	-18.03	1.50
SGR_01004	18 53 59.27	–30 50 06.50	K	12.18	00.72	140.41	1.11
SGR_01022	18 57 02.62	–30 28 09.11	K	10.75	00.59	-2.33	1.60
SGR_01056	18 55 12.22	–30 02 39.11	K	10.22	00.15	-19.77	5.36
SGR_01075	18 53 38.25	–30 47 45.74	K	11.63	00.32	28.38	1.65
SGR_01078	18 53 26.16	–30 12 35.01	K	12.14	00.40	-14.36	2.92
SGR_01086	18 53 51.55	–30 50 14.16	K	11.29	00.67	-96.25	0.84
SGR_01090	18 53 09.52	–30 38 54.21	K	11.98	00.84	-130.16	0.74
SGR_01102	18 55 42.75	–30 03 20.75	K	12.06	00.68	-38.16	0.89
SGR_01103	18 53 45.34	–30 49 35.77	K	11.73	00.68	-49.26	0.77
SGR_01124	18 53 31.75	–30 47 18.33	K	11.79	00.73	-11.66	2.84
SGR_01139	18 55 18.86	–30 01 42.51	K	12.20	00.68	19.32	1.54
SGR_01149	18 54 22.96	–30 54 40.53	K	10.79	00.87	-38.02	0.90
SGR_01158	18 53 54.90	–30 51 54.28	K	11.06	00.75	-20.52	0.42
SGR_01162	18 53 34.82	–30 48 33.15	K	12.00	00.72	-128.09	0.52
SGR_01187	18 52 54.19	–30 27 28.64	K	11.85	00.60	-103.49	2.88
SGR_01190	18 53 06.96	–30 40 58.25	K	11.85	00.64	-103.30	1.46
SGR_01208	18 52 53.69	–30 26 16.48	K	12.14	00.34	31.93	0.76

Continued on next page

Table A.1 – continued from previous page

ID	RA	Dec	Spectral Type	2MASS K	2MASS $(J-K)$	v_{rad} (km s^{-1})	σ_{rv} (km s^{-1})
SGR_01246	18 53 00.76	–30 17 53.85	K	11.23	00.74	59.25	1.28
SGR_01259	18 53 24.40	–30 09 28.96	K	10.17	00.67	36.10	1.03
SGR_01273	18 53 32.71	–30 50 01.68	K	12.00	00.28	18.17	2.56
SGR_01289	18 53 34.33	–30 50 39.20	K	10.89	00.67	11.84	0.88
SGR_01295	18 53 30.45	–30 49 57.07	K	10.05	00.70	0.98	1.10
SGR_01305	18 53 09.25	–30 12 54.04	K	11.79	00.72	27.53	1.27
SGR_01342	18 57 18.60	–30 34 06.27	K	11.95	00.66	-28.91	0.92
SGR_01360	18 53 24.20	–30 49 37.18	K	08.82	00.67	-7.91	0.39
SGR_01368	18 52 47.71	–30 22 12.53	K	10.78	00.64	35.25	1.08
SGR_01382	18 53 35.16	–30 52 03.82	K	12.05	00.49	9.08	1.62
SGR_01385	18 54 12.81	–30 56 46.39	M	11.46	00.88	55.40	135.78
SGR_01387	18 53 36.49	–30 52 21.85	K	11.89	00.68	8.83	0.69
SGR_01405	18 53 07.28	–30 46 00.33	K	11.91	00.17	16.18	2.39
SGR_01410	18 52 54.48	–30 16 19.62	K	12.04	00.66	-46.63	1.80
SGR_01418	18 53 41.72	–30 53 40.16	K	11.19	00.68	43.70	1.17
SGR_01425	18 53 02.61	–30 44 51.08	M	11.93	00.81	1.27	2.53
SGR_01491	18 52 55.59	–30 14 10.59	K	08.92	00.87	16.99	1.36
SGR_01533	18 52 57.30	–30 12 26.49	K	12.29	00.49	-18.03	0.94
SGR_01554	18 52 35.40	–30 26 40.12	K	11.98	00.64	37.67	0.85
SGR_01578	18 52 42.25	–30 18 20.98	K	12.13	00.28	-46.34	2.42
SGR_01640	18 52 33.11	–30 24 28.63	K	12.12	00.83	40.31	0.65
SGR_01709	18 52 47.75	–30 12 55.68	K	12.24	00.74	50.49	1.85
SGR_01831	18 52 27.63	–30 22 19.93	M	10.97	01.02	128.09	3.62
SGR_01890	18 57 31.09	–30 42 41.41	M	07.86	01.14	22.71	3.23

Continued on next page

Table A.1 – continued from previous page

ID	RA	Dec	Spectral Type	2MASS K	$(J-K)$	v_{rad} (km s^{-1})	σ_{rv} (km s^{-1})
SGR_01998	18 57 38.75	–30 40 50.07	K	09.11	00.80	-53.42	0.77
SGR_02105	18 57 37.07	–30 44 10.81	K	12.11	00.36	-64.04	2.29
SGR_02136	18 52 37.62	–30 09 33.12	K	12.12	00.69	11.04	3.70
SGR_02140	18 57 40.90	–30 43 03.41	K	09.51	00.74	-49.28	0.92
SGR_02195	18 52 47.57	–30 05 39.67	K	11.67	00.52	-83.78	8.36
SGR_02216	18 52 53.29	–30 03 54.74	K	11.67	00.73	110.74	160.10
SGR_02256	18 52 34.14	–30 08 50.72	K	12.03	00.26	19.00	7.04
SGR_02392	18 57 35.25	–30 50 04.09	K	10.72	00.67	26.69	0.77
SGR_02397	18 57 54.54	–30 41 44.98	K	12.04	00.93	117.75	0.50
SGR_02414	18 52 51.42	–30 01 44.03	K	11.85	00.24	-26.89	3.00
SGR_02443	18 57 52.34	–30 44 07.22	K	08.58	01.05	48.68	0.60
SGR_02446	18 57 47.64	–30 46 20.65	K	10.39	00.72	-21.83	1.57
SGR_02537	18 52 45.11	–30 01 37.58	K	09.76	00.69	-4.10	0.99
SGR_02555	18 52 54.41	–29 59 25.25	K	11.56	00.46	28.17	0.75
SGR_02630	18 58 12.52	–30 33 11.14	K	12.04	00.79	87.73	1.11
SGR_02631	18 52 09.16	–30 12 16.30	K	10.36	00.74	104.99	4.16
SGR_02638	18 52 28.05	–30 05 00.18	K	11.96	00.67	30.81	1.49
SGR_02737	18 58 12.79	–30 38 07.76	K	11.80	00.71	-10.68	0.78
SGR_02752	18 52 09.58	–30 09 52.91	M	09.41	00.98	-57.37	2.56
SGR_02795	18 52 07.53	–30 10 02.53	K	10.05	00.23	-42.97	6.85
SGR_02799	18 52 14.88	–30 07 06.37	M	10.12	01.08	-0.88	2.70
SGR_02810	18 58 17.29	–30 35 54.79	M	08.00	01.08	44.40	2.08
SGR_02857	18 58 03.47	–30 46 38.51	K	11.87	00.72	57.32	1.92
SGR_02869	18 57 47.42	–30 52 51.53	K	12.21	00.35	-10.37	3.34

Continued on next page

Table A.1 – continued from previous page

ID	RA	Dec	Spectral Type	2MASS K	$(J-K)$	v_{rad} (km s^{-1})	σ_{rv} (km s^{-1})
SGR_02872	18 58 11.27	–30 42 37.34	K	10.55	00.43	-7.73	1.68
SGR_02907	18 58 03.70	–30 47 26.23	K	11.24	00.51	-65.16	0.92
SGR_02912	18 52 35.68	–29 59 40.74	K	10.65	00.85	-45.32	0.41
SGR_02971	18 58 10.60	–30 45 05.14	K	10.83	00.32	7.16	1.75
SGR_02983	18 52 05.14	–30 08 12.69	K	08.85	00.59	-4.35	0.84
SGR_03013	18 52 18.89	–30 03 03.55	K	11.72	00.62	25.40	0.53
SGR_03034	18 52 20.43	–30 02 25.14	K	10.64	00.69	-51.69	0.97
SGR_03069	18 58 26.73	–30 34 28.39	K	09.77	00.95	-131.50	1.01
SGR_03080	18 57 59.67	–30 51 30.32	M	08.82	00.92	-98.69	1.45
SGR_03123	18 52 11.13	–30 04 09.91	K	12.21	00.72	16.51	2.85
SGR_03165	18 52 55.90	–29 53 14.53	K	11.88	00.70	27.34	4.25
SGR_03209	18 57 57.46	–30 54 02.86	K	10.74	00.84	-3.64	0.58
SGR_03219	18 52 45.98	–29 54 30.09	K	11.27	00.84	29.05	1.35
SGR_03260	18 58 34.14	–30 32 09.09	K	07.48	01.27	80.33	2.78
SGR_03284	18 52 00.32	–30 05 42.95	K	11.96	00.83	-37.50	2.79
SGR_03343	18 58 35.79	–30 34 27.98	M	08.62	00.99	-44.29	1.32
SGR_03363	18 58 18.29	–30 48 19.28	M	07.49	01.22	-74.44	7.82
SGR_03367	18 51 49.88	–30 08 38.67	K	11.84	00.82	-7.81	5.09
SGR_03381	18 58 37.37	–30 34 23.84	K	11.56	01.00	123.30	0.28
SGR_03458	18 58 36.25	–30 38 55.79	K	11.46	00.67	8.45	1.09
SGR_03467	18 58 17.19	–30 50 29.49	K	10.89	00.34	64.58	3.35
SGR_03479	18 52 37.60	–29 53 38.45	K	12.18	00.44	-88.29	2.19
SGR_03528	18 58 15.47	–30 52 06.13	K	11.22	00.68	-6.81	1.15
SGR_03543	18 52 04.25	–30 00 54.96	K	12.27	00.37	-39.23	6.30

Continued on next page

Table A.1 – continued from previous page

ID	RA	Dec	Spectral Type	2MASS K	$(J-K)$	v_{rad} (km s^{-1})	σ_{rv} (km s^{-1})
SGR_03558	18 58 33.17	–30 44 12.82	K	11.79	00.92	135.84	0.73
SGR_03620	18 51 46.22	–30 06 12.61	K	12.05	00.86	55.38	3.09
SGR_03630	18 52 41.59	–29 51 30.31	K	11.41	00.60	-25.38	1.11
SGR_03661	18 58 15.19	–30 53 51.88	K	10.96	00.90	25.98	0.92
SGR_03670	18 58 45.53	–30 35 57.21	K	11.54	00.63	-16.36	0.53
SGR_03687	18 52 23.12	–29 54 40.18	K	11.70	00.79	-37.31	1.00
SGR_03695	18 58 29.12	–30 48 39.44	K	11.81	00.71	13.92	0.97
SGR_03734	18 58 48.91	–30 32 50.93	K	09.19	00.67	31.33	0.79
SGR_03761	18 58 27.23	–30 50 22.52	K	12.29	00.39	69.89	2.53
SGR_03858	18 51 42.44	–30 04 35.16	K	12.19	00.62	-45.74	3.45
SGR_03883	18 51 35.25	–30 07 11.93	K	11.69	00.75	37.88	118.35
SGR_03901	18 52 27.69	–29 51 49.73	K	11.88	00.24	-5.40	4.78
SGR_03939	18 58 47.61	–30 42 19.67	K	11.95	00.67	11.90	1.25
SGR_03951	18 58 45.12	–30 44 18.67	K	11.54	00.39	-11.33	1.32
SGR_03998	18 51 45.36	–30 01 53.05	M	10.54	00.95	-22.67	3.11
SGR_04055	18 58 47.80	–30 44 34.75	K	11.90	00.67	182.74	1.36
SGR_04132	18 58 54.19	–30 41 28.82	K	09.48	00.87	-176.19	0.74
SGR_04154	18 52 06.48	–29 54 16.42	K	09.96	00.76	-198.38	0.74
SGR_04243	18 52 17.35	–29 51 08.39	K	10.86	00.88	-247.82	1.94
SGR_04262	18 52 00.24	–29 54 51.97	K	12.28	00.85	41.17	2.88
SGR_04347	18 52 23.16	–29 48 57.71	K	11.82	00.37	-4.27	126.12
SGR_04381	18 52 12.83	–29 50 40.03	K	12.20	00.84	80.91	4.60
SGR_04433	18 51 59.86	–29 53 08.00	M	10.82	00.96	-31.30	2.44
SGR_04461	18 51 40.77	–29 57 58.21	K	10.04	00.73	-10.32	0.92

Continued on next page

Table A.1 – continued from previous page

ID	RA	Dec	Spectral Type	2MASS K	2MASS $(J-K)$	v_{rad} (km s^{-1})	σ_{rv} (km s^{-1})
SGR_04472	18 52 19.98	–29 48 29.66	K	12.17	00.76	-45.06	106.02
SGR_04488	18 51 23.42	–30 03 50.69	K	12.28	00.86	-19.25	109.46
SGR_04535	18 51 48.60	–29 55 07.14	K	11.43	00.88	-148.46	2.58
SGR_04544	18 51 57.22	–29 52 51.29	K	12.15	00.43	-72.84	1.99
SGR_04669	18 59 09.16	–30 42 22.92	K	11.46	00.67	25.94	1.07
SGR_05026	18 51 57.69	–29 48 42.78	K	11.18	00.15	24.73	3.59
SGR_05130	18 51 51.16	–29 49 16.31	K	11.49	00.95	-14.72	5.52
SGR_05167	18 57 52.56	–31 13 12.47	K	12.04	00.36	17.70	2.98
SGR_05199	18 57 44.37	–31 14 47.39	K	12.23	00.73	36.50	2.18
SGR_05426	18 58 02.50	–31 13 12.43	K	11.85	00.37	7.09	2.44
SGR_05531	18 58 15.88	–31 11 25.32	K	11.71	00.71	-39.95	1.68
SGR_05586	18 59 00.38	–30 59 59.11	K	10.42	00.68	134.11	1.63
SGR_05613	18 59 09.01	–30 57 02.30	K	11.75	00.75	-22.16	1.43
SGR_05682	18 57 44.98	–31 18 02.06	K	12.15	00.36	13.05	0.98
SGR_05733	18 57 42.41	–31 18 41.08	K	11.74	00.68	-15.34	1.25
SGR_05767	18 57 37.97	–31 19 28.19	K	12.27	00.70	8.89	1.81
SGR_05789	18 58 12.94	–31 13 51.28	M	08.07	01.02	-15.00	1.27
SGR_05857	18 59 21.30	–30 54 13.72	K	11.66	00.61	50.96	0.55
SGR_05866	18 58 04.40	–31 15 53.50	K	11.64	00.68	-71.70	1.66
SGR_05874	18 57 51.45	–31 18 05.90	K	11.61	00.38	-23.15	2.01
SGR_05880	18 57 32.43	–31 20 51.94	K	11.34	00.67	43.13	1.64
SGR_05935	18 59 24.67	–30 53 46.84	K	10.34	00.30	-20.96	1.58
SGR_06060	18 59 14.49	–30 59 38.15	K	11.17	00.64	-57.93	1.11
SGR_06068	18 58 23.84	–31 13 45.11	K	10.07	00.76	-5.84	0.67

Continued on next page

Table A.1 – continued from previous page

ID	RA	Dec	Spectral Type	2MASS K	2MASS $(J-K)$	v_{rad} (km s^{-1})	σ_{rv} (km s^{-1})
SGR_06097	18 57 56.68	–31 18 52.96	K	11.54	00.72	9.33	1.89
SGR_06265	18 58 02.78	–31 18 51.93	K	11.82	00.70	-69.85	0.90
SGR_06348	18 59 36.77	–30 53 20.35	K	12.11	00.59	-134.01	0.51
SGR_06373	18 58 32.74	–31 14 07.82	K	11.71	00.82	3.73	1.07
SGR_06383	18 58 04.98	–31 19 24.86	K	12.21	00.61	-49.59	0.87
SGR_06501	18 58 39.54	–31 13 37.79	K	11.93	00.36	78.16	0.95
SGR_06570	18 57 47.20	–31 23 20.44	K	12.10	00.39	-81.27	0.94
SGR_06612	18 57 52.50	–31 22 52.63	K	11.52	00.89	80.57	0.26
SGR_06724	18 59 49.21	–30 52 02.01	K	11.93	00.28	14.53	3.01
SGR_06753	18 58 35.57	–31 16 23.13	K	11.44	00.61	-26.23	1.14
SGR_06850	18 58 39.67	–31 16 07.66	K	11.88	00.52	24.71	1.32
SGR_06888	18 58 44.81	–31 15 16.91	K	12.20	00.61	24.58	1.86
SGR_06917	18 59 54.44	–30 51 39.31	K	12.19	00.61	9.74	0.87
SGR_06920	18 59 47.63	–30 55 22.18	K	10.37	00.60	46.62	0.88
SGR_07004	18 59 11.37	–31 09 30.18	K	11.27	00.68	-23.60	0.86
SGR_07052	18 58 42.31	–31 16 52.49	K	11.78	00.37	-69.66	1.58
SGR_07086	18 57 51.75	–31 25 43.55	K	09.47	00.63	22.73	1.04
SGR_07104	18 58 01.90	–31 24 24.38	K	12.29	00.31	3.14	1.41
SGR_07178	18 58 23.68	–31 21 23.12	K	12.24	00.73	-62.91	0.58
SGR_07250	18 58 20.89	–31 22 21.25	K	11.60	00.66	-64.75	0.92
SGR_07254	18 58 49.23	–31 16 58.25	K	11.60	00.89	40.07	0.82
SGR_07278	18 59 02.25	–31 14 11.38	K	12.27	00.70	-29.22	2.01
SGR_07380	18 58 52.45	–31 17 10.39	K	11.88	00.92	97.52	1.25
SGR_07545	18 58 04.14	–31 26 51.97	K	12.15	00.29	10.16	5.08

Continued on next page

Table A.1 – continued from previous page

ID	RA	Dec	Spectral Type	2MASS K	$(J-K)$	v_{rad} (km s^{-1})	σ_{rv} (km s^{-1})
SGR_07602	19 00 04.37	–30 55 47.30	K	10.28	00.45	-20.31	0.95
SGR_07719	18 59 34.86	–31 08 44.32	K	11.85	00.86	61.83	1.30
SGR_07720	18 59 57.02	–31 00 38.55	K	12.24	00.37	-10.17	4.04
SGR_07747	19 00 04.35	–30 57 37.00	K	12.26	00.42	-26.70	1.60
SGR_07750	19 00 14.93	–30 51 46.90	K	09.42	00.77	17.18	0.91
SGR_07830	18 58 16.16	–31 26 44.44	K	12.02	00.86	177.38	1.42
SGR_07843	18 58 09.67	–31 27 46.09	M	08.86	00.86	-55.62	4.05
SGR_07860	18 58 58.12	–31 19 17.57	K	10.79	00.70	-17.52	1.08
SGR_07890	18 59 10.28	–31 16 42.89	K	11.54	00.61	-25.54	1.84
SGR_07914	18 58 12.90	–31 27 39.85	K	12.05	00.77	67.41	0.89
SGR_07926	18 57 57.21	–31 29 53.10	K	11.87	00.70	-184.98	1.93
SGR_07928	18 59 59.82	–31 01 28.48	K	07.59	00.71	-37.49	0.68
SGR_07966	18 59 31.50	–31 11 39.17	K	11.31	00.70	-25.34	0.84
SGR_08050	18 59 49.53	–31 06 36.88	K	11.90	00.60	-200.00	1.18
SGR_08188	18 58 59.37	–31 20 58.59	K	11.81	00.35	-86.35	4.19
SGR_08197	18 57 50.01	–31 32 08.71	M	05.46	01.25	63.48	9.72
SGR_08215	18 57 55.69	–31 31 29.42	K	12.17	00.75	177.10	1.71
SGR_08248	19 00 12.08	–30 59 03.55	K	12.23	00.64	-5.21	1.12
SGR_08340	19 00 23.47	–30 54 13.29	K	12.00	00.80	-50.85	1.62
SGR_08407	18 58 00.86	–31 31 48.55	K	12.17	00.35	-33.49	1.27
SGR_08438	18 58 19.94	–31 29 18.45	K	12.12	00.36	-20.86	1.99
SGR_08517	18 58 24.67	–31 28 57.62	K	11.78	00.38	-36.46	3.19
SGR_08555	18 59 56.40	–31 08 08.81	K	11.35	00.86	8.87	2.77
SGR_08590	18 59 40.48	–31 13 26.08	K	12.09	00.58	-81.67	1.78

Continued on next page

Table A.1 – continued from previous page

ID	RA	Dec	Spectral Type	2MASS K	$(J-K)$	v_{rad} (km s^{-1})	σ_{rv} (km s^{-1})
SGR_08592	18 58 47.15	–31 25 36.81	K	11.17	00.71	-63.34	0.48
SGR_08594	18 59 58.61	–31 07 42.04	M	11.41	00.86	75.16	130.89
SGR_08713	18 58 50.11	–31 25 43.10	K	09.89	00.65	23.06	0.46
SGR_08780	18 49 20.31	–30 14 46.39	K	12.23	00.68	-46.61	3.45
SGR_09014	18 49 17.92	–30 12 31.71	K	12.25	00.78	-104.17	6.15
SGR_09099	18 58 51.12	–31 27 49.45	K	12.04	00.34	-12.88	1.35
SGR_09251	18 59 59.18	–31 12 43.36	K	12.00	00.71	-69.17	1.85
SGR_09261	19 00 31.72	–31 00 17.70	K	12.16	00.64	30.30	0.61
SGR_09301	18 58 32.95	–31 31 47.32	K	12.21	00.61	-39.31	0.71
SGR_09352	18 58 54.98	–31 28 30.80	C	11.01	01.01	139.81	1.79
SGR_09374	19 00 35.20	–30 59 53.77	K	12.26	00.40	47.76	1.66
SGR_09380	19 00 30.32	–31 02 17.37	K	11.58	00.21	-22.14	5.07
SGR_09444	18 58 37.83	–31 31 53.50	K	11.59	00.59	-26.74	5.30
SGR_09670	18 49 04.71	–30 12 31.87	K	11.47	00.72	-100.15	152.05
SGR_09775	18 49 02.64	–30 12 50.73	K	11.25	00.72	-61.73	1.15
SGR_09786	18 59 19.09	–31 26 14.98	K	10.74	00.35	-43.83	1.17
SGR_09957	18 59 15.67	–31 27 57.12	M	08.51	01.18	184.25	126.55
SGR_10058	18 49 04.54	–30 06 05.41	K	10.49	00.96	-82.50	1.58
SGR_10177	18 48 59.82	–30 07 54.91	K	11.89	00.72	-4.95	1.17
SGR_10280	18 48 50.28	–30 15 27.43	K	11.55	00.66	-55.12	0.81
SGR_10352	18 48 45.65	–30 20 23.87	K	12.29	00.76	17.89	2.76
SGR_10377	18 48 44.77	–30 21 40.26	M	09.74	01.10	3.00	2.21
SGR_10759	18 48 38.63	–30 20 18.40	K	12.09	00.75	-56.22	1.76
SGR_10783	18 48 39.96	–30 17 15.26	K	12.21	00.81	-44.32	1.50

Continued on next page

Table A.1 – continued from previous page

ID	RA	Dec	Spectral Type	2MASS K	$(J-K)$	v_{rad} (km s^{-1})	σ_{rv} (km s^{-1})
SGR_10786	18 48 50.56	–30 06 25.48	K	10.75	00.81	-107.92	1.24
SGR_10821	18 48 38.56	–30 18 19.25	K	11.00	00.42	-14.12	1.17
SGR_11010	18 48 44.60	–30 07 46.21	K	11.88	00.36	13.51	1.19
SGR_11155	18 48 31.20	–30 21 06.51	K	10.82	00.53	42.02	1.48
SGR_11159	18 48 38.46	–30 11 03.34	K	11.62	00.69	68.16	0.99
SGR_11285	18 48 27.57	–30 23 50.32	K	11.88	00.42	39.18	101.17
SGR_11507	18 48 24.60	–30 22 25.00	K	11.98	00.85	81.67	3.52
SGR_11530	18 48 36.55	–30 07 03.61	K	11.76	00.67	-193.93	1.49
SGR_11931	18 48 18.34	–30 19 14.05	M	08.72	01.15	22.99	2.23
SGR_12272	18 48 24.84	–30 05 45.37	K	11.64	00.89	70.47	1.04
SGR_12329	18 48 12.48	–30 17 51.29	K	11.87	00.70	-11.47	1.96
SGR_12574	18 48 09.33	–30 16 22.87	K	12.05	00.23	-21.75	1.81
SGR_12592	18 48 16.99	–30 07 40.80	K	11.62	00.99	156.72	2.68
SGR_12893	18 48 12.82	–30 06 31.82	K	11.55	00.90	71.22	1.67
SGR_12923	18 48 11.07	–30 07 30.08	K	11.80	00.40	-57.65	1.11
SGR_13211	18 47 57.14	–30 18 12.97	K	12.18	00.67	-72.15	4.39
SGR_13251	18 48 05.59	–30 07 29.51	K	11.64	00.86	-32.20	2.81
SGR_13348	18 48 04.12	–30 07 12.48	K	11.99	00.76	-6.52	4.61
SGR_13403	18 47 58.90	–30 11 26.74	K	12.07	00.84	-16.16	3.45
SGR_13472	18 47 51.74	–30 20 10.14	M	09.67	01.04	-15.21	7.13
SGR_13627	18 48 06.27	–30 01 57.23	K	12.06	00.67	-31.31	129.71
SGR_13717	18 47 56.18	–30 09 00.66	K	12.24	00.83	19.60	124.45
SGR_13718	18 47 48.64	–30 18 42.29	K	11.98	00.66	0.46	101.86
SGR_13953	18 47 53.76	–30 07 09.58	K	12.03	00.65	-19.07	98.81

Continued on next page

Table A.1 – continued from previous page

ID	RA	Dec	Spectral Type	2MASS K	2MASS $(J-K)$	v_{rad} (km s^{-1})	σ_{rv} (km s^{-1})
SGR_14395	18 47 48.05	–30 05 18.86	K	12.20	00.54	41.92	113.68
SGR_14410	18 47 44.78	–30 08 02.48	K	11.54	00.76	50.31	4.12
SGR_14557	18 47 39.90	–30 10 49.44	K	12.23	00.73	80.33	114.20
SGR_P2583	18 55 15.66	–30 23 58.55	K	13.20	00.97	147.85	2.06
SGR_P2584	18 55 01.53	–30 23 07.29	M	11.50	01.13	129.15	2.80
SGR_P2599	18 55 02.14	–30 21 56.35	K	13.31	00.93	149.33	2.98
SGR_P2601	18 55 27.06	–30 24 03.20	M	11.55	01.09	135.86	2.41
SGR_P2604	18 55 30.38	–30 32 45.47	K	13.79	00.87	133.51	2.86
SGR_P2610	18 55 32.70	–30 32 58.96	M	11.44	01.08	132.95	0.89
SGR_P2614	18 55 12.86	–30 20 59.54	K	13.38	00.90	133.58	1.37
SGR_P2618	18 55 31.65	–30 23 22.87	M	12.02	01.12	147.35	1.49
SGR_P2619	18 54 52.61	–30 20 55.55	C	09.44	01.88	147.94	2.16
SGR_P2622	18 55 09.69	–30 20 35.93	K	13.27	00.96	127.18	1.17
SGR_P2623	18 55 41.69	–30 28 30.99	M	11.12	01.15	131.79	2.85
SGR_P2624	18 55 29.42	–30 34 50.76	M	10.62	01.21	122.20	7.11
SGR_P2632	18 55 36.30	–30 33 38.96	M	10.82	01.11	52.93	2.94
SGR_P2635	18 55 42.15	–30 31 19.68	K	13.38	00.91	142.24	0.89
SGR_P2637	18 55 31.67	–30 35 03.12	M	11.69	01.09	137.29	1.31
SGR_P2641	18 55 10.93	–30 19 49.33	K	12.19	01.01	140.72	1.00
SGR_P2645	18 54 57.59	–30 19 38.83	M	11.19	01.12	134.15	2.18
SGR_P2648	18 54 40.75	–30 36 32.89	M	11.08	01.15	137.51	1.07
SGR_P2650	18 55 44.48	–30 26 09.58	K	13.72	00.83	127.01	0.52
SGR_P2651	18 54 38.12	–30 36 11.68	M	12.06	01.09	134.62	1.77
SGR_P2652	18 54 54.70	–30 19 39.46	K	13.55	00.91	149.32	3.09

Continued on next page

Table A.1 – continued from previous page

ID	RA	Dec	Spectral Type	2MASS K	$(J-K)$	v_{rad} (km s^{-1})	σ_{rv} (km s^{-1})
SGR_P2654	18 55 43.80	–30 32 00.55	M	13.17	00.90	197.65	4.09
SGR_P2657	18 55 30.36	–30 21 25.00	M	12.54	00.94	-18.19	5.26
SGR_P2658	18 54 41.64	–30 20 36.09	M	10.14	01.19	143.25	138.19
SGR_P2661	18 55 24.82	–30 20 22.26	K	13.32	00.86	119.61	2.94
SGR_P2662	18 54 27.77	–30 34 33.81	M	10.76	01.19	117.90	2.71
SGR_P2665	18 55 48.02	–30 27 17.64	K	13.66	00.89	151.53	1.64
SGR_P2667	18 54 45.41	–30 19 43.96	K	12.61	00.94	138.05	1.23
SGR_P2669	18 55 44.42	–30 32 58.77	M	13.68	00.91	79.29	153.53
SGR_P2670	18 54 31.93	–30 36 03.17	K	13.05	00.96	144.44	2.31
SGR_P2672	18 55 22.99	–30 19 36.63	M	13.57	00.96	-34.10	4.79
SGR_P2673	18 54 22.92	–30 33 45.34	M	10.72	01.20	130.46	2.88
SGR_P2674	18 55 41.20	–30 22 46.15	K	12.77	00.96	131.12	1.10
SGR_P2676	18 54 47.25	–30 18 52.92	K	13.11	00.96	144.78	1.15
SGR_P2677	18 55 31.67	–30 20 15.68	M	10.91	01.21	135.90	2.22
SGR_P2678	18 54 56.82	–30 18 19.07	K	12.38	00.97	161.71	1.64
SGR_P2684	18 54 32.05	–30 37 07.70	K	13.00	01.08	144.64	1.29
SGR_P2687	18 55 53.61	–30 28 58.03	K	10.96	01.13	115.48	1.56
SGR_P2690	18 54 38.57	–30 19 02.47	M	11.91	01.05	132.98	2.36
SGR_P2691	18 54 46.66	–30 18 11.42	M	12.01	01.02	135.59	1.98
SGR_P2693	18 54 15.62	–30 24 12.76	K	12.67	01.01	139.12	0.68
SGR_P2694	18 54 38.93	–30 18 43.83	K	13.72	00.87	156.02	3.49
SGR_P2699	18 55 53.87	–30 25 23.15	K	12.22	00.97	163.99	2.44
SGR_P2700	18 55 55.45	–30 30 41.01	K	13.43	00.96	140.81	3.66
SGR_P2702	18 55 46.72	–30 35 24.84	K	11.77	01.08	149.30	0.58

Continued on next page

Table A.1 – continued from previous page

ID	RA	Dec	Spectral Type	2MASS K	$(J-K)$	v_{rad} (km s^{-1})	σ_{rv} (km s^{-1})
SGR_P2703	18 54 17.29	–30 34 34.39	M	11.05	01.19	153.38	2.77
SGR_P2706	18 54 12.35	–30 25 09.10	M	11.17	01.19	133.73	1.88
SGR_P2708	18 55 57.15	–30 28 50.01	M	10.75	01.22	126.04	2.95
SGR_P2709	18 55 07.13	–30 17 04.56	K	13.61	00.94	141.51	2.10
SGR_P2710	18 54 13.66	–30 33 27.19	K	12.52	00.97	134.82	0.81
SGR_P2712	18 55 37.76	–30 19 27.17	M	11.65	01.11	125.69	1.81
SGR_P2713	18 55 52.65	–30 23 25.82	K	13.57	00.83	11.28	2.65
SGR_P2720	18 54 41.50	–30 40 09.01	K	13.79	00.87	157.40	1.01
SGR_P2722	18 54 33.55	–30 18 00.67	K	12.96	01.02	129.75	3.72
SGR_P2724	18 55 52.98	–30 35 19.68	M	11.84	01.13	122.10	2.16
SGR_P2725	18 56 01.50	–30 27 24.80	M	11.70	01.10	126.39	1.93
SGR_P2726	18 54 59.22	–30 16 05.62	K	13.22	00.89	138.84	2.08
SGR_P2727	18 54 17.39	–30 20 43.12	K	13.49	00.94	138.91	6.06
SGR_P2728	18 54 13.46	–30 35 33.59	M	10.71	01.18	116.59	2.62
SGR_P2732	18 54 09.02	–30 23 20.20	M	09.28	01.29	100.63	126.63
SGR_P2733	18 54 20.39	–30 19 44.50	K	12.97	00.95	139.26	2.33
SGR_P2734	18 55 06.67	–30 15 48.79	M	12.18	01.09	145.17	1.92
SGR_P2735	18 56 03.34	–30 28 42.40	K	12.98	01.01	133.56	3.10
SGR_P2739	18 55 41.93	–30 18 41.72	M	10.92	01.18	125.61	2.49
SGR_P2741	18 56 02.72	–30 31 14.27	M	11.33	01.20	130.78	2.63
SGR_P2742	18 54 02.61	–30 27 47.97	M	10.77	01.12	155.25	3.51
SGR_P2743	18 54 10.32	–30 35 11.72	M	13.28	00.90	149.84	4.09
SGR_P2744	18 56 03.84	–30 30 06.07	M	11.67	01.12	119.36	1.94
SGR_P2746	18 54 46.75	–30 16 01.00	K	13.58	00.84	154.14	2.26

Continued on next page

Table A.1 – continued from previous page

ID	RA	Dec	Spectral Type	2MASS K	2MASS $(J-K)$	v_{rad} (km s^{-1})	σ_{rv} (km s^{-1})
SGR_P2747	18 54 02.66	–30 26 49.03	M	10.91	01.18	116.99	2.19
SGR_P2750	18 56 05.15	–30 28 41.70	K	12.86	00.97	139.73	1.49
SGR_P2751	18 55 29.60	–30 16 33.63	M	12.35	01.07	134.08	1.92
SGR_P2752	18 54 17.54	–30 19 31.31	K	12.81	00.95	136.75	0.91
SGR_P2753	18 54 07.47	–30 22 36.87	K	12.86	00.93	146.06	1.73
SGR_P2754	18 56 05.94	–30 27 46.90	K	12.49	01.05	157.08	1.39
SGR_P2757	18 54 25.51	–30 39 45.60	K	12.57	00.96	137.64	0.87
SGR_P2758	18 55 41.60	–30 17 45.10	K	12.78	00.97	112.69	2.41
SGR_P2760	18 56 05.00	–30 25 05.26	K	13.76	00.90	72.38	91.93
SGR_P2761	18 56 06.19	–30 31 18.51	K	12.71	00.97	120.59	1.37
SGR_P2762	18 55 40.90	–30 39 57.70	K	13.49	00.93	140.19	2.96
SGR_P2764	18 54 55.13	–30 14 56.22	M	11.96	01.12	139.02	1.74
SGR_P2765	18 54 12.72	–30 20 04.09	K	13.02	00.95	124.18	1.37
SGR_P2766	18 54 22.30	–30 17 55.21	K	12.30	00.99	128.47	1.71
SGR_P2768	18 54 57.01	–30 14 48.29	K	13.64	00.91	141.76	4.24
SGR_P2769	18 55 59.87	–30 21 49.28	K	13.44	00.88	134.12	1.99
SGR_P2770	18 54 22.47	–30 17 38.93	K	13.49	00.86	125.21	1.80
SGR_P2773	18 53 59.60	–30 24 23.94	K	13.49	00.89	130.73	3.98
SGR_P2774	18 56 09.77	–30 27 07.04	K	13.80	01.00	156.89	4.49
SGR_P2775	18 56 10.29	–30 28 34.63	K	13.61	00.93	156.27	1.29
SGR_P2776	18 53 56.51	–30 27 20.58	M	11.28	01.08	150.81	1.74
SGR_P2778	18 54 04.97	–30 36 02.93	M	11.37	01.11	139.74	2.36
SGR_P2779	18 55 48.84	–30 39 28.67	K	13.63	00.94	141.92	2.57
SGR_P2780	18 53 57.47	–30 25 09.46	M	11.43	01.10	141.94	3.98

Continued on next page

Table A.1 – continued from previous page

ID	RA	Dec	Spectral Type	2MASS K	2MASS $(J-K)$	v_{rad} (km s^{-1})	σ_{rv} (km s^{-1})
SGR_P2781	18 54 56.18	–30 14 08.00	M	10.54	01.22	122.36	3.56
SGR_P2782	18 54 23.02	–30 40 34.30	K	12.94	00.91	139.99	1.39
SGR_P2783	18 56 06.28	–30 34 22.02	K	13.41	00.88	146.20	2.97
SGR_P2784	18 55 33.32	–30 15 30.29	K	12.96	00.99	150.32	2.11
SGR_P2788	18 54 25.96	–30 41 14.08	M	12.05	01.09	135.95	1.60
SGR_P2789	18 56 10.12	–30 24 54.28	K	13.78	00.98	134.38	3.01
SGR_P2792	18 54 19.18	–30 40 12.71	K	12.91	00.95	143.70	1.58
SGR_P2793	18 54 33.68	–30 42 14.10	M	12.49	00.97	140.24	2.24
SGR_P2794	18 55 15.28	–30 13 55.68	M	12.11	01.07	118.09	1.39
SGR_P2795	18 56 13.78	–30 28 24.77	M	13.18	00.88	187.84	142.78
SGR_P2796	18 54 02.14	–30 36 21.85	K	12.06	01.00	143.88	0.77
SGR_P2797	18 55 55.54	–30 18 23.92	M	11.81	01.08	116.75	1.73
SGR_P2801	18 55 16.82	–30 13 33.49	K	12.69	01.02	129.75	1.16
SGR_P2803	18 54 30.49	–30 42 26.97	K	13.68	00.96	139.72	1.62
SGR_P2804	18 53 57.12	–30 34 54.38	K	12.89	01.01	141.47	0.45
SGR_P2807	18 53 52.07	–30 25 19.47	K	12.61	00.95	134.51	1.06
SGR_P2808	18 54 03.33	–30 19 43.39	K	13.73	00.87	143.90	4.31
SGR_P2809	18 54 13.31	–30 17 13.61	K	13.38	00.88	147.26	1.05
SGR_P2810	18 53 56.18	–30 22 26.84	M	11.40	01.13	144.47	4.27
SGR_P2812	18 56 14.05	–30 33 00.10	K	13.51	00.95	138.09	1.32
SGR_P2813	18 56 15.41	–30 25 40.48	K	13.09	00.90	144.16	3.06
SGR_P2814	18 54 25.37	–30 42 21.36	M	12.27	01.03	143.28	1.70
SGR_P2816	18 54 21.66	–30 41 54.31	K	13.51	00.95	160.04	1.60
SGR_P2817	18 56 14.47	–30 24 15.35	K	13.00	00.98	129.91	1.18

Continued on next page

Table A.1 – continued from previous page

ID	RA	Dec	Spectral Type	2MASS K	2MASS $(J-K)$	v_{rad} (km s^{-1})	σ_{rv} (km s^{-1})
SGR_P2818	18 56 13.02	–30 23 11.89	K	13.20	00.97	146.62	1.67
SGR_P2820	18 55 52.28	–30 16 34.97	K	13.40	00.89	150.49	2.40
SGR_P2821	18 54 36.20	–30 13 40.84	K	13.17	00.94	157.65	2.08
SGR_P2822	18 54 46.56	–30 44 26.52	K	13.28	00.98	144.86	2.94
SGR_P2824	18 55 55.43	–30 40 26.05	K	12.71	01.01	143.71	1.47
SGR_P2825	18 54 30.30	–30 43 20.74	M	11.34	01.13	131.30	1.33
SGR_P2826	18 55 35.45	–30 13 57.07	K	13.22	00.95	129.86	2.15
SGR_P2827	18 54 42.10	–30 13 02.48	M	10.80	01.18	127.81	4.15
SGR_P2828	18 54 06.34	–30 39 31.59	K	12.71	01.00	145.43	0.50
SGR_P2830	18 56 19.17	–30 27 25.39	K	13.41	00.87	-45.62	3.47
SGR_P2831	18 54 08.33	–30 40 07.29	K	12.94	00.92	79.58	1.10
SGR_P2832	18 56 13.30	–30 35 17.14	K	13.69	00.94	78.46	114.35
SGR_P2833	18 54 12.40	–30 41 01.70	K	13.54	00.91	154.19	2.21
SGR_P2834	18 56 17.10	–30 23 50.18	M	10.93	01.21	129.91	3.07
SGR_P2835	18 53 49.37	–30 34 06.07	M	13.30	00.86	39.34	63.71
SGR_P2840	18 56 21.88	–30 28 24.27	K	13.19	00.90	146.95	1.30
SGR_P2841	18 53 45.23	–30 30 55.87	K	12.78	00.97	144.49	1.68
SGR_P2842	18 55 53.28	–30 15 36.02	K	13.55	00.83	128.01	3.25
SGR_P2844	18 56 22.30	–30 30 42.80	M	11.53	01.07	158.82	2.04
SGR_P2846	18 55 13.73	–30 11 39.12	M	13.07	00.91	103.39	138.41
SGR_P2847	18 55 48.46	–30 14 27.45	K	11.31	01.08	-69.83	1.22
SGR_P2850	18 54 19.45	–30 14 10.71	K	13.66	00.89	132.01	3.02
SGR_P2851	18 54 31.47	–30 12 43.25	K	13.67	00.84	116.73	3.10
SGR_P2853	18 54 57.16	–30 46 07.57	K	13.22	00.95	133.97	2.81

Continued on next page

Table A.1 – continued from previous page

ID	RA	Dec	Spectral Type	2MASS K	$(J-K)$	v_{rad} (km s^{-1})	σ_{rv} (km s^{-1})
SGR_P2855	18 54 07.47	–30 41 27.78	M	11.48	01.11	135.15	1.66
SGR_P2856	18 55 30.32	–30 12 10.21	K	13.67	00.85	149.22	1.31
SGR_P2857	18 56 24.13	–30 26 27.59	M	11.71	01.02	138.07	2.22
SGR_P2858	18 56 10.40	–30 38 46.87	M	13.51	00.91	41.38	103.61
SGR_P2859	18 54 29.31	–30 44 44.55	K	13.14	00.91	120.14	1.69
SGR_P2860	18 56 20.55	–30 22 57.14	M	10.27	01.23	125.62	7.30
SGR_P2861	18 55 36.12	–30 12 30.76	K	13.06	00.92	140.71	2.92
SGR_P2862	18 56 25.33	–30 27 44.01	K	12.77	00.98	108.10	1.44
SGR_P2863	18 54 50.85	–30 11 11.16	K	12.85	00.96	142.92	1.49
SGR_P2864	18 56 04.59	–30 16 52.76	K	13.65	00.84	155.77	4.04
SGR_P2865	18 54 00.56	–30 40 15.81	K	12.65	00.97	154.13	0.94
SGR_P2866	18 54 24.90	–30 12 58.75	M	11.36	01.10	140.38	2.69
SGR_P2868	18 53 49.58	–30 36 53.22	M	11.20	01.15	135.46	1.49
SGR_P2869	18 56 21.01	–30 34 59.44	K	13.77	00.96	140.56	2.49
SGR_P2872	18 56 26.53	–30 29 16.01	K	12.44	00.95	136.73	1.07
SGR_P2874	18 53 55.98	–30 18 01.36	K	13.45	00.85	162.72	2.10
SGR_P2875	18 56 15.01	–30 38 02.72	K	13.42	00.90	137.51	1.32
SGR_P2876	18 55 47.71	–30 13 23.26	M	13.62	00.86	22.31	108.95
SGR_P2878	18 56 00.94	–30 41 54.13	M	10.00	01.25	127.28	5.17
SGR_P2879	18 53 57.63	–30 17 18.77	K	13.42	00.84	130.80	1.41
SGR_P2881	18 55 22.82	–30 10 58.69	M	12.96	00.90	123.11	114.88
SGR_P2882	18 55 01.70	–30 10 27.97	K	13.19	00.93	144.14	1.96
SGR_P2883	18 53 43.02	–30 34 34.53	K	13.01	00.91	135.82	2.09
SGR_P2885	18 53 49.02	–30 19 48.40	K	13.39	00.94	34.45	4.60

Continued on next page

Table A.1 – continued from previous page

ID	RA	Dec	Spectral Type	2MASS K	2MASS $(J-K)$	v_{rad} (km s^{-1})	σ_{rv} (km s^{-1})
SGR_P2886	18 56 19.72	–30 36 53.58	M	11.05	01.18	137.76	2.58
SGR_P2887	18 53 58.42	–30 40 40.58	K	12.88	00.94	143.16	1.51
SGR_P2889	18 53 38.22	–30 31 00.06	K	13.05	00.94	150.63	2.40
SGR_P2891	18 54 22.38	–30 12 23.81	K	13.61	00.84	118.67	5.30
SGR_P2892	18 55 41.14	–30 11 59.27	M	13.78	00.92	138.50	132.61
SGR_P2893	18 54 29.73	–30 11 21.86	M	09.73	01.28	131.01	4.12
SGR_P2894	18 56 23.81	–30 35 58.88	K	13.30	01.00	147.84	1.10
SGR_P2898	18 53 57.07	–30 41 09.14	K	12.60	00.95	137.65	0.94
SGR_P2899	18 53 52.49	–30 17 29.11	K	13.03	01.02	137.00	1.96
SGR_P2901	18 53 41.89	–30 21 26.47	K	13.67	00.94	153.97	2.13
SGR_P2903	18 56 30.39	–30 31 47.49	K	13.52	00.89	132.10	1.34
SGR_P2904	18 54 30.52	–30 46 22.70	K	13.65	00.92	147.99	2.00
SGR_P2905	18 56 22.00	–30 37 28.78	K	11.57	01.06	159.35	1.54
SGR_P2906	18 55 12.65	–30 09 43.59	K	12.75	01.00	142.69	0.97
SGR_P2909	18 54 01.07	–30 14 49.31	K	13.35	00.94	137.28	2.61
SGR_P2911	18 56 25.56	–30 36 48.14	K	12.26	00.99	144.07	1.82
SGR_P2912	18 54 38.62	–30 09 57.64	K	13.53	00.92	130.06	0.89
SGR_P2913	18 54 33.70	–30 10 12.55	K	13.51	00.89	143.44	1.69
SGR_P2914	18 53 48.38	–30 17 34.30	M	11.80	01.12	119.51	2.16
SGR_P2915	18 55 46.47	–30 11 25.98	K	12.46	00.95	173.65	0.86
SGR_P2916	18 55 39.77	–30 10 42.55	M	13.65	00.89	-22.42	6.80
SGR_P2917	18 54 45.37	–30 48 02.67	M	13.15	00.87	-2.71	5.56
SGR_P2921	18 53 31.46	–30 30 20.88	K	12.81	00.95	146.85	1.15
SGR_P2922	18 56 35.14	–30 26 51.51	K	13.19	00.88	137.07	1.60

Continued on next page

Table A.1 – continued from previous page

ID	RA	Dec	Spectral Type	2MASS K	$(J-K)$	v_{rad} (km s^{-1})	σ_{rv} (km s^{-1})
SGR_P2923	18 56 22.35	–30 39 00.03	M	11.02	01.17	142.93	2.28
SGR_P2924	18 54 55.33	–30 48 38.38	K	11.18	01.05	157.73	1.76
SGR_P2926	18 56 34.88	–30 24 43.56	K	12.61	00.96	122.71	2.42
SGR_P2928	18 56 34.16	–30 33 41.19	K	13.72	00.85	155.96	4.64
SGR_P2930	18 56 36.66	–30 26 50.59	K	13.73	00.91	155.45	4.64
SGR_P2931	18 53 51.00	–30 15 49.62	M	11.73	01.16	138.72	2.13
SGR_P2933	18 54 19.65	–30 46 43.15	K	12.70	00.99	156.14	2.59
SGR_P2937	18 56 34.76	–30 34 03.78	K	12.12	01.07	150.22	1.33
SGR_P2938	18 54 24.05	–30 10 07.72	M	11.36	01.15	128.64	1.83
SGR_P2940	18 53 42.42	–30 18 02.98	K	12.98	00.97	150.82	3.20
SGR_P2943	18 53 28.10	–30 30 52.52	M	10.56	01.24	134.17	5.14
SGR_P2944	18 55 37.92	–30 09 29.39	K	13.61	00.91	136.11	1.18
SGR_P2945	18 54 58.15	–30 08 05.59	K	13.41	00.84	140.70	1.32
SGR_P2946	18 53 43.10	–30 40 04.09	K	13.21	00.88	170.89	0.80
SGR_P2949	18 53 27.51	–30 30 29.50	M	13.06	00.90	62.29	142.73
SGR_P2953	18 53 39.61	–30 39 12.08	M	11.82	01.08	150.13	2.16
SGR_P2956	18 53 26.44	–30 27 07.66	M	12.72	00.91	90.93	136.34
SGR_P2957	18 54 58.09	–30 07 44.17	M	13.44	00.87	139.43	107.59
SGR_P2959	18 53 37.96	–30 18 31.96	K	13.41	00.89	138.22	2.25
SGR_P2960	18 56 25.23	–30 40 10.07	K	12.01	01.04	156.08	1.07
SGR_P2963	18 55 55.16	–30 10 48.54	K	13.71	00.82	74.22	1.63
SGR_P2965	18 54 05.83	–30 45 52.90	K	12.83	00.96	152.70	2.30
SGR_P2966	18 53 47.46	–30 42 17.00	K	13.39	00.96	150.38	1.97
SGR_P2967	18 53 40.30	–30 17 15.63	M	11.77	01.10	141.22	2.52

Continued on next page

Table A.1 – continued from previous page

ID	RA	Dec	Spectral Type	2MASS K	$(J-K)$	v_{rad} (km s^{-1})	σ_{rv} (km s^{-1})
SGR_P2969	18 56 40.70	–30 32 47.68	K	13.02	00.97	136.08	0.92
SGR_P2970	18 53 55.99	–30 44 27.36	K	12.53	00.95	121.78	0.99
SGR_P2971	18 56 42.58	–30 28 44.97	M	11.77	01.09	123.66	2.21
SGR_P2973	18 56 38.92	–30 34 45.82	M	12.18	01.07	129.14	2.21
SGR_P2975	18 56 14.78	–30 43 41.83	M	11.07	01.16	132.14	2.40
SGR_P2979	18 54 58.27	–30 07 08.33	M	13.18	00.92	32.91	4.94
SGR_P2980	18 56 27.88	–30 40 23.18	K	12.04	00.99	139.13	1.46
SGR_P2982	18 55 22.41	–30 07 25.17	K	13.17	00.99	135.54	1.33
SGR_P2986	18 53 41.50	–30 41 29.93	K	12.62	00.98	155.99	1.30
SGR_P2988	18 53 38.09	–30 17 01.87	K	12.77	00.97	146.72	2.30
SGR_P2989	18 54 45.29	–30 07 08.02	K	13.29	00.92	138.19	2.05
SGR_P2991	18 56 45.18	–30 30 12.31	K	13.57	00.90	166.14	3.30
SGR_P2992	18 56 40.45	–30 35 34.79	K	12.28	01.03	151.10	1.28
SGR_P2994	18 53 25.54	–30 35 24.76	K	12.23	00.96	177.90	1.27
SGR_P2997	18 55 59.97	–30 10 15.00	M	12.69	00.99	129.98	1.39
SGR_P2998	18 56 33.83	–30 39 20.53	K	13.23	00.86	133.28	3.02
SGR_P3000	18 53 49.93	–30 13 06.86	K	13.50	00.88	152.26	4.21
SGR_P3004	18 53 22.36	–30 23 47.38	K	12.73	00.99	158.62	2.65
SGR_P3006	18 53 34.45	–30 17 12.04	K	13.07	00.99	146.80	1.99
SGR_P3007	18 56 46.99	–30 30 35.62	K	13.51	00.90	135.47	4.57
SGR_P3008	18 55 17.97	–30 06 30.32	K	13.34	01.00	146.91	2.58
SGR_P3009	18 56 47.30	–30 27 01.62	M	11.29	01.14	143.10	2.11
SGR_P3011	18 53 51.02	–30 12 25.51	M	11.32	01.08	149.47	2.38
SGR_P3012	18 56 46.81	–30 25 08.99	K	11.60	01.05	132.83	0.76

Continued on next page

Table A.1 – continued from previous page

ID	RA	Dec	Spectral Type	2MASS K	2MASS $(J-K)$	v_{rad} (km s^{-1})	σ_{rv} (km s^{-1})
SGR_P3013	18 56 47.40	–30 31 37.28	M	11.93	01.06	131.71	1.86
SGR_P3015	18 54 42.88	–30 50 55.68	K	12.26	00.97	140.18	1.12
SGR_P3016	18 55 16.81	–30 06 13.55	K	13.63	00.83	138.45	1.23
SGR_P3019	18 55 03.42	–30 05 57.87	K	13.73	00.87	121.50	2.74
SGR_P3020	18 53 20.42	–30 23 30.38	M	11.70	01.09	124.87	2.56
SGR_P3021	18 53 40.89	–30 43 00.89	K	13.64	00.89	151.87	3.21
SGR_P3022	18 54 41.25	–30 06 18.93	M	13.78	00.91	109.71	117.33
SGR_P3024	18 53 16.17	–30 29 23.61	K	12.72	01.00	130.89	2.12
SGR_P3025	18 55 55.41	–30 08 30.45	M	12.11	01.06	119.06	2.22
SGR_P3026	18 55 28.96	–30 06 14.21	K	13.50	00.85	132.97	1.22
SGR_P3028	18 56 49.56	–30 25 11.94	K	12.46	00.97	139.25	1.80
SGR_P3029	18 55 46.93	–30 07 31.33	K	12.27	00.96	120.57	0.89
SGR_P3031	18 56 35.26	–30 40 54.69	K	13.37	00.91	120.41	1.79
SGR_P3034	18 53 32.71	–30 15 58.09	K	12.82	00.94	145.18	3.35
SGR_P3039	18 53 18.76	–30 22 14.61	K	13.65	00.99	-27.25	5.38
SGR_P3043	18 54 36.22	–30 51 27.45	M	13.72	00.93	135.73	133.21
SGR_P3044	18 55 36.00	–30 06 16.12	M	11.95	01.05	130.40	0.86
SGR_P3045	18 54 28.31	–30 06 24.84	K	12.61	00.98	135.90	1.23
SGR_P3047	18 53 45.22	–30 45 14.49	K	12.63	00.93	148.58	1.16
SGR_P3050	18 56 46.24	–30 37 18.02	M	13.33	00.88	116.06	115.18
SGR_P3051	18 55 56.42	–30 07 46.34	K	13.06	00.93	151.62	2.07
SGR_P3052	18 53 13.59	–30 25 17.86	K	13.10	00.98	152.04	1.72
SGR_P3055	18 53 12.91	–30 32 03.72	K	12.94	00.98	146.12	2.95
SGR_P3058	18 53 19.78	–30 37 40.31	K	12.75	01.00	160.91	0.62

Continued on next page

Table A.1 – continued from previous page

ID	RA	Dec	Spectral Type	2MASS K	$(J-K)$	v_{rad} (km s^{-1})	σ_{rv} (km s^{-1})
SGR_P3067	18 53 30.11	–30 14 44.84	K	13.56	00.93	142.34	4.80
SGR_P3072	18 56 55.94	–30 32 48.04	K	13.07	00.97	140.54	1.64
SGR_P3074	18 56 57.51	–30 27 08.28	K	13.75	00.89	182.81	7.11
SGR_P3076	18 56 06.70	–30 08 06.21	K	13.48	00.91	144.83	4.02
SGR_P3078	18 53 13.07	–30 21 40.12	K	12.87	00.96	146.69	2.65
SGR_P3081	18 55 10.75	–30 03 56.81	M	13.44	00.90	10.74	7.08
SGR_P3082	18 53 09.23	–30 32 41.34	M	13.65	00.84	170.80	101.37
SGR_P3085	18 56 59.12	–30 26 31.69	M	11.08	01.14	169.46	3.39
SGR_P3086	18 54 47.95	–30 03 49.75	M	13.59	00.88	4.21	156.47
SGR_P3087	18 53 17.77	–30 18 06.66	M	13.79	00.93	164.12	127.17
SGR_P3088	18 55 09.29	–30 03 38.22	K	13.74	00.93	132.06	3.33
SGR_P3094	18 53 06.02	–30 29 20.68	K	13.43	00.85	144.97	6.58
SGR_P3102	18 56 47.79	–30 40 30.66	M	11.74	01.14	146.22	1.87
SGR_P3103	18 57 01.16	–30 30 02.92	M	11.74	01.11	142.76	2.61
SGR_P3113	18 55 34.53	–30 04 00.02	K	12.61	00.98	12.03	1.22
SGR_P3117	18 53 38.93	–30 46 56.19	K	12.98	00.92	122.76	0.65
SGR_P3118	18 53 04.67	–30 31 43.59	K	11.81	01.04	133.32	1.21
SGR_P3120	18 56 57.09	–30 36 36.78	M	11.53	01.02	134.86	2.06
SGR_P3121	18 53 03.67	–30 28 35.03	K	12.42	01.04	154.84	1.64
SGR_P3124	18 53 19.80	–30 41 43.54	M	10.56	01.20	140.60	3.20
SGR_P3126	18 53 31.06	–30 12 10.58	K	13.69	00.86	-70.97	116.69
SGR_P3127	18 53 44.40	–30 48 18.61	M	12.03	01.02	148.38	2.88
SGR_P3128	18 53 03.08	–30 27 33.65	M	10.87	01.09	130.26	2.83
SGR_P3130	18 53 02.62	–30 29 48.87	K	12.91	00.97	156.97	3.41

Continued on next page

Table A.1 – continued from previous page

ID	RA	Dec	Spectral Type	2MASS K	2MASS $(J-K)$	v_{rad} (km s^{-1})	σ_{rv} (km s^{-1})
SGR_P3136	18 54 06.66	–30 51 59.43	K	13.73	00.84	136.22	2.75
SGR_P3143	18 53 02.48	–30 24 11.54	K	13.37	00.91	145.88	1.89
SGR_P3148	18 53 30.84	–30 46 42.09	C	13.53	00.83	149.69	1.43
SGR_P3152	18 54 05.33	–30 52 32.95	M	11.51	01.08	128.06	1.82
SGR_P3153	18 57 08.13	–30 28 14.24	K	12.62	00.92	128.99	2.86
SGR_P3157	18 55 34.42	–30 02 34.47	K	12.46	01.00	155.09	2.90
SGR_P3163	18 56 52.57	–30 42 20.77	M	10.93	01.17	142.03	3.17
SGR_P3164	18 53 18.12	–30 13 43.65	M	10.39	01.17	140.49	1.93
SGR_P3170	18 54 32.41	–30 55 15.87	K	13.39	00.87	139.21	3.35
SGR_P3171	18 57 10.27	–30 30 29.68	K	11.81	01.02	132.53	2.04
SGR_P3176	18 57 11.08	–30 29 50.83	K	13.03	00.96	149.42	1.62
SGR_P3183	18 54 21.19	–30 54 59.76	M	13.65	00.85	-60.84	6.10
SGR_P3184	18 55 31.25	–30 01 33.83	K	13.72	00.93	155.68	2.21
SGR_P3185	18 53 22.25	–30 46 06.29	M	12.00	00.99	149.46	2.39
SGR_P3186	18 54 12.32	–30 54 19.62	K	13.76	00.89	162.89	1.10
SGR_P3187	18 54 24.13	–30 55 19.73	M	13.10	00.87	75.91	135.81
SGR_P3192	18 57 05.29	–30 38 20.93	K	12.28	01.06	134.20	1.74
SGR_P3193	18 53 19.40	–30 11 47.38	K	11.95	01.02	156.33	1.97
SGR_P3194	18 52 53.30	–30 31 24.36	K	13.70	00.82	155.93	6.34
SGR_P3195	18 53 08.31	–30 15 25.12	K	12.51	00.97	120.56	2.03
SGR_P3201	18 57 01.00	–30 41 11.09	K	12.92	00.91	143.39	2.95
SGR_P3204	18 53 14.94	–30 12 45.27	M	10.87	01.18	124.88	3.02
SGR_P3205	18 57 05.61	–30 39 09.12	K	13.75	00.88	120.57	6.93
SGR_P3206	18 53 12.05	–30 13 36.95	M	13.52	00.92	185.48	4.78

Continued on next page

Table A.1 – continued from previous page

ID	RA	Dec	Spectral Type	2MASS K	2MASS $(J-K)$	v_{rad} (km s^{-1})	σ_{rv} (km s^{-1})
SGR_P3207	18 53 45.23	–30 51 34.08	K	13.36	00.85	132.31	2.43
SGR_P3208	18 55 27.47	–30 00 49.88	K	13.34	00.91	165.30	1.74
SGR_P3213	18 53 08.35	–30 42 45.85	M	10.48	01.17	150.25	5.26
SGR_P3214	18 52 52.53	–30 24 32.31	M	11.26	01.14	128.17	2.42
SGR_P3216	18 53 21.79	–30 10 26.27	K	13.68	00.84	137.72	2.47
SGR_P3218	18 53 15.23	–30 12 10.33	K	12.29	01.00	125.99	2.00
SGR_P3219	18 53 07.74	–30 14 37.39	K	13.61	00.94	152.34	3.42
SGR_P3220	18 53 37.59	–30 50 37.55	K	13.22	00.90	152.55	1.68
SGR_P3222	18 53 44.32	–30 51 53.87	K	13.00	00.88	155.39	1.93
SGR_P3223	18 57 09.74	–30 37 57.62	M	11.40	01.12	151.17	3.40
SGR_P3228	18 53 08.91	–30 43 49.88	M	11.26	01.08	141.08	2.67
SGR_P3232	18 57 16.54	–30 33 02.35	M	11.64	01.11	131.12	1.56
SGR_P3239	18 52 48.27	–30 30 13.64	K	13.58	00.87	-20.75	2.71
SGR_P3240	18 53 11.80	–30 12 15.99	M	11.43	01.06	-33.60	2.84
SGR_P3242	18 54 19.76	–30 56 22.62	K	12.46	00.96	160.22	1.35
SGR_P3244	18 53 52.10	–30 53 39.07	K	12.74	00.97	132.16	0.97
SGR_P3252	18 53 18.17	–30 47 33.99	M	13.61	00.83	196.39	4.62
SGR_P3258	18 53 53.90	–30 54 13.20	M	13.06	00.94	134.15	2.17
SGR_P3259	18 54 01.86	–30 55 14.71	M	11.33	01.17	137.93	3.00
SGR_P3260	18 57 16.05	–30 36 40.72	K	12.61	01.02	154.41	2.63
SGR_P3284	18 53 00.11	–30 14 12.90	K	13.25	00.95	133.36	3.04
SGR_P3285	18 52 43.97	–30 24 44.95	K	12.91	00.90	135.45	2.81
SGR_P3299	18 53 12.87	–30 47 48.01	K	12.97	00.88	128.75	2.57
SGR_P3315	18 52 55.37	–30 14 54.70	M	12.21	01.01	130.07	2.46

Continued on next page

Table A.1 – continued from previous page

ID	RA	Dec	Spectral Type	2MASS K	$(J-K)$	v_{rad} (km s^{-1})	σ_{rv} (km s^{-1})
SGR_P3316	18 52 49.79	–30 17 37.19	M	11.40	01.13	127.70	2.44
SGR_P3320	18 57 23.56	–30 35 28.19	K	13.54	00.94	138.23	2.67
SGR_P3340	18 52 38.18	–30 27 51.08	M	11.36	01.05	127.77	3.01
SGR_P3348	18 54 00.83	–30 57 11.06	K	13.10	00.95	152.95	1.45
SGR_P3357	18 52 40.27	–30 21 03.41	K	13.62	00.87	145.80	2.48
SGR_P3366	18 52 37.80	–30 23 03.30	K	13.46	00.90	136.83	7.29
SGR_P3384	18 52 57.75	–30 11 16.66	M	11.39	01.17	119.53	2.33
SGR_P3406	18 57 31.09	–30 35 19.26	K	12.12	01.03	165.72	1.26
SGR_P3411	18 52 33.99	–30 23 42.57	K	12.95	00.91	149.03	3.43
SGR_P3422	18 57 30.62	–30 36 54.30	M	13.21	00.89	-45.09	2.59
SGR_P3431	18 52 40.24	–30 17 20.78	K	13.01	00.89	158.13	2.94
SGR_P3433	18 52 33.35	–30 22 30.53	M	10.73	01.18	140.19	5.76
SGR_P3449	18 57 34.95	–30 34 46.28	M	11.83	01.09	116.37	1.31
SGR_P3456	18 52 40.17	–30 16 04.24	K	13.69	00.86	153.45	4.95
SGR_P3460	18 57 33.13	–30 37 33.92	M	11.38	01.17	132.47	2.52
SGR_P3463	18 52 43.58	–30 14 02.92	M	11.92	01.00	148.63	3.81
SGR_P3466	18 57 34.84	–30 36 34.99	K	13.65	00.86	144.96	3.64
SGR_P3482	18 57 30.17	–30 40 43.70	M	11.13	01.20	141.78	2.40
SGR_P3489	18 57 40.35	–30 32 17.86	M	10.67	01.20	127.72	4.96
SGR_P3491	18 57 38.39	–30 35 33.36	K	12.63	00.94	158.36	1.49
SGR_P3494	18 57 32.62	–30 40 20.80	K	13.61	00.86	156.15	2.33
SGR_P3507	18 57 42.05	–30 33 59.05	K	12.88	00.92	128.79	2.22
SGR_P3527	18 57 35.65	–30 40 33.74	M	13.24	00.92	-18.76	8.97
SGR_P3533	18 52 27.60	–30 18 49.33	K	12.39	00.97	153.37	3.03

Continued on next page

Table A.1 – continued from previous page

ID	RA	Dec	Spectral Type	2MASS K	2MASS $(J - K)$	v_{rad} (km s^{-1})	σ_{rv} (km s^{-1})
SGR_P3550	18 57 21.77	–30 47 58.40	C	10.83	01.21	159.80	0.00
SGR_P3558	18 57 48.31	–30 32 35.47	K	12.85	01.03	142.20	1.98
SGR_P3567	18 57 48.42	–30 33 37.30	K	12.09	00.98	146.38	0.80
SGR_P3568	18 57 38.64	–30 41 48.75	M	11.67	01.13	158.01	1.22
SGR_P3572	18 57 48.02	–30 34 45.06	K	12.92	00.98	163.03	1.64
SGR_P3596	18 57 51.58	–30 32 00.07	M	09.89	01.31	126.44	3.63
SGR_P3607	18 52 39.25	–30 09 16.29	M	09.55	01.26	122.28	140.06
SGR_P3615	18 57 53.64	–30 32 48.35	K	12.01	01.00	173.59	0.73
SGR_P3620	18 52 55.81	–30 03 55.42	M	12.08	01.05	119.68	2.73
SGR_P3624	18 57 53.21	–30 34 53.59	M	11.29	01.22	137.86	2.08
SGR_P3626	18 57 38.37	–30 45 05.59	K	13.40	00.91	156.35	2.61
SGR_P3627	18 57 53.27	–30 35 12.09	K	13.04	00.92	130.88	2.12
SGR_P3638	18 52 39.60	–30 07 45.99	M	12.24	00.99	131.13	6.64
SGR_P3639	18 57 45.78	–30 42 05.81	M	12.96	00.96	19.60	79.18
SGR_P3662	18 57 31.82	–30 48 44.71	K	13.52	00.95	138.31	2.61
SGR_P3672	18 57 41.12	–30 45 30.45	K	11.72	01.01	144.85	1.06
SGR_P3676	18 52 54.91	–30 02 50.08	M	11.28	01.08	146.71	3.36
SGR_P3682	18 57 59.63	–30 31 24.70	K	12.72	00.93	134.06	0.59
SGR_P3694	18 58 00.56	–30 29 52.08	K	12.79	00.95	128.82	3.58
SGR_P3703	18 57 44.69	–30 45 06.09	K	12.60	01.03	142.76	0.93
SGR_P3707	18 57 51.63	–30 41 39.89	K	12.57	00.98	142.18	1.55
SGR_P3716	18 58 02.30	–30 31 02.45	K	12.51	00.98	143.25	1.46
SGR_P3717	18 52 44.42	–30 04 20.62	K	13.60	00.89	152.88	6.10
SGR_P3722	18 57 59.22	–30 37 15.83	K	12.53	01.02	128.72	1.18

Continued on next page

Table A.1 – continued from previous page

ID	RA	Dec	Spectral Type	2MASS K	2MASS $(J-K)$	v_{rad} (km s^{-1})	σ_{rv} (km s^{-1})
SGR_P3725	18 52 48.03	–30 02 59.18	K	13.76	00.84	82.55	136.91
SGR_P3750	18 57 58.25	–30 40 16.30	M	13.61	00.91	191.77	113.37
SGR_P3753	18 57 37.12	–30 50 11.27	M	11.62	01.09	124.44	2.27
SGR_P3758	18 57 34.84	–30 51 08.13	K	12.98	00.94	132.41	1.45
SGR_P3768	18 57 59.23	–30 41 06.46	K	13.59	00.83	136.61	1.41
SGR_P3769	18 52 26.03	–30 07 47.72	M	11.00	01.10	141.73	4.68
SGR_P3772	18 52 48.82	–30 01 15.90	K	12.94	00.98	151.39	2.03
SGR_P3783	18 52 21.02	–30 09 02.70	M	11.52	01.04	132.39	3.96
SGR_P3784	18 52 48.10	–30 01 05.38	K	13.15	00.96	141.20	1.94
SGR_P3785	18 52 59.17	–29 58 44.18	K	11.78	01.03	159.58	2.96
SGR_P3812	18 52 39.34	–30 01 57.05	K	13.23	00.88	152.07	2.99
SGR_P3813	18 58 13.20	–30 31 45.33	K	12.45	01.03	135.47	1.42
SGR_P3816	18 52 17.73	–30 08 32.40	M	10.98	01.06	126.33	2.39
SGR_P3823	18 58 06.75	–30 40 27.60	K	13.42	00.86	146.51	1.78
SGR_P3825	18 52 22.92	–30 06 17.87	M	11.69	01.14	152.11	3.98
SGR_P3836	18 57 51.28	–30 48 57.22	K	12.54	00.94	135.13	1.65
SGR_P3841	18 52 30.83	–30 03 24.19	K	12.72	00.96	140.39	2.49
SGR_P3847	18 58 01.67	–30 44 42.48	K	12.52	00.98	148.33	2.03
SGR_P3874	18 58 19.43	–30 29 48.47	M	11.48	01.16	133.63	2.56
SGR_P3894	18 58 18.53	–30 36 12.27	K	13.22	00.92	156.55	2.08
SGR_P3903	18 57 56.21	–30 49 52.82	K	12.82	01.08	136.09	1.46
SGR_P3907	18 52 57.86	–29 55 25.54	K	12.89	00.98	161.12	8.58
SGR_P3912	18 58 18.55	–30 37 53.98	K	12.16	01.06	133.78	0.94
SGR_P3916	18 52 46.09	–29 57 25.43	K	12.76	00.97	133.03	1.37

Continued on next page

Table A.1 – continued from previous page

ID	RA	Dec	Spectral Type	2MASS K	$(J-K)$	v_{rad} (km s^{-1})	σ_{rv} (km s^{-1})
SGR_P3919	18 52 50.31	–29 56 31.70	C	09.45	01.69	140.81	1.26
SGR_P3927	18 52 16.23	–30 04 39.00	K	13.20	00.95	56.27	99.64
SGR_P3928	18 58 20.11	–30 37 58.65	K	12.74	00.97	138.12	2.08
SGR_P3939	18 51 59.44	–30 10 41.55	K	12.01	00.97	32.05	137.50
SGR_P3940	18 52 38.31	–29 58 24.66	M	10.84	01.17	135.63	3.89
SGR_P3946	18 52 43.52	–29 57 05.52	M	12.41	00.97	80.07	104.48
SGR_P3964	18 58 14.03	–30 44 52.02	M	13.39	00.92	124.12	120.84
SGR_P3968	18 52 31.78	–29 59 00.91	K	13.59	00.91	156.22	2.58
SGR_P3975	18 58 28.51	–30 31 30.90	M	10.74	01.22	139.77	3.14
SGR_P3977	18 52 12.35	–30 04 10.18	K	11.70	01.08	162.42	0.94
SGR_P3982	18 52 04.18	–30 06 50.54	K	13.48	00.94	-4.53	132.06
SGR_P3988	18 52 44.25	–29 55 42.94	M	12.51	01.00	134.18	1.47
SGR_P4029	18 52 14.72	–30 01 48.26	K	13.31	00.96	124.30	1.28
SGR_P4034	18 52 53.41	–29 53 06.06	M	09.85	01.29	124.67	121.88
SGR_P4036	18 52 28.62	–29 58 02.23	M	11.89	01.08	133.52	1.83
SGR_P4044	18 58 32.86	–30 34 05.65	K	13.70	00.86	123.74	1.61
SGR_P4060	18 52 42.86	–29 54 28.39	K	13.62	00.86	56.62	109.07
SGR_P4071	18 52 03.47	–30 04 18.58	K	13.50	00.87	26.53	116.46
SGR_P4106	18 52 07.14	–30 01 52.19	K	13.66	00.90	112.81	3.94
SGR_P4107	18 51 44.64	–30 10 31.23	K	12.70	00.96	1.08	124.44
SGR_P4110	18 52 24.89	–29 57 03.81	K	13.62	00.90	46.66	122.86
SGR_P4111	18 51 51.49	–30 07 17.05	K	13.23	00.86	-10.81	134.42
SGR_P4138	18 58 35.77	–30 39 17.93	K	12.96	00.93	148.40	1.52
SGR_P4148	18 58 20.35	–30 49 15.30	M	13.37	01.06	172.71	4.05

Continued on next page

Table A.1 – continued from previous page

ID	RA	Dec	Spectral Type	2MASS K	2MASS $(J-K)$	v_{rad} (km s^{-1})	σ_{rv} (km s^{-1})
SGR_P4192	18 58 42.60	–30 37 20.15	K	13.11	00.93	127.06	1.14
SGR_P4198	18 58 43.80	–30 36 46.96	M	11.59	01.08	155.29	1.78
SGR_P4204	18 58 19.57	–30 52 02.17	K	12.17	01.03	139.11	1.06
SGR_P4212	18 52 05.80	–29 59 21.09	K	12.84	00.97	131.53	2.71
SGR_P4214	18 52 37.53	–29 52 04.69	M	11.07	01.15	134.41	2.99
SGR_P4215	18 52 18.28	–29 56 05.88	M	13.61	00.82	72.15	2.30
SGR_P4222	18 58 44.29	–30 37 37.94	K	13.14	00.93	156.48	1.59
SGR_P4235	18 52 36.06	–29 52 00.33	K	13.05	00.90	137.21	3.08
SGR_P4236	18 52 01.70	–29 59 58.60	K	13.75	00.88	16.54	123.13
SGR_P4239	18 52 07.09	–29 58 23.97	K	13.65	00.95	132.48	2.99
SGR_P4247	18 58 45.00	–30 38 45.50	M	13.54	00.99	107.45	70.65
SGR_P4253	18 52 17.42	–29 55 30.69	K	12.21	00.98	154.99	0.96
SGR_P4269	18 58 22.92	–30 52 41.19	M	11.49	01.15	132.53	2.16
SGR_P4274	18 58 49.71	–30 35 22.58	M	13.58	00.85	0.69	89.72
SGR_P4278	18 58 33.18	–30 48 23.80	K	12.18	00.97	134.67	1.62
SGR_P4284	18 58 46.14	–30 40 42.34	M	11.58	01.13	132.22	2.48
SGR_P4294	18 58 46.84	–30 41 06.59	K	12.91	00.99	124.79	3.63
SGR_P4302	18 58 44.10	–30 43 38.76	K	13.62	00.86	135.83	3.71
SGR_P4305	18 52 41.04	–29 49 29.52	K	12.39	00.98	13.46	139.18
SGR_P4321	18 51 55.46	–29 59 06.31	K	13.69	00.94	-9.45	136.13
SGR_P4323	18 58 42.71	–30 45 52.43	M	13.46	00.88	72.77	124.82
SGR_P4331	18 51 41.06	–30 03 37.77	C	09.43	02.67	150.38	3.40
SGR_P4332	18 51 59.98	–29 57 35.79	K	13.31	00.93	154.28	3.57
SGR_P4335	18 52 37.86	–29 49 12.01	K	11.69	01.07	19.89	123.89

Continued on next page

Table A.1 – continued from previous page

ID	RA	Dec	Spectral Type	2MASS K	$(J-K)$	v_{rad} (km s^{-1})	σ_{rv} (km s^{-1})
SGR_P4341	18 51 52.17	–29 59 28.22	K	13.68	00.97	-2.42	121.02
SGR_P4359	18 51 45.25	–30 01 08.43	K	12.85	00.94	79.07	89.59
SGR_P4378	18 51 42.23	–30 01 37.05	M	10.78	01.21	136.78	8.49
SGR_P4385	18 58 35.77	–30 52 07.37	K	13.46	00.88	167.81	2.62
SGR_P4396	18 52 02.73	–29 55 08.20	K	13.08	00.96	54.23	119.31
SGR_P4402	18 51 45.34	–29 59 58.93	K	13.04	00.99	106.46	124.27
SGR_P4421	18 58 39.02	–30 52 05.67	M	11.70	01.09	149.58	1.33
SGR_P4426	18 51 43.17	–29 59 43.52	K	13.63	00.84	5.34	120.77
SGR_P4427	18 59 02.54	–30 36 08.91	K	13.35	00.87	172.31	2.69
SGR_P4429	18 58 54.78	–30 43 49.98	M	10.00	01.28	138.72	132.54
SGR_P4430	18 58 42.45	–30 50 50.37	M	11.74	01.13	128.79	1.49
SGR_P4444	18 58 46.63	–30 49 21.98	K	13.38	01.00	132.58	2.45
SGR_P4456	18 58 46.42	–30 50 01.40	M	12.80	00.94	178.39	149.58
SGR_P4458	18 58 58.45	–30 43 07.09	M	12.82	00.99	126.29	3.31
SGR_P4474	18 59 04.24	–30 38 45.22	K	13.53	00.88	140.93	1.61
SGR_P4479	18 52 01.72	–29 53 09.29	K	12.88	01.00	-3.40	133.11
SGR_P4506	18 58 50.10	–30 50 06.22	K	12.86	00.93	140.15	2.76
SGR_P4508	18 51 26.83	–30 03 08.03	M	11.08	01.14	156.66	128.60
SGR_P4539	18 59 05.76	–30 41 05.89	K	12.36	00.98	143.63	1.29
SGR_P4557	18 51 50.17	–29 54 30.96	K	13.13	00.96	35.31	151.69
SGR_P4575	18 52 15.46	–29 48 21.55	K	13.78	01.50	21.63	123.11
SGR_P4582	18 58 57.88	–30 49 05.50	M	13.18	00.98	117.57	152.04
SGR_P4602	18 59 05.24	–30 45 33.24	K	12.47	01.02	141.81	2.38
SGR_P4607	18 59 03.37	–30 46 52.11	K	11.79	01.03	144.17	1.02

Continued on next page

Table A.1 – continued from previous page

ID	RA	Dec	Spectral Type	2MASS K	2MASS $(J-K)$	v_{rad} (km s^{-1})	σ_{rv} (km s^{-1})
SGR_P4621	18 51 44.01	–29 54 39.39	K	12.56	01.04	57.02	141.59
SGR_P4624	18 51 28.18	–29 59 18.28	M	10.28	01.22	198.55	60.64
SGR_P4635	18 58 45.75	–30 56 08.42	K	11.98	01.05	116.94	0.67
SGR_P4637	18 51 35.41	–29 56 40.92	M	11.48	01.14	115.86	122.49
SGR_P4659	18 51 24.65	–29 59 42.98	K	12.88	00.93	8.73	119.18
SGR_P4671	18 51 36.76	–29 55 38.90	M	11.03	01.16	151.60	6.45
SGR_P4693	18 51 30.45	–29 56 54.10	K	12.84	00.99	18.79	125.92
SGR_P4699	18 58 51.68	–30 55 36.65	K	13.22	00.93	147.32	1.13
SGR_P4747	18 58 44.83	–30 59 15.23	M	10.87	01.18	134.73	1.94
SGR_P4771	18 58 58.43	–30 54 54.87	M	12.41	01.02	145.16	2.40
SGR_P4798	18 57 50.18	–31 13 34.98	M	11.58	01.10	122.81	2.77
SGR_P4804	18 51 53.56	–29 48 24.59	M	10.80	01.23	187.88	120.41
SGR_P4810	18 51 36.68	–29 52 21.27	M	11.22	01.15	146.88	99.93
SGR_P4815	18 51 26.92	–29 54 56.76	K	13.51	00.90	-28.18	128.66
SGR_P4828	18 51 15.60	–29 58 10.09	M	11.28	01.18	158.99	180.01
SGR_P4834	18 58 49.06	–31 00 27.18	K	11.84	01.07	146.59	0.93
SGR_P4844	18 59 01.24	–30 56 20.12	M	11.34	01.11	144.77	1.96
SGR_P4869	18 51 35.50	–29 51 20.95	K	12.02	01.08	25.27	125.91
SGR_P4872	18 58 58.43	–30 58 12.00	K	12.54	01.00	136.08	1.02
SGR_P4873	18 58 04.63	–31 12 23.84	K	13.63	00.84	146.86	2.69
SGR_P4877	18 51 31.53	–29 52 07.67	K	12.89	00.92	52.06	124.50
SGR_P4882	18 51 30.00	–29 52 21.60	C	08.97	01.82	145.12	3.86
SGR_P4884	18 58 11.08	–31 11 23.09	M	10.33	01.17	-75.34	5.84
SGR_P4896	18 58 57.32	–30 59 12.09	M	10.80	01.18	119.66	3.01

Continued on next page

Table A.1 – continued from previous page

ID	RA	Dec	Spectral Type	2MASS K	2MASS $(J-K)$	v_{rad} (km s^{-1})	σ_{rv} (km s^{-1})
SGR_P4897	18 58 46.37	–31 02 49.23	K	13.06	00.92	180.28	2.57
SGR_P4947	18 58 49.34	–31 03 02.25	K	12.03	01.04	140.40	1.38
SGR_P4950	18 58 55.16	–31 01 13.28	K	13.53	00.90	151.54	5.57
SGR_P4970	18 58 51.89	–31 02 41.15	K	13.02	00.98	136.72	2.08
SGR_P4974	18 58 46.41	–31 04 24.19	K	12.60	00.95	120.20	1.90
SGR_P4978	18 58 02.68	–31 14 27.41	K	13.59	00.85	146.78	5.48
SGR_P4984	18 59 12.93	–30 55 09.48	K	13.02	00.92	152.74	2.23
SGR_P5005	18 58 19.02	–31 11 41.55	K	13.37	00.88	131.23	6.94
SGR_P5014	18 59 04.43	–30 59 30.32	K	12.88	00.95	147.68	1.02
SGR_P5035	18 59 15.00	–30 55 49.63	K	12.83	00.91	130.17	1.53
SGR_P5040	18 58 48.78	–31 05 15.62	M	10.80	01.13	17.52	4.88
SGR_P5080	18 59 16.94	–30 56 53.74	K	12.58	00.95	127.56	3.88
SGR_P5093	18 59 21.10	–30 55 23.16	K	11.68	01.02	152.82	0.78
SGR_P5113	18 59 15.17	–30 58 31.52	K	12.04	00.98	126.78	1.75
SGR_P5118	18 59 18.56	–30 57 21.50	M	13.38	00.87	134.55	143.58
SGR_P5141	18 57 29.26	–31 22 40.48	K	13.69	00.93	144.93	5.26
SGR_P5143	18 58 21.70	–31 14 19.33	M	10.55	01.24	122.08	3.31
SGR_P5158	18 59 33.95	–30 51 59.21	M	11.92	01.03	147.03	1.81
SGR_P5159	18 59 18.07	–30 59 14.27	K	13.18	00.89	144.80	3.13
SGR_P5161	18 59 03.16	–31 04 28.12	M	10.85	01.11	125.20	2.63
SGR_P5172	18 59 32.23	–30 53 26.51	M	11.32	01.17	134.97	2.13
SGR_P5187	18 59 26.04	–30 56 46.50	M	10.74	01.14	164.57	3.19
SGR_P5208	18 58 23.24	–31 15 17.48	M	13.73	00.89	152.19	143.35
SGR_P5209	18 59 16.84	–31 01 02.79	M	13.15	00.93	90.19	127.36

Continued on next page

Table A.1 – continued from previous page

ID	RA	Dec	Spectral Type	2MASS K	2MASS $(J-K)$	v_{rad} (km s^{-1})	σ_{rv} (km s^{-1})
SGR_P5226	18 59 04.08	–31 05 54.21	M	11.14	01.09	120.98	2.40
SGR_P5236	18 57 53.34	–31 21 14.39	K	13.66	00.90	132.46	2.13
SGR_P5253	18 59 02.64	–31 07 10.99	M	11.67	01.11	144.69	1.86
SGR_P5275	18 59 33.08	–30 57 01.34	K	13.78	00.84	-29.02	4.04
SGR_P5297	18 58 12.58	–31 19 13.75	M	11.72	01.08	154.97	2.57
SGR_P5323	18 58 34.38	–31 15 39.85	M	10.76	01.22	153.75	3.26
SGR_P5326	18 58 40.45	–31 14 22.70	K	13.30	01.02	138.10	1.47
SGR_P5327	18 59 01.48	–31 09 14.04	M	10.67	01.19	127.35	3.09
SGR_P5333	18 59 20.70	–31 03 29.77	K	12.67	01.00	143.15	3.29
SGR_P5339	18 59 20.57	–31 03 41.07	M	10.99	01.19	149.32	2.88
SGR_P5352	18 59 27.12	–31 02 03.80	M	13.64	00.94	19.01	104.96
SGR_P5362	18 57 52.49	–31 23 40.02	M	10.63	01.20	141.26	3.25
SGR_P5373	18 59 25.91	–31 03 00.82	K	12.67	01.01	140.64	1.51
SGR_P5374	18 59 36.94	–30 58 46.62	M	13.39	00.90	62.92	98.56
SGR_P5379	18 59 40.60	–30 57 14.72	M	11.71	01.13	142.67	2.47
SGR_P5387	18 58 51.09	–31 13 21.15	K	12.41	01.01	146.44	2.69
SGR_P5396	18 59 27.64	–31 02 57.21	K	12.32	00.98	145.40	1.30
SGR_P5408	18 57 53.00	–31 24 19.94	K	12.59	01.01	147.57	2.61
SGR_P5412	18 59 55.25	–30 50 38.98	M	11.95	01.08	117.46	2.31
SGR_P5415	18 59 37.88	–30 59 31.97	M	13.22	00.86	95.29	133.21
SGR_P5429	18 59 50.05	–30 54 18.25	K	13.80	00.85	129.75	3.42
SGR_P5433	18 59 26.59	–31 04 16.05	K	13.70	00.88	151.52	2.17
SGR_P5449	18 59 59.04	–30 49 36.66	K	13.01	00.89	-141.52	2.18
SGR_P5460	18 59 44.84	–30 57 48.12	K	13.80	00.87	138.87	5.63

Continued on next page

Table A.1 – continued from previous page

ID	RA	Dec	Spectral Type	2MASS K	$(J-K)$	v_{rad} (km s^{-1})	σ_{rv} (km s^{-1})
SGR_P5478	18 59 13.48	–31 09 35.74	K	13.46	00.92	137.41	3.09
SGR_P5481	18 58 05.82	–31 23 46.20	K	13.74	00.97	149.10	3.49
SGR_P5488	19 00 00.23	–30 50 54.76	K	13.52	00.87	173.10	1.72
SGR_P5501	18 59 33.34	–31 03 48.94	K	12.31	00.99	168.79	1.63
SGR_P5504	18 59 50.93	–30 56 37.58	K	13.62	00.86	129.63	2.30
SGR_P5511	18 59 16.67	–31 09 30.29	K	12.78	00.92	159.87	2.03
SGR_P5515	18 58 16.24	–31 22 44.23	M	12.95	00.89	-4.99	102.57
SGR_P5518	18 59 03.38	–31 13 12.88	K	12.67	01.01	138.72	2.13
SGR_P5538	19 00 02.85	–30 51 39.90	K	13.77	00.82	163.97	2.89
SGR_P5552	18 58 02.58	–31 25 27.14	K	13.03	00.96	125.48	4.23
SGR_P5556	18 59 29.78	–31 06 33.93	K	13.61	00.97	-20.56	135.76
SGR_P5559	18 59 16.29	–31 10 45.10	M	13.66	00.91	256.51	9.34
SGR_P5581	18 59 30.49	–31 06 57.32	K	12.92	00.99	164.49	2.43
SGR_P5593	18 57 44.54	–31 28 34.36	K	13.63	00.97	-20.66	4.83
SGR_P5600	18 59 40.48	–31 04 04.84	K	13.47	01.07	147.48	1.76
SGR_P5603	18 57 42.35	–31 29 02.25	M	10.46	01.18	123.27	4.15
SGR_P5607	18 57 45.40	–31 28 41.33	K	13.66	00.86	57.89	132.11
SGR_P5636	18 58 49.89	–31 18 35.48	M	11.02	01.20	117.24	2.86
SGR_P5644	18 59 33.00	–31 07 34.63	K	12.99	00.93	146.94	2.38
SGR_P5646	18 58 40.95	–31 20 34.80	K	13.11	00.96	157.68	1.94
SGR_P5658	18 58 47.03	–31 19 43.38	K	12.98	01.01	129.76	2.32
SGR_P5665	18 59 32.25	–31 08 34.94	K	12.39	01.02	135.78	3.04
SGR_P5680	19 00 08.34	–30 54 27.50	K	13.49	00.95	144.47	2.34
SGR_P5690	19 00 13.11	–30 51 59.43	K	13.04	00.92	122.48	2.70

Continued on next page

Table A.1 – continued from previous page

ID	RA	Dec	Spectral Type	2MASS K	2MASS $(J-K)$	v_{rad} (km s^{-1})	σ_{rv} (km s^{-1})
SGR_P5691	19 00 09.87	–30 54 00.40	K	13.53	00.94	144.43	2.54
SGR_P5692	18 58 39.46	–31 21 57.49	K	13.57	00.90	150.87	3.92
SGR_P5699	18 59 40.70	–31 06 41.85	K	13.56	00.90	137.74	5.45
SGR_P5715	18 59 02.33	–31 17 33.49	K	12.68	00.99	148.27	1.14
SGR_P5749	18 59 59.39	–31 00 45.17	K	12.44	01.02	128.90	1.23
SGR_P5756	18 58 20.19	–31 26 16.96	M	13.10	00.89	44.84	121.04
SGR_P5764	18 59 27.06	–31 12 22.65	M	12.13	01.04	151.19	2.59
SGR_P5784	19 00 13.64	–30 55 13.26	K	13.13	01.02	165.10	2.38
SGR_P5785	18 59 58.25	–31 02 27.28	K	13.29	00.88	-18.16	3.46
SGR_P5798	19 00 10.50	–30 57 15.15	K	12.63	00.92	130.31	3.62
SGR_P5814	18 59 38.57	–31 10 08.24	M	11.88	01.07	134.64	2.11
SGR_P5825	18 59 55.64	–31 04 30.12	K	12.21	01.07	153.77	1.44
SGR_P5832	18 58 09.98	–31 29 04.93	M	12.86	00.92	-9.21	161.91
SGR_P5848	18 59 59.08	–31 03 55.81	K	13.11	00.94	134.42	4.60
SGR_P5859	19 00 06.02	–31 01 24.54	K	13.38	00.94	140.58	3.26
SGR_P5876	18 58 35.55	–31 25 43.85	K	12.61	01.01	128.46	0.94
SGR_P5888	18 59 00.17	–31 21 13.02	K	13.78	00.87	158.64	2.46
SGR_P5890	18 59 38.96	–31 11 34.80	K	12.02	00.98	145.48	0.78
SGR_P5906	18 59 45.19	–31 09 59.38	K	12.81	00.94	161.18	2.40
SGR_P5907	18 58 52.79	–31 23 04.07	K	12.94	01.01	135.97	1.66
SGR_P5926	18 58 31.60	–31 27 11.79	K	13.73	00.86	145.75	2.72
SGR_P5932	18 58 38.00	–31 26 12.67	K	13.22	00.97	156.65	1.88
SGR_P5950	18 58 21.56	–31 29 07.92	K	12.47	00.96	153.80	2.63
SGR_P5952	19 00 22.94	–30 55 51.05	K	12.88	00.96	150.04	2.14

Continued on next page

Table A.1 – continued from previous page

ID	RA	Dec	Spectral Type	2MASS K	2MASS $(J-K)$	v_{rad} (km s^{-1})	σ_{rv} (km s^{-1})
SGR_P5962	18 59 56.49	–31 07 30.14	M	13.68	01.00	187.63	152.67
SGR_P5964	18 59 49.01	–31 10 01.72	M	10.26	01.25	141.86	6.74
SGR_P5968	18 58 45.90	–31 25 15.19	M	12.27	01.03	147.26	2.96
SGR_P5970	19 00 22.24	–30 56 34.08	M	12.27	01.06	151.36	2.44
SGR_P5976	18 59 05.52	–31 21 33.54	K	13.77	00.83	146.12	2.21
SGR_P5998	18 59 16.97	–31 19 26.51	M	12.07	01.03	131.18	1.09
SGR_P6010	19 00 19.62	–30 59 17.96	M	10.80	01.15	132.19	3.10
SGR_P6018	18 58 56.46	–31 24 05.85	M	13.00	00.92	142.74	141.15
SGR_P6032	19 00 16.96	–31 01 08.99	M	13.47	00.91	-10.78	4.71
SGR_P6037	18 49 23.09	–30 13 53.43	K	13.27	00.91	54.06	107.13
SGR_P6042	18 59 00.38	–31 23 51.90	K	13.13	00.95	156.32	2.60
SGR_P6052	18 59 07.97	–31 22 37.98	M	13.53	00.90	152.90	129.82
SGR_P6054	18 59 17.24	–31 20 41.01	M	09.76	01.30	105.25	134.93
SGR_P6059	18 58 59.82	–31 24 36.41	M	13.21	00.88	79.65	114.46
SGR_P6062	18 58 23.89	–31 30 46.65	M	13.50	00.94	-22.31	4.01
SGR_P6065	19 00 01.62	–31 08 42.06	M	11.02	01.23	131.75	3.34
SGR_P6067	18 59 20.69	–31 20 15.03	K	12.73	00.93	145.78	3.98
SGR_P6091	18 49 21.68	–30 10 31.15	K	13.74	00.83	-5.57	135.28
SGR_P6094	18 58 13.31	–31 32 53.53	M	13.28	00.88	72.58	134.34
SGR_P6099	18 59 54.06	–31 12 15.00	K	12.34	00.96	142.18	0.70
SGR_P6104	19 00 17.66	–31 03 52.00	K	13.46	00.95	130.08	4.77
SGR_P6106	18 59 15.39	–31 22 22.58	K	12.80	01.04	139.80	2.36
SGR_P6114	18 58 26.76	–31 31 15.50	K	12.77	00.97	140.81	3.21
SGR_P6118	18 59 10.03	–31 23 40.36	K	13.59	00.89	-83.33	6.62

Continued on next page

Table A.1 – continued from previous page

ID	RA	Dec	Spectral Type	2MASS K	2MASS $(J-K)$	v_{rad} (km s^{-1})	σ_{rv} (km s^{-1})
SGR_P6135	18 59 00.98	–31 25 48.89	M	11.39	01.13	155.26	2.27
SGR_P6139	18 58 56.00	–31 26 46.87	K	13.60	00.88	136.80	2.47
SGR_P6152	18 49 11.73	–30 17 06.91	K	11.15	01.05	147.57	2.18
SGR_P6161	18 59 11.03	–31 24 08.86	K	12.51	00.99	182.61	1.28
SGR_P6165	19 00 21.55	–31 03 48.53	K	13.51	00.95	131.94	1.88
SGR_P6177	18 58 55.22	–31 27 37.02	K	13.80	00.83	-11.27	3.80
SGR_P6179	18 49 12.54	–30 13 56.83	K	13.21	00.89	-2.58	111.78
SGR_P6180	19 00 16.11	–31 06 33.80	M	11.16	01.16	148.59	3.02
SGR_P6196	18 49 13.91	–30 11 31.95	K	12.02	01.05	136.02	5.62
SGR_P6199	19 00 16.48	–31 06 54.78	K	13.73	00.85	20.97	5.71
SGR_P6204	18 58 31.90	–31 31 52.18	M	13.30	00.93	148.05	115.92
SGR_P6210	18 58 43.84	–31 30 02.79	K	13.60	00.83	-65.33	5.86
SGR_P6214	18 58 30.54	–31 32 10.37	K	12.15	01.00	109.28	2.72
SGR_P6225	19 00 09.86	–31 09 53.23	K	12.83	00.91	138.25	0.89
SGR_P6226	18 58 28.86	–31 32 39.46	K	12.94	00.93	162.26	1.83
SGR_P6227	18 49 04.90	–30 20 46.41	K	13.58	00.89	12.08	123.80
SGR_P6234	18 49 15.23	–30 08 36.25	M	09.55	01.20	-46.98	3.75
SGR_P6237	18 49 16.82	–30 07 19.45	K	13.39	00.86	79.97	126.47
SGR_P6243	18 58 50.19	–31 29 31.13	K	13.18	00.96	-59.39	3.53
SGR_P6251	18 49 13.31	–30 09 32.23	M	11.38	01.19	118.42	3.57
SGR_P6259	18 49 06.19	–30 16 00.05	K	12.86	01.00	158.37	2.62
SGR_P6264	19 00 29.45	–31 03 13.55	M	09.94	01.25	65.72	123.72
SGR_P6275	18 58 46.23	–31 30 42.18	M	10.57	01.13	122.50	2.65
SGR_P6289	18 49 11.03	–30 09 20.57	K	13.31	00.99	7.93	5.17

Continued on next page

Table A.1 – continued from previous page

ID	RA	Dec	Spectral Type	2MASS K	2MASS $(J-K)$	v_{rad} (km s^{-1})	σ_{rv} (km s^{-1})
SGR_P6299	18 49 04.96	–30 14 35.60	M	11.48	01.14	148.28	3.23
SGR_P6300	18 49 08.68	–30 10 50.08	K	13.72	00.86	-0.47	123.14
SGR_P6305	18 58 59.22	–31 28 54.12	K	12.51	01.04	155.98	2.29
SGR_P6314	18 49 03.03	–30 16 07.83	K	13.22	00.86	52.42	138.70
SGR_P6322	18 49 08.32	–30 10 11.20	K	11.35	01.07	158.78	3.44
SGR_P6338	18 49 11.15	–30 06 53.18	K	12.39	01.08	99.30	129.62
SGR_P6355	19 00 18.13	–31 10 13.21	M	11.02	01.13	105.28	2.60
SGR_P6398	18 49 05.60	–30 08 39.71	M	10.64	01.21	130.04	2.58
SGR_P6456	18 59 00.96	–31 31 10.96	K	13.52	00.90	156.57	2.93
SGR_P6480	18 59 12.47	–31 29 29.12	K	12.94	00.95	149.54	3.04
SGR_P6491	18 48 58.80	–30 09 12.98	M	13.79	00.94	204.61	174.22
SGR_P6536	18 49 01.49	–30 04 13.69	M	13.53	00.94	146.83	90.81
SGR_P6563	18 49 00.19	–30 03 44.97	K	11.66	01.10	-1.08	123.54
SGR_P6571	18 48 46.68	–30 15 08.60	K	12.16	01.03	145.88	1.25
SGR_P6587	18 48 44.83	–30 16 39.25	M	13.41	00.88	16.01	136.59
SGR_P6600	18 48 51.54	–30 08 31.48	M	11.02	01.18	146.70	2.16
SGR_P6613	18 48 43.37	–30 16 17.50	K	13.67	00.91	141.15	3.39
SGR_P6615	18 48 40.25	–30 20 49.63	K	13.51	00.87	-40.84	125.49
SGR_P6616	18 48 45.49	–30 13 12.07	K	12.80	00.96	162.42	1.17
SGR_P6623	18 48 40.31	–30 20 15.01	K	13.77	00.86	10.57	5.82
SGR_P6646	18 48 37.49	–30 23 10.07	M	09.85	01.17	46.24	3.69
SGR_P6697	18 48 49.60	–30 04 30.54	K	13.12	00.87	28.82	96.82
SGR_P6726	18 48 48.41	–30 04 18.89	K	13.59	00.93	36.07	120.98
SGR_P6730	18 48 44.69	–30 06 57.39	M	11.64	01.14	158.07	3.30

Continued on next page

Table A.1 – continued from previous page

ID	RA	Dec	Spectral Type	2MASS K	2MASS $(J-K)$	v_{rad} (km s^{-1})	σ_{rv} (km s^{-1})
SGR_P6741	18 48 33.58	–30 18 10.06	M	13.57	00.87	240.80	2.33
SGR_P6750	18 48 37.20	–30 12 44.86	K	12.88	00.94	147.52	1.91
SGR_P6767	18 48 44.41	–30 05 32.41	M	13.77	00.81	209.32	119.56
SGR_P6820	18 48 33.55	–30 12 27.97	K	13.28	00.97	144.08	0.89
SGR_P6826	18 48 45.88	–30 02 02.90	K	13.77	00.86	82.29	155.50
SGR_P6853	18 48 44.38	–30 02 07.06	K	11.97	01.10	-71.37	125.09
SGR_P6859	18 48 29.69	–30 14 25.58	K	13.60	00.85	143.19	1.88
SGR_P6869	18 48 27.33	–30 16 39.18	K	13.24	00.86	156.54	2.37
SGR_P6894	18 48 32.44	–30 08 49.43	K	13.19	00.95	150.95	1.82
SGR_P6898	18 48 22.31	–30 21 45.42	K	13.26	01.01	21.98	81.88
SGR_P6919	18 48 24.61	–30 16 10.55	M	10.90	01.24	135.48	2.90
SGR_P7007	18 48 16.10	–30 21 03.81	M	11.49	01.12	148.67	3.96
SGR_P7013	18 48 32.93	–30 02 40.78	K	13.60	00.85	45.32	101.69
SGR_P7025	18 48 18.96	–30 14 38.27	M	11.99	01.08	-43.19	1.47
SGR_P7085	18 48 13.12	–30 20 15.38	K	13.70	00.85	-0.34	137.34
SGR_P7097	18 48 23.67	–30 07 04.77	K	13.78	00.84	-4.75	120.88
SGR_P7099	18 48 13.31	–30 18 54.50	M	10.35	01.26	136.16	131.09
SGR_P7118	18 48 18.69	–30 10 15.22	K	13.60	00.88	147.73	2.48
SGR_P7132	18 48 12.08	–30 17 37.29	K	13.04	01.00	148.30	3.13
SGR_P7183	18 48 19.46	–30 06 17.11	M	13.28	00.86	70.96	143.76
SGR_P7193	18 48 07.98	–30 17 59.86	K	13.12	00.92	106.28	98.82
SGR_P7236	18 48 08.54	–30 13 48.75	M	13.54	00.94	46.56	88.62
SGR_P7288	18 48 16.10	–30 03 39.27	K	12.71	00.99	4.39	4.73
SGR_P7294	18 48 13.47	–30 05 24.87	M	13.72	00.81	136.38	126.74

Continued on next page

Table A.1 – continued from previous page

ID	RA	Dec	Spectral Type	2MASS K	2MASS $(J-K)$	v_{rad} (km s^{-1})	σ_{rv} (km s^{-1})
SGR_P7353	18 48 01.39	–30 14 12.25	K	12.69	00.92	134.70	3.79
SGR_P7364	18 48 07.50	–30 07 08.12	K	12.60	00.92	19.03	116.43
SGR_P7368	18 48 01.67	–30 12 43.76	M	11.99	01.06	135.41	2.23
SGR_P7374	18 48 01.89	–30 12 00.25	K	13.03	00.96	34.98	132.94
SGR_P7375	18 47 56.39	–30 20 02.82	M	13.60	00.83	74.95	146.79
SGR_P7390	18 48 08.21	–30 05 04.16	K	13.02	00.88	39.66	129.40
SGR_P7480	18 47 55.13	–30 13 22.94	M	13.34	00.91	78.65	134.54
SGR_P7508	18 47 52.66	–30 14 27.73	K	12.68	01.00	149.33	5.44
SGR_P7516	18 47 50.41	–30 16 54.99	M	12.64	00.95	64.21	125.06
SGR_P7535	18 47 52.07	–30 13 00.21	M	10.79	01.22	142.23	4.74
SGR_P7552	18 47 50.62	–30 13 22.84	K	12.07	00.96	12.93	109.84
SGR_P7562	18 47 54.57	–30 08 26.79	M	11.24	01.19	112.32	156.52
SGR_P7580	18 47 47.37	–30 15 25.46	M	11.32	01.17	135.16	4.16
SGR_P7586	18 47 56.62	–30 05 13.13	K	13.64	00.87	1.48	129.28
SGR_P7590	18 47 44.56	–30 19 00.51	M	11.21	01.08	66.55	110.36
SGR_P7644	18 47 47.53	–30 11 10.66	K	12.35	00.95	78.78	129.59
SGR_P7729	18 47 38.59	–30 16 28.97	M	13.23	00.87	44.87	118.78
SGR_P7753	18 47 42.30	–30 10 18.42	M	10.55	01.19	118.34	135.87
SGR_P7759	18 47 44.97	–30 07 21.61	K	13.39	00.87	18.36	139.00
SGR_P7851	18 47 33.57	–30 14 01.62	K	12.07	01.01	-27.35	115.87

A.2 SAAO Data

Table A.2: A Complete Table of all the SAAO Data

ID	RA	Dec	Spectral Type	2MASS K	2MASS $(J-K)$
SAAO-1	18 55 25.52	–30 26 12.80	M	09.72	01.33
SAAO-2	18 54 09.02	–30 23 20.20	M	09.28	01.29
SAAO-3	18 55 39.57	–30 16 32.50	M	10.12	01.16
SAAO-4	18 54 29.72	–30 11 21.90	M	09.73	01.28
SAAO-5	18 55 43.72	–30 12 26.30	M	09.91	01.24
SAAO-6	18 55 48.83	–30 42 27.30	M	09.95	01.17
SAAO-7	18 55 41.22	–30 11 31.00	M	10.29	01.11
SAAO-8	18 53 59.53	–29 58 57.40	C	09.26	01.52
SAAO-9	18 56 55.99	–30 08 10.50	C	09.72	01.23
SAAO-10	18 52 39.24	–30 09 16.30	M	09.55	01.26
SAAO-11	18 52 54.39	–30 00 20.60	M	09.70	01.31
SAAO-12	18 57 46.10	–30 06 54.40	K	09.52	01.33
SAAO-13	18 52 50.30	–29 56 31.70	C	09.45	01.69
SAAO-14	18 52 53.41	–29 53 06.10	M	09.85	01.29
SAAO-15	18 51 27.09	–30 24 52.20	M	09.66	01.29
SAAO-16	18 56 16.03	–29 42 47.20	M	09.85	01.28
SAAO-17	18 57 20.38	–31 04 48.20	M	09.85	01.24
SAAO-18	18 55 56.74	–29 39 07.40	M	09.87	01.21
SAAO-19	18 53 57.29	–31 17 42.10	K	09.63	01.25
SAAO-20	18 54 16.55	–29 36 34.60	M	09.93	01.20
SAAO-21	18 50 52.42	–30 30 59.30	M	09.64	01.30
SAAO-22	18 51 28.17	–29 59 18.30	M	10.28	01.22
SAAO-23	18 54 34.26	–31 21 22.00	M	09.63	01.22

Continued on next page

Table A.2 – continued from previous page

ID	RA	Dec	Spectral Type	2MASS K	$(J-K)$
SAAO-24	18 51 53.56	–29 48 24.60	M	10.80	01.23
SAAO-25	18 55 20.15	–29 30 25.30	M	09.61	01.33
SAAO-26	18 51 17.05	–31 01 39.00	M	09.98	01.16
SAAO-27	18 51 08.22	–29 54 15.80	M	10.72	01.18
SAAO-28	18 59 41.04	–30 28 32.20	K	09.94	01.18
SAAO-29	18 51 32.69	–29 45 18.80	C	10.67	01.32
SAAO-30	18 51 37.01	–29 40 07.80	C	10.65	01.21
SAAO-31	18 50 09.23	–30 45 36.50	C	09.69	01.32
SAAO-32	18 51 47.73	–29 35 54.10	K	10.71	01.23
SAAO-33	19 00 11.36	–30 20 04.50	K	09.74	01.30
SAAO-34	18 58 36.40	–31 20 23.00	C	10.04	01.33
SAAO-35	19 00 28.37	–30 37 27.00	M	09.78	01.29
SAAO-36	18 58 40.12	–31 22 23.10	K	10.58	01.20
SAAO-37	18 50 03.66	–29 53 04.80	M	10.27	01.26
SAAO-38	18 50 43.85	–29 36 44.00	K	09.89	01.35
SAAO-39	18 51 44.46	–29 25 11.30	K	09.59	01.31
SAAO-40	18 59 17.24	–31 20 41.00	M	09.76	01.30
SAAO-41	18 57 23.10	–31 38 26.40	K	09.95	01.17
SAAO-42	18 48 57.66	–30 30 05.50	M	09.79	01.32
SAAO-43	18 58 24.53	–31 31 59.60	M	10.84	01.18
SAAO-44	18 50 03.70	–29 42 52.40	K	10.36	01.18
SAAO-45	18 58 46.23	–31 30 42.20	K	10.57	01.13
SAAO-46	18 59 02.11	–31 30 32.50	M	09.78	01.29
SAAO-47	18 49 07.55	–29 56 11.60	M	09.85	01.32

Continued on next page

Table A.2 – continued from previous page

ID	RA	Dec	Spectral Type	2MASS K	2MASS $(J-K)$
SAAO-48	18 59 27.54	–31 26 18.50	M	10.83	01.21
SAAO-49	18 48 37.49	–30 23 10.10	M	09.85	01.17
SAAO-50	18 56 11.24	–29 03 54.90	C	06.31	01.92
SAAO-51	18 55 28.11	–29 00 55.00	M	09.62	01.34
SAAO-52	18 48 15.80	–30 07 19.80	M	09.65	01.28
SAAO-53	18 56 14.22	–31 56 06.30	M	09.96	01.20
SAAO-54	19 01 26.53	–31 03 27.70	M	09.69	01.29
SAAO-55	18 49 33.56	–29 25 54.90	K	10.77	01.26
SAAO-56	18 57 48.77	–31 57 11.60	M	10.79	01.18
SAAO-57	18 59 31.95	–31 44 44.60	M	10.72	01.16
SAAO-58	18 48 54.60	–29 30 15.90	K	10.56	01.14
SAAO-59	18 50 25.76	–31 47 16.20	M	09.88	01.20
SAAO-60	19 01 06.10	–31 29 33.60	M	09.70	01.27
SAAO-61	18 48 39.78	–31 32 58.10	K	09.74	01.31
SAAO-62	18 59 50.54	–31 51 22.30	M	10.50	01.18
SAAO-63	18 48 57.20	–29 18 33.80	M	09.79	01.23
SAAO-64	18 48 06.18	–29 19 02.00	K	10.55	01.24
SAAO-65	18 55 20.80	–30 25 11.10	M	10.17	01.21
SAAO-66	18 54 52.61	–30 20 55.50	C	09.44	01.88
SAAO-67	18 54 24.29	–30 25 10.50	C	09.74	01.76
SAAO-68	18 54 41.63	–30 20 36.00	M	10.14	01.19
SAAO-69	18 55 16.66	–30 36 18.60	M	10.03	01.26
SAAO-70	18 54 10.97	–30 23 19.20	M	09.60	01.13
SAAO-71	18 54 29.74	–30 37 47.10	M	09.83	01.11

Continued on next page

Table A.2 – continued from previous page

ID	RA	Dec	Spectral Type	2MASS K	2MASS $(J-K)$
SAAO-72	18 54 56.18	–30 14 08.00	M	10.54	01.22
SAAO-73	18 54 07.14	–30 39 19.50	M	10.59	01.17
SAAO-74	18 53 14.05	–30 19 13.90	M	10.10	01.20
SAAO-75	18 53 15.68	–30 17 57.20	M	10.05	01.28
SAAO-76	18 53 18.11	–30 13 43.60	M	10.39	01.17
SAAO-77	18 55 38.97	–29 55 56.80	C	09.80	02.75
SAAO-78	18 54 39.18	–29 54 18.20	C	10.51	01.39
SAAO-79	18 57 51.58	–30 32 00.00	M	09.89	01.31
SAAO-80	18 52 10.77	–30 40 23.00	M	09.44	01.11
SAAO-81	18 57 57.48	–30 10 08.50	C	09.76	02.75
SAAO-82	18 51 41.05	–30 03 37.70	C	09.43	02.67
SAAO-83	18 55 43.28	–29 37 09.50	M	10.22	01.28
SAAO-84	18 53 29.37	–29 38 24.10	C	09.72	01.65

Appendix B

Data Reduction of the SAAO Data

In this appendix the commands used during the data reduction of the SAAO data using IRAF will be displayed.

B.1 Setting Up IRAF

To begin using IRAF an IRAF directory must be set up.

```
> mkiraf
    :xgterm
```

This creates a new login.cl file, which is edited to include the packages needed to open in IRAF.

```
> emacs login.cl
> set stdimage = imt4096
> set imtype = ‘‘fits’’
    noao
    imred
    ccdred
```

```
twodspec
longslit
!ds9 &
```

Once this is saved, a terminal is opened up to work from.

```
> xgterm &
> cl
```

To exit IRAF type `logout`

B.2 Data Reduction

The data is prepared by creating a list containing all of it.

```
> ls a*.fits > all.lst
```

B.2.1 Overscan Region

A new list is made, of the same data but renamed xxxo.fits, to signify overscan.

```
> emacs all.lst &
```

Go to, `Edit`, `Search`, `Replace`

`replace: .fits`, `with: o.fits`

Ensure you are the top of the list, SHIFT-1 replaces for all files.

`Save Buffer As` allo.lst

The location of the overscan region needs to be determined.

```
> imhead xxx.fits
```

```
    biassec '[4:21, 1:133]'
```

Then the overscan correction can be run.

```
> epar ccdproc
    images = all.lst
    output = allo.lst
    ccdtype =
    fixpix = no
    oversca = yes
    scancor = no
```

Everything else is set to no, as all that is run is the overscan correction.

```
    biassec = [4:21, 1:133]
    interac = yes
    low_rej = 1.
    high_rej = 1.
:wq
:go
```

The fit is run interactively to check the first, if it's ok `:q` to quit, if not the order and/or the function can be changed `:order = 2`, `:fun = chebyshev`, type `:f` to fit. If the fit is ok type `NO` to skip the rest of the interactive fitting.

B.2.2 Bias Subtraction

A list of all bias files is created and saved as bias.lst.

Then a master bias must be created.

```
> epar zerocomb
    input = @bias.lst
    output = Zero
    reject = avsigclip
:go
```

A list of all the images from which the bias is to be subtracted from is created.

`> emacs allo.lst &`

Delete the bias images.

`Edit`, `Search`, `Replace`

`replace: .fits`, `with: b.fits`

Save as allob.lst.

Next the bias is subtracted from our images.

```
> epar ccdproc
    images = allbias.lst
    output = @allob.lst
    zercor = yes
```

Again, all others set to no.

```
    zero = Zero
:go
```

B.2.3 Flat Field

As mentioned in the text, this step was not completed with our images. However, the following steps should be followed to do flat field correction.

A list of all the flat field images is created and saved as domeflats.lst.

```
> epar flatcombine
    input = domeflats.lst
    output = DomeFlat
    combine = average
    reject = avsigslip
    ccdtype = flat
    scale = mode
:go
```

This has created a master flat field. Next the flat must be normalised.

```
> epar response
    calibrat = DomeFlat
    normaliz = DomeFlat
    response = nDomeFlat
    interac = yes
:go
```

Again, as we opted to fit interactively, the fit must be checked.

Once `response` has completed, check the DomeFlat image. Values should all be around 1.

Finally the flat field division must be completed. A list of all the files to be flat field corrected is made and saved as flats.lst. A list for the output images must also be created.

`Edit`, `Search`, `Replace`

`replace: .fits`, `with: f.fits`

This is saved as allobf.lst.

```
> epar ccdproc
    images = flats.lst
    output = allobf.lst
    flatcor = yes
    flat = nDomeFlat
:go
```

B.2.4 Bad Pixel Removal

`> emacs allob.lst &`

`Edit`, `Search`, `Replace`

`replace: .fits`, `with: p.fits`

Saved as allobp.fits.

A flat image is used to locate the bad columns, x1 x2 y1 y2, and then a list of all these bad columns to be removed is created and saved as fixpix.lst.

```
> epar ccdproc
    images = allob.lst
    output = allobp.lst
    fixpix = yes
    fixfile = fixpix.lst
:go
```

B.2.5 Trimming The Images

`> emacs allobp.lst &`

`Edit`, `Search`, `Replace`

`replace: .fits`, `with: t.fits`

Saved as allobpt.fits.

The pixels to trim are checked.

```
> display xxxobp.fits
```

```
> epar ccdproc
    images = allobp.lst
    output = allobpt.lst
    trim = yes
    trimsec = [4:1795,3:130]
:go
```

B.2.6 Cosmic Rays

The programme for removing cosmic rays must be downloaded off the internet. Google 'LA Cosmic' and download the spectroscopic version.

```
> emacs lacos_spec.cl &
```

The programme is copied and pasted into an emacs file. Edit,

```
    outmask = mktemp(''lacos'')
```

And saved as lacos_spec.cl.

```
> task lacos_spec = lacos_spec.cl
> epar lacos_spec
    input = xxxobpt.fits
    output = xxxobtpc.fits
    gain = 2.
    readn = 6.
    sigclip = 4.5
```

```
    sigfrac = 0.5
    objlim = 1.
    niter = 4
:go
```

A new file xxxobptc.fits is created, and is checked to ensure the cosmic rays have been removed.

In terminal,

```
> gaia xxxobptc.fits &
```

Repeat for all object images.

B.2.7 Wavelength Calibration

The correct line list on the internet is found and saved as CuNe1.dat.

The full width half maximum value (gfwhm) needs to be identified.

```
> splot xxxobpt.fits
    line ():  yes
```

Type `a` and `a` either side of the peak to zoom in and then `d` and `d` either side to fit function. Type `g` to choose a Gaussion function, move to the peak and type `g` again.

`q` (to quit)

`s` (single)

`s`

And now the gfwhm value can be checked.

The first task in wavelength calibration is to identify the known lines of the arc lamp spectrum.

```
> epar identify
    images = arc.fits (e.g.  a2630007obpt.fits)
    database = object name (eg.  12680)
    coordli = CuNe1.dat
    fwidth = 2 (the gfwhm value)
:go
```

`m` on the line and type in wavelength

Repeat for all lines

`f`

Check fit values are small (0.2 – 0.5), change order or function if necessary

`q`, now see the same plot but in units of wavelength

`l` identifies any other lines

`f` to check the values again

`q` to quit

`:yes` to save the image

```
> epar reidentify
    reference = arc.fits
    images = arc.fits
    coordlist = CuNe1.dat
    database = object name
    answer = NO
:go
```

```
> epar fitcoords
    images = arc (e.g.  a2360007obpt)
    fitname = arc
    database = object name
```

```
:go
```

The fit is checked and points that are outliers are deleted; type `d p`

`f` to fit,

Plot different residuals `x x y r`, `x y y r` or `x x y y`

```
f
q
:yes
> epar transform
    input = arc.fits
    output = arc w (eg.  a26300007obptw)
    fitnames = arcarc
    database = object name
    interptype = spline3
:go

> epar transform
    input = object.fits
    output = object w
    filenames = arcarc
    database = object name
    interptype = spline3
:go
```

B.2.8 Background Subtraction

The object image is opened within Gaia and checked to see where the flat background is. The y co-ordinates are written in a list, with any bright areas e.g. the stellar spectrum, omitted. For example, [1:46,75:96,105:128].

```
> epar background
    input = xxxobptcw.fits
    output = xxxobptcwg.fits
:wq
```

The background sample needs to be changed but as the coordinates are a long list it is done outside the task window.

```
> background sample = ‘‘1:46,75:96,105:128’’
```

Check the fit and again, change order if neccessary

```
:order 2
f
q
```

If there are peaks or troughs which lie outside the omitted regions the background subtraction must be re-run with edited background sample values. First the background subtracted image must be deleted.

(In terminal)

```
> rm -f xxx*g.fits
```

The IRAF reductions are now complete.

```
> logout
```

References

T. B. Ake. A revised spectral classification system in the red for S stars. *ApJ*, 234: 538–547, December 1979.

B. Aringer, L. Girardi, W. Nowotny, P. Marigo, and M. T. Lederer. Synthetic photometry for carbon rich giants. I. Hydrostatic dust-free models. *A&A*, 503:913–928, September 2009.

N. Baker and R. Kippenhahn. The Pulsations of Models of Delta Cephei Stars. II. *ApJ*, 142:868–+, October 1965.

S. A. Becker and I. Iben, Jr. The asymptotic giant branch evolution of intermediate-mass stars as a function of mass and composition. II - Through the first major thermal pulse and the consequences of convective dredge-up. *ApJ*, 237:111–129, April 1980.

M. Bellazzini, F. R. Ferraro, and R. Buonanno. The Sagittarius Dwarf Galaxy Survey (SDGS) - I. Colour-magnitude diagrams, reddening and population gradients. First evidence of a very metal-poor population. *MNRAS*, 304:633–653, April 1999a.

M. Bellazzini, F. R. Ferraro, and R. Buonanno. The Sagittarius Dwarf Galaxy Survey (SDGS) - II. The stellar content and constraints on the star formation history. *MNRAS*, 307:619–636, August 1999b.

T. Blöcker. Structure and Evolution of AGB Stars. In T. Le Bertre, A. Lebre, & C. Waelkens, editor, *Asymptotic Giant Branch Stars*, volume 191 of *IAU Symposium*, pages 21–+, 1999.

P. Bonifacio, L. Sbordone, G. Marconi, L. Pasquini, and V. Hill. The Sgr dSph hosts a metal-rich population. *A&A*, 414:503–514, February 2004.

A. I. Boothroyd, I.-J. Sackmann, and G. J. Wasserburg. Hot bottom burning in asymptotic giant branch stars and its effect on oxygen isotopic abundances. *ApJL*, 442: L21–L24, March 1995.

G. H. Bowen and L. A. Willson. From wind to superwind - The evolution of mass-loss rates for Mira models. *ApJL*, 375:L53–L56, July 1991.

M. L. Boyer, I. McDonald, J. T. van Loon, K. D. Gordon, B. Babler, M. Block, S. Bracker, C. Engelbracht, J. Hora, R. Indebetouw, M. Meade, M. Meixner, K. Misselt, J. M. Oliveira, M. Sewilo, B. Shiao, and B. Whitney. Dust Production and Mass Loss in the Galactic Globular Cluster NGC 362. *ApJ*, 705:746–757, November 2009.

M. L. Boyer, S. Srinivasan, J. T. van Loon, I. McDonald, M. Meixner, D. Zaritsky, K. D. Gordon, F. Kemper, B. Babler, M. Block, S. Bracker, C. W. Engelbracht, J. Hora, R. Indebetouw, M. Meade, K. Misselt, T. Robitaille, M. Sewilo, B. Shiao, and B. Whitney. Surveying the Agents of Galaxy Evolution in the Tidally-Stripped, Low Metallicity Small Magellanic Cloud (SAGE-SMC) II. Cool Evolved Stars. *AJ*, 142:103, October 2011.

P. Cariulo, S. Degl'Innocenti, and V. Castellani. Calibrated stellar models for metal-poor populations. *A&A*, 421:1121–1130, July 2004.

J. M. Carpenter. Color Transformations for the 2MASS Second Incremental Data Release. *AJ*, 121:2851–2871, May 2001.

V. Castellani, S. Degl'Innocenti, M. Marconi, P. G. Prada Moroni, and P. Sestito. Stellar evolutionary models for Magellanic Clouds. *A&A*, 404:645–653, June 2003.

L. Cerrigone, J. L. Hora, G. Umana, and C. Trigilio. Investigating the formation of planetary nebulae. In M. J. Barlow & R. H. Méndez, editor, *Planetary Nebulae in our Galaxy and Beyond*, volume 234 of *IAU Symposium*, pages 377–378, 2006.

M.-Y. Chou, S. R. Majewski, K. Cunha, V. V. Smith, R. J. Patterson, D. Martínez-Delgado, D. R. Law, J. D. Crane, R. R. Muñoz, R. Garcia López, D. Geisler, and M. F. Skrutskie. A 2MASS All-Sky View of the Sagittarius Dwarf Galaxy. V. Variation of the Metallicity Distribution Function along the Sagittarius Stream. *ApJ*, 670: 346–362, November 2007.

M.-R. L. Cioni and H. J. Habing. AGB stars in the Magellanic Clouds. I. The C/M ratio. *A&A*, 402:133–140, April 2003.

P. Cote, D. A. Hanes, D. E. McLaughlin, T. J. Bridges, J. E. Hesser, and G. L. H. Harris. Discovery of a Probable CH Star in the Globular Cluster M14 and Implications for the Evolution of Binaries in Clusters. *ApJL*, 476:L15+, February 1997.

L. Decin, I. Cherchneff, S. Hony, S. Dehaes, C. De Breuck, and K. M. Menten. Detection of "parent" molecules from the inner wind of AGB stars as tracers of nonequilibrium chemistry. *A&A*, 480:431–438, March 2008.

A. Dotter, B. Chaboyer, D. Jevremović, E. Baron, J. W. Ferguson, A. Sarajedini, and J. Anderson. The ACS Survey of Galactic Globular Clusters. II. Stellar Evolution Tracks, Isochrones, Luminosity Functions, and Synthetic Horizontal-Branch Models. *AJ*, 134:376–390, July 2007.

A. Dotter, B. Chaboyer, D. Jevremović, V. Kostov, E. Baron, and J. W. Ferguson. The Dartmouth Stellar Evolution Database. *ApJS*, 178:89–101, September 2008.

A. S. Eddington. The pulsation theory of Cepheid variables. *The Observatory*, 40: 290–293, August 1917.

D. Engels, A. Winnberg, J. Brand, and C. M. Walmsley. Variability of 22 GHz H_2O masers in circumstellar shells. In T. Le Bertre, A. Lebre, & C. Waelkens, editor, *Asymptotic Giant Branch Stars*, volume 191 of *IAU Symposium*, page 373, 1999.

M. Feast. AGB variables as distance indicators. In D. W. Kurtz & K. R. Pollard, editor, *IAU Colloq. 193: Variable Stars in the Local Group*, volume 310 of *Astronomical Society of the Pacific Conference Series*, pages 304–+, May 2004.

M. Feast and P. Whitelock. Can Mira Variables Tell us the Chemical Abundances in Stellar Systems? In F. Matteucci & F. Giovannelli, editor, *The Evolution of the Milky Way: Stars versus Clusters*, pages 229–+, 2000.

M. W. Feast, I. S. Glass, P. A. Whitelock, and R. M. Catchpole. A period-luminosity-colour relation for Mira variables. *MNRAS*, 241:375–392, November 1989.

P. García-Lario. Properties of Post-AGB Stars. In M. J. Barlow & R. H. Méndez, editor, *Planetary Nebulae in our Galaxy and Beyond*, volume 234 of *IAU Symposium*, pages 63–70, 2006.

P. García-Lario, F. D'Antona, J. Lub, B. Plez, and H. J. Habing. Lithium and s-process enrichment in massive galactic AGB stars. In T. Le Bertre, A. Lebre, & C. Waelkens, editor, *Asymptotic Giant Branch Stars*, volume 191 of *IAU Symposium*, page 91, 1999.

R. C. Gilman. On the Coupling of Grains to the Gas in Circumstellar Envelopes. *ApJ*, 178:423–426, December 1972.

K. K. Gilroy. Carbon isotope ratios and lithium abundances in open cluster giants. *ApJ*, 347:835–848, December 1989.

G. Giuffrida, L. Sbordone, S. Zaggia, G. Marconi, P. Bonifacio, C. Izzo, T. Szeifert, and R. Buonanno. A wide angle view of the Sagittarius dwarf spheroidal galaxy.

I. VIMOS photometry and radial velocities across Sgr dSph major and minor axis. *A&A*, 513:A62+, April 2010.

K. D. Gordon, M. Meixner, M. Meade, B. A. Whitney, C. W. Engelbracht, C. Bot, M. L Boyer, B. Lawton, M. Sewilo, M. B. L. Babler, J.-P. Bernard, S. Bracker, M. Block, R. D. Blum, A. D. Bolatto, A. Z. Bonanos, J. Harris, J. L. Hora, R. Indebetouw, K. A. Misselt, W. T. Reach, B. Shiao, A. Tielens, L. R. Carlson, E. B. Churchwell, G. C. Clayton, C. R. Chen, M. Cohen, J. L. Fukui, V. Gorjian, S. Hony, F. Israel, A. Kawamura, F. Kemper, A. K. Leroy, A. Li, S. C. Madden, A. R. Marble, I. McDonald, A. Mizuno, N. Mizuno, E. Muller, J. M. Oliveira, K. A. G. Olsen, T. Onishi, R. Paladini, D. Paradis, S. Points, T. Robitaille, D. Rubin, K. Sandstrom, S Sato, H. Shibai, J. D. Simon, L. J Smith, S. Srinivasan, U. P. Vijh, S. D. Van Dyk, J. Theodorus van Loon, and D. F. Zaritsky. Surveying the Agents of Galaxy Evolution in the Tidally-Stripped, Low Metallicity Small Magellanic Cloud (SAGE-SMC). I. Overview. *AJ*, 142:102, October 2011.

R. Gratton, C. Sneden, and E. Carretta. Abundance Variations Within Globular Clusters. *ARA&A*, 42:385–440, September 2004.

B. Gustafsson, R. A. Bell, K. Eriksson, and A. Nordlund. A grid of model atmospheres for metal-deficient giant stars. I. *A&A*, 42:407–432, September 1975.

B. Gustafsson, B. Edvardsson, K. Eriksson, U. G. Jørgensen, Å. Nordlund, and B. Plez. A grid of MARCS model atmospheres for late-type stars. I. Methods and general properties. *A&A*, 486:951–970, August 2008.

H. J. Habing and H. Olofsson, editors. *Asymptotic giant branch stars*, 2003. Springer.

F. Herwig. Evolution of Asymptotic Giant Branch Stars. *ARA&A*, 43:435–479, September 2005.

R. W. Hilditch, I. D. Howarth, and T. J. Harries. Forty eclipsing binaries in the Small Magellanic Cloud: fundamental parameters and Cloud distance. *MNRAS*, 357:304–324, February 2005.

M. L. Houdashelt, R. A. Bell, and A. V. Sweigart. Improved Color-Temperature Relations and Bolometric Corrections for Cool Stars. *AJ*, 119:1448–1469, March 2000.

R. A. Ibata, G. Gilmore, and M. J. Irwin. A dwarf satellite galaxy in Sagittarius. *Nature*, 370:194–196, July 1994.

R. A. Ibata, R. F. G. Wyse, G. Gilmore, M. J. Irwin, and N. B. Suntzeff. The Kinematics, Orbit, and Survival of the Sagittarius Dwarf Spheroidal Galaxy. *AJ*, 113:

634–655, February 1997.

I. Iben, Jr. Asymptotic Giant Branch Stars as Producers of Carbon and of Neutron-Rich Isotopes. In S. L. Baliunas & L. Hartmann, editor, *Cool Stars, Stellar Systems, and the Sun*, volume 193 of *Lecture Notes in Physics, Berlin Springer Verlag*, pages 309–+, 1984.

R. G. Izzard, E. Glebbeek, R. J. Stancliffe, and O. Pols. Binary Populations of Carbon-Enhanced Metal-Poor Stars. *PASA*, 26:311–313, September 2009.

R. G. Izzard and C. A. Tout. A binary origin for low-luminosity carbon stars. *MNRAS*, 350:L1–L4, May 2004.

A. P. Jones, A. G. G. M. Tielens, and D. J. Hollenbach. Grain Shattering in Shocks: The Interstellar Grain Size Distribution. *ApJ*, 469:740–+, October 1996.

A. Karakas and J. C. Lattanzio. Stellar Models and Yields of Asymptotic Giant Branch Stars. *PASA*, 24:103–117, October 2007.

A. I. Karakas. Stellar evolution from the main sequence to the post-AGB phase. In A. A. Zijlstra, F. Lykou, I. McDonald, & E. Lagadec, editor, *Asymmetric Planetary Nebulae 5 Conference*, pages 144–152. Jodrell Bank Centre for Astrophysics, 2010.

F. Kemper, P. M. Woods, V. Antoniou, J.-P. Bernard, R. D. Blum, M. L. Boyer, J. Chan, C.-H. R. Chen, M. Cohen, C. Dijkstra, C. Engelbracht, M. Galametz, F. Galliano, C. Gielen, K. D. Gordon, V. Gorjian, J. Harris, S. Hony, J. L. Hora, R. Indebetouw, O. Jones, A. Kawamura, E. Lagadec, B. Lawton, J. M. Leisenring, S. C. Madden, M. Marengo, M. Matsuura, I. McDonald, C. McGuire, M. Meixner, A. J. Mulia, B. O'Halloran, J. M. Oliveira, R. Paladini, D. Paradis, W. T. Reach, D. Rubin, K. Sandstrom, B. A. Sargent, M. Sewilo, B. Shiao, G. C. Sloan, A. K. Speck, S. Srinivasan, R. Szczerba, A. G. G. M. Tielens, E. van Aarle, S. D. Van Dyk, J. T. van Loon, H. Van Winckel, U. P. Vijh, K. Volk, B. A. Whitney, A. N. Wilkins, and A. A. Zijlstra. The SAGE-Spec Spitzer Legacy Program: The Life Cycle of Dust and Gas in the Large Magellanic Cloud. *PASP*, 122:683–700, May 2010.

F. Kerschbaum, T. Lebzelter, and L. Mekul. Bolometric corrections for cool giants based on near-infrared photometry. *A&A*, 524:A87+, December 2010.

D. Kilkenny. The SAAO 1.9-m Telescope and Grating Spectrograph. 6, July 2010.

S. Kwok, C. R. Purton, and P. M. Fitzgerald. On the origin of planetary nebulae. *ApJL*, 219:L125–L127, February 1978.

E. Lagadec and A. A. Zijlstra. The trigger of the asymptotic giant branch superwind:

the importance of carbon. *MNRAS*, 390:L59–L63, October 2008.

E. Lagadec, A. A. Zijlstra, M. Matsuura, J. W. Menzies, J. T. van Loon, and P. A. Whitelock. Dust mass-loss rates from asymptotic giant branch stars in the Fornax and Sagittarius dwarf spheroidal galaxies. *MNRAS*, 383:399–410, January 2008.

E. Lagadec, A. A. Zijlstra, G. C. Sloan, and M. Matsuura. Mass-loss from AGB stars in Local Group galaxies. In K. Sheth, A. Noriega-Crespo, J. Ingalls, & R. Paldini, editor, *The Evolving ISM in the Milky Way and Nearby Galaxies*, volume 4 of *Spitzer Science Centre Conference*, pages 1–8, January 2009a.

E. Lagadec, A. A. Zijlstra, G. C. Sloan, M. Matsuura, P. R. Wood, J. T. van Loon, G. J. Harris, J. A. D. L. Blommaert, S. Hony, M. A. T. Groenewegen, M. W. Feast, P. A. Whitelock, J. W. Menzies, and M.-R. Cioni. Spitzer spectroscopy of carbon stars in the Small Magellanic Cloud. *MNRAS*, 376:1270–1284, April 2007.

E. Lagadec, A. A. Zijlstra, G. C. Sloan, P. R. Wood, M. Matsuura, J. Bernard-Salas, J. A. D. L. Blommaert, M.-R. L. Cioni, M. W. Feast, M. A. T. Groenewegen, S. Hony, J. W. Menzies, J. T. van Loon, and P. A. Whitelock. Metal-rich carbon stars in the Sagittarius dwarf spheroidal galaxy. *MNRAS*, 396:598–608, June 2009b.

H. J. G. L. M. Lamers and J. P. Cassinelli. *Introduction to Stellar Winds*. Cambridge University Press, June 1999.

C. D. Laney. African Starlight: Astronomy in South Africa and the SAAO: Part 2. *Monthly Notes of the Astronomical Society of South Africa*, 55:110–+, 1996.

J. Lattanzio. Nucleosynthesis in AGB Stars: the Role of Dredge-Up and Hot Bottom Burning (invited review). In S. Kwok, M. Dopita, & R. Sutherland, editor, *Planetary Nebulae: Their Evolution and Role in the Universe*, volume 209 of *IAU Symposium*, pages 73–+, 2003.

J. Lattanzio and M. Forestini. Nucleosynthesis in AGB Stars. In T. Le Bertre, A. Lebre, & C. Waelkens, editor, *Asymptotic Giant Branch Stars*, volume 191 of *IAU Symposium*, pages 31–+, 1999.

J. Lattanzio, A. Karakas, S. Campbell, L. Elliott, and A. Chieffi. The Role of AGB Stars. *Mem. Soc. Astron. Italiana*, 75:322–+, 2004.

J. C. Lattanzio and P. R. Wood. Evolution, nucleosynthesis, and pulsations of agb stars. In H. J. Habing and H. Olofsson, editors, *Asymptotic Giant Branch Stars*, page 23, 2004.

A. C. Layden and A. Sarajedini. Photometry of the Globular Cluster M54 and the

Sagittarius Dwarf Galaxy: The Age-Metallicity Relation. *AJ*, 119:1760–1792, April 2000.

T. Lebzelter, K. H. Hinkle, P. R. Wood, R. R. Joyce, and F. C. Fekel. A study of bright Southern long period variables. *A&A*, 431:623–634, February 2005.

T. Lebzelter and P. R. Wood. Long period variables and mass loss in the globular clusters NGC 362 and NGC 2808. *A&A*, 529:A137+, May 2011.

J.-K. Lee, W. R. J. Rolleston, P. L. Dufton, and R. S. I. Ryans. Chemical compositions of four B-type supergiants in the SMC wing. *A&A*, 429:1025–1030, January 2005.

S. Lucatello, S. Tsangarides, T. C. Beers, E. Carretta, R. G. Gratton, and S. G. Ryan. The Binary Frequency Among Carbon-enhanced, s-Process-rich, Metal-poor Stars. *ApJ*, 625:825–832, June 2005.

P. Marigo. AGB evolution: the key rôle of the C/O ratio . *Mem. Soc. Astron. Italiana*, 79:403–+, 2008.

J. R. Marshall, J. T. van Loon, M. Matsuura, P. R. Wood, A. A. Zijlstra, and P. A. Whitelock. Asymptotic giant branch superwind speed at low metallicity. *MNRAS*, 355:1348–1360, December 2004.

N. F. Martin, R. A. Ibata, M. Bellazzini, M. J. Irwin, G. F. Lewis, and W. Dehnen. A dwarf galaxy remnant in Canis Major: the fossil of an in-plane accretion on to the Milky Way. *MNRAS*, 348:12–23, February 2004.

M. Matsuura, A. A. Zijlstra, J. T. van Loon, I. Yamamura, A. J. Markwick, P. A. Whitelock, P. M. Woods, J. R. Marshall, M. W. Feast, and L. B. F. M. Waters. Three-micron spectra of AGB stars and supergiants in nearby galaxies. *A&A*, 434: 691–706, May 2005.

L. Mattsson, R. Wahlin, S. Höfner, and K. Eriksson. Intense mass loss from C-rich AGB stars at low metallicity? *A&A*, 484:L5–L8, June 2008.

R. D. McClure and A. W. Woodsworth. The binary nature of the barium and CH stars. III - Orbital parameters. *ApJ*, 352:709–723, April 1990.

I. McDonald and J. T. van Loon. Dust, pulsation, chromospheres and their rôle in driving mass loss from red giants in Galactic globular clusters. *A&A*, 476:1261–1282, December 2007.

A. McWilliam and T. A. Smecker-Hane. The Composition of the Sagittarius Dwarf Spheroidal Galaxy, and Implications for Nucleosynthesis and Chemical Evolution. In T. G. Barnes III & F. N. Bash, editor, *Cosmic Abundances as Records of Stellar*

Evolution and Nucleosynthesis, volume 336 of *Astronomical Society of the Pacific Conference Series*, pages 221–+, September 2005.

M. Meixner, K. D. Gordon, R. Indebetouw, J. L. Hora, B. Whitney, R. Blum, W. Reach, J.-P. Bernard, M. Meade, B. Babler, C. W. Engelbracht, B.-Q. For, K. Misselt, U. Vijh, C. Leitherer, M. Cohen, E. B. Churchwell, F. Boulanger, J. A. Frogel, Y. Fukui, J. Gallagher, V. Gorjian, J. Harris, D. Kelly, A. Kawamura, S. Kim, W. B. Latter, S. Madden, C. Markwick-Kemper, A. Mizuno, N. Mizuno, J. Mould, A. Nota, M. S. Oey, K. Olsen, T. Onishi, R. Paladini, N. Panagia, P. Perez-Gonzalez, H. Shibai, S. Sato, L. Smith, L. Staveley-Smith, A. G. G. M. Tielens, T. Ueta, S. van Dyk, K. Volk, M. Werner, and D. Zaritsky. Spitzer Survey of the Large Magellanic Cloud: Surveying the Agents of a Galaxy's Evolution (SAGE). I. Overview and Initial Results. *AJ*, 132:2268–2288, December 2006.

R. A. Mesler and G. D. Henson. Luminosity Variations in Post-AGB Stars. *Journal of the Southeastern Association for Research in Astronomy*, 2:10–13, May 2008.

T. J. Millar. Molecule and dust grain formation. In H. J. Habing and H. Olofsson, editors, *Asymptotic Giant Branch Stars*, page 247, 2004.

S. Moehler, D. Koester, M. Zoccali, F. R. Ferraro, U. Heber, R. Napiwotzki, and A. Renzini. Spectral types and masses of white dwarfs in globular clusters. *A&A*, 420:515–525, June 2004.

L. Monaco, M. Bellazzini, P. Bonifacio, F. R. Ferraro, G. Marconi, E. Pancino, L. Sbordone, and S. Zaggia. The Ital-FLAMES survey of the Sagittarius dwarf spheroidal galaxy. I. Chemical abundances of bright RGB stars. *A&A*, 441:141–151, October 2005.

L. Monaco, M. Bellazzini, F. R. Ferraro, and E. Pancino. The distance to the Sagittarius dwarf spheroidal galaxy from the red giant branch tip. *MNRAS*, 353:874–878, September 2004.

M. Mouhcine and A. Lançon. The modelling of intermediate-age stellar populations. I. Near-infrared properties. *A&A*, 393:149–166, October 2002.

M. Mouhcine and A. Lançon. Carbon star populations in systems with different metallicities: statistics in Local Group galaxies. *MNRAS*, 338:572–586, January 2003.

N. Mowlavi. Carbon Production from Low- and Intermediate-Mass Stars. In D. Friedli, M. Edmunds, C. Robert, & L. Drissen, editor, *Abundance Profiles: Diagnostic Tools for Galaxy History*, volume 147 of *Astronomical Society of the Pacific Conference*

Series, pages 166–+, 1998.

C. P. Nicholls, P. R. Wood, M.-R. L. Cioni, and I. Soszyński. Long Secondary Periods in variable red giants. *MNRAS*, 399:2063–2078, November 2009.

P. North, A. Jorissen, and M. Mayor. Binarity among Barium Dwarfs and CH Subgiants: Will They Become Barium Giants? In R. F. Wing, editor, *The Carbon Star Phenomenon*, volume 177 of *IAU Symposium*, pages 269–+, June 2000.

L. Pasquini, G. Avila, A. Blecha, C. Cacciari, V. Cayatte, M. Colless, F. Damiani, R. de Propris, H. Dekker, P. di Marcantonio, T. Farrell, P. Gillingham, I. Guinouard, F. Hammer, A. Kaufer, V. Hill, M. Marteaud, A. Modigliani, G. Mulas, P. North, D. Popovic, E. Rossetti, F. Royer, P. Santin, R. Schmutzer, G. Simond, P. Vola, L. Waller, and M. Zoccali. Installation and commissioning of FLAMES, the VLT Multifibre Facility. *The Messenger*, 110:1–9, December 2002.

C. Payne-Gaposchkin. The red variable stars. *Annals of Harvard College Observatory*, 113:189–208, 1954.

C. A. Pilachowski. Abundances in Cool Evolved Stars. In K. Nomoto, editor, *IAU Colloq. 108: Atmospheric Diagnostics of Stellar Evolution*, volume 305 of *Lecture Notes in Physics, Berlin Springer Verlag*, pages 17–+, 1988.

O. R. Pols and R. G. Izzard. Carbon-enhanced metal-poor stars – effects of binary evolution at low metallicity. In H. J. G. L. M. Lamers, N. Langer, T. Nugis, & K. Annuk, editor, *Stellar Evolution at Low Metallicity: Mass Loss, Explosions, Cosmology*, volume 353 of *Astronomical Society of the Pacific Conference Series*, pages 233–+, December 2006.

S. Ramstedt, F. L. Schöier, and H. Olofsson. The Mass-Loss Rates and Molecular Abundances of S-type AGB Stars. In F. Kerschbaum, T. Lebzelter, & R. F. Wing, editor, *Why Galaxies Care about AGB Stars II: Shining Examples and Common Inhabitants*, volume 445 of *Astronomical Society of the Pacific Conference Series*, page 263, September 2011.

E. Rebeirot, M. Azzopardi, and B. E. Westerlund. Carbon stars in the Small Magellanic Cloud. II - Catalogue of 1707 objects with identifications and spectrophotometry. *A&AS*, 97:603–728, February 1993.

D. Reimers. Circumstellar absorption lines and mass loss from red giants. *Memoires of the Societe Royale des Sciences de Liege*, 8:369–382, 1975.

G. H. Rieke and M. J. Lebofsky. The interstellar extinction law from 1 to 13 microns.

ApJ, 288:618–621, January 1985.

W. R. J. Rolleston, P. L. Dufton, N. D. McErlean, and K. A. Venn. The chemical composition of the young, Inter-Cloud population. *A&A*, 348:728–736, August 1999.

W. R. J. Rolleston, K. Venn, E. Tolstoy, and P. L. Dufton. The present-day chemical composition of the SMC from UVES spectra of the sharp-lined, B-type dwarf AV 304. *A&A*, 400:21–30, March 2003.

N. G. Roman. A group of high velocity F-type stars. *AJ*, 59:307–312, 1954.

S. C. Russell and M. A. Dopita. Abundances of the heavy elements in the Magellanic Clouds. III - Interpretation of results. *ApJ*, 384:508–522, January 1992.

L. Sbordone, P. Bonifacio, R. Buonanno, G. Marconi, L. Monaco, and S. Zaggia. The exotic chemical composition of the Sagittarius dwarf spheroidal galaxy. *A&A*, 465: 815–824, April 2007.

J. M. Scalo and G. E. Miller. A method for the determination of metal abundances in the Galactic nuclear bulge and nearby galaxies. *ApJL*, 248:L65–L68, September 1981.

D. Schönberner and M. Steffen. The Formation and Evolution of Planetary Nebulae (invited review). In S. Kwok, M. Dopita, & R. Sutherland, editor, *Planetary Nebulae: Their Evolution and Role in the Universe*, volume 209 of *IAU Symposium*, pages 147–+, 2003.

M. H. Siegel, Y. Karataş, and I. N. Reid. Metallicities and ages of stellar populations at a high Galactic latitude field. *MNRAS*, 395:1569–1578, May 2009.

G. C. Sloan, K. E. Kraemer, P. R. Wood, A. A. Zijlstra, J. Bernard-Salas, D. Devost, and J. R. Houck. The Magellanic Zoo: Mid-Infrared Spitzer Spectroscopy of Evolved Stars and Circumstellar Dust in the Magellanic Clouds. *ApJ*, 686:1056–1081, October 2008.

T. A. Smecker-Hane and A. McWilliam. The Complex Chemical Abundances and Evolution of the Sagittarius Dwarf Spheroidal Galaxy. *ArXiv Astrophysics e-prints*, May 2002.

C. Sneden, G. W. Preston, and J. J. Cowan. Binary Blue Metal-poor Stars: Evidence for Asymptotic Giant Branch Mass Transfer. *ApJ*, 592:504–515, July 2003.

I. Soszynski, A. Udalski, M. Kubiak, M. K. Szymanski, G. Pietrzynski, K. Zebrun, O. Szewczyk, L. Wyrzykowski, and W. A. Dziembowski. The Optical Gravitational Lensing Experiment. Ellipsoidal Variability of Red Giants in the Large Magellanic

Cloud. *Acta Astron.*, 54:347–362, December 2004.

O. Suárez, P. García-Lario, and M. Manteiga. Stellar evolution in the Post-AGB stage. *Lecture Notes and Essays in Astrophysics*, 2:149–158, December 2006.

P. G. van Dokkum. Cosmic-Ray Rejection by Laplacian Edge Detection. *PASP*, 113: 1420–1427, November 2001.

J. T. van Loon. On Determining the Mass-Loss Rates of Red Giants and Red Supergiants Based on Infrared Data. In F. Kerschbaum, C. Charbonnel, & R. F. Wing, editor, *Why Galaxies Care About AGB Stars: Their Importance as Actors and Probes*, volume 378 of *Astronomical Society of the Pacific Conference Series*, pages 227–+, November 2007.

H. van Winckel. Post-Agb Stars. *ARA&A*, 41:391–427, 2003.

H. van Winckel. Why Galaxies Care about Post-AGB stars. In F. Kerschbaum, T. Lebzelter, & R. F. Wing, editor, *Why Galaxies Care about AGB Stars II: Shining Examples and Common Inhabitants*, volume 445 of *Astronomical Society of the Pacific Conference Series*, page 133, September 2011.

K. A. Venn. A-Type Supergiant Abundances in the Small Magellanic Cloud: Probes of Evolution. *ApJ*, 518:405–421, June 1999.

P. Ventura and F. D'Antona. Hot bottom burning in the envelope of super asymptotic giant branch stars. *MNRAS*, 410:2760–2766, February 2011.

P. Ventura and P. Marigo. Asymptotic giant branch stars at low metallicity: the challenging interplay between the mass-loss and molecular opacities. *MNRAS*, 408: 2476–2486, November 2010.

C. Waelkens and R. B.F.M. Waters. Post-agb stars. In H. J. Habing and H. Olofsson, editors, *Asymptotic Giant Branch Stars*, page 519, 2004.

T. P. Wallace and C. A. Clayton. RV - Radial Components of Observer's Velocity, Starlink User Note 78.8. 1996.

B. E. Westerlund. *The Magellanic Clouds*. January 1997.

P. Whitelock. Luminosities of AGB variables. In Y. Nakada, M. Honma, & M. Seki, editor, *Mass-Losing Pulsating Stars and their Circumstellar Matter*, volume 283 of *Astrophysics and Space Science Library*, pages 19–26, April 2003.

P. Whitelock, J. Menzies, M. Irwin, and M. Feast. Carbon Stars in the Sagittarius Dwarf Galaxy. In P. Whitelock & R. Cannon, editor, *The Stellar Content of Local Group Galaxies*, volume 192 of *IAU Symposium*, pages 136–+, January 1999.

P. A. Whitelock, M. W. Feast, F. Marang, and M. A. T. Groenewegen. Near-infrared photometry of carbon stars. *MNRAS*, 369:751–782, June 2006.

P. A. Whitelock, M. W. Feast, and F. van Leeuwen. AGB variables and the Mira period-luminosity relation. *MNRAS*, 386:313–323, May 2008.

L. A. Willson. Mass Loss From Cool Stars: Impact on the Evolution of Stars and Stellar Populations. *ARA&A*, 38:573–611, 2000.

P. R. Wood, C. Alcock, R. A. Allsman, D. Alves, T. S. Axelrod, A. C. Becker, D. P. Bennett, K. H. Cook, A. J. Drake, K. C. Freeman, K. Griest, L. J. King, M. J. Lehner, S. L. Marshall, D. Minniti, B. A. Peterson, M. R. Pratt, P. J. Quinn, C. W. Stubbs, W. Sutherland, A. Tomaney, T. Vandehei, and D. L. Welch. MACHO observations of LMC red giants: Mira and semi-regular pulsators, and contact and semi-detached binaries. In T. Le Bertre, A. Lebre, & C. Waelkens, editor, *Asymptotic Giant Branch Stars*, volume 191 of *IAU Symposium*, pages 151–+, 1999.

P. R. Wood, H. J. Habing, and P. J. McGregor. Infrared monitoring of OH/IR stars near the Galactic Center. *A&A*, 336:925–941, August 1998.

P. R. Wood, J. B. Whiteoak, S. M. G. Hughes, M. S. Bessell, F. F. Gardner, and A. R. Hyland. OH/IR stars in the Magellanic Clouds. *ApJ*, 397:552–569, October 1992.

S. A. Zhevakin. Physical Basis of the Pulsation Theory of Variable Stars. *ARA&A*, 1: 367–+, 1963.

A. A. Zijlstra. Mass loss and AGB evolution in extra-galactic stellar populations. In T. Le Bertre, A. Lebre, & C. Waelkens, editor, *Asymptotic Giant Branch Stars*, volume 191 of *IAU Symposium*, pages 551–+, 1999.

A. A. Zijlstra. Low-mass supernovae in the early Galactic halo: source of the double r/s-process enriched halo stars? *MNRAS*, 348:L23–L27, February 2004.

A. A. Zijlstra. Mass loss on the Asymptotic Giant Branch. In M. J. Barlow & R. H. Méndez, editor, *Planetary Nebulae in our Galaxy and Beyond*, volume 234 of *IAU Symposium*, pages 55–62, 2006.

A. A. Zijlstra, K. Gesicki, J. R. Walsh, D. Péquignot, P. A. M. van Hoof, and D. Minniti. The planetary nebula population of the Sagittarius dwarf spheroidal galaxy. *MNRAS*, 369:875–890, June 2006a.

A. A. Zijlstra, M. Matsuura, P. R. Wood, G. C. Sloan, E. Lagadec, J. T. van Loon, M. A. T. Groenewegen, M. W. Feast, J. W. Menzies, P. A. Whitelock, J. A. D. L. Blommaert, M.-R. L. Cioni, H. J. Habing, S. Hony, C. Loup, and L. B. F. M. Waters. A Spitzer mid-infrared spectral survey of mass-losing carbon stars in the Large Magellanic Cloud. *MNRAS*, 370:1961–1978, August 2006b.

A. A. Zijlstra and J. R. Walsh. Two planetary nebulae in the Sagittarius Dwarf Galaxy. *A&A*, 312:L21–L24, August 1996.